Section III

PHYSICS OF THE SOLAR ACTIVITY AND DYNAMIC PROCESSES IN THE INTER-PLANETARY SPACE AND IN THE EARTH'S MAGNETOSPHERE

Edited by S. N. Vernov, V. A. Dergachev, S. I. Isaev, and G. E. Kocharov

STRUCTURE OF THE INTERPLANETARY SPACE FROM OBSERVATIONS OF LOW-ENERGY COSMIC RAYS IN 1965—1967

S.N. Vernov, G.P. Lyubimov, and N.V. Pereslegina

The probing of the interplanetary space with cosmic rays, which propagate over tremendous distances while interacting with the interplanetary medium, constitutes an important branch of space physics. Cosmic rays carry information about large-scale magnetic fields and solar plasma. The most effective approach calls for a simultaneous study of various characteristics of the solar cosmic rays (SCR) and the galactic cosmic rays (GCR) with an attempt to establish a correlation between cosmic-ray effects and solar activity.

Let us first consider the results of analysis of 15 SCR showers ($1 < E_p < 5$ MeV) associated with chromospheric flares on the visible side of the Sun. Most of these events were accompanied by Forbush decreases of the GCL in space ($E_p > 30$ MeV) and on Earth ($E_p > 1$ BeV). The cosmic ray intensity was studied in the following periods: 4—7 Oct. 1965, 29 Dec. 1965—3 Jan. 1966, 19—22 Jan. 1966, 24—28 June 1967, 1—5 Aug. 1967, 9—12 Aug. 1967, 17—22 Sept. 1967 /1, 2/.

Solar flares at longitudes of 30 to 90°W cause direct SCR showers. The length of the Archimedes spiral from the Sun to the Earth for plasma velocities of 300 km/sec is about $200 \cdot 10^6$ km. Protons with $1 < E_p < 5$ MeV and a pitch angle of 0° will traverse this spiral in from 2 to 4 hr. The initial distribution over pitch angles may increase the length of this time, but apparently by no more than a factor of 2. For flares in a weakly disturbed medium, the time of arrival of the SCR is indeed 2—4 hr. Inhomogeneities may increase this period up to about 10 hr for other flares. Thus, within the margin of measurement error (±2 hr) the time of direct arrival of the SCR from flares at longitudes of from 30 to 90°W approximately corresponds to the time of motion of the particles with velocities determined by their kinetic energy. Hence it follows that if the transverse diffusion coefficient is small for particles of these energies, the SCR in some unknown way (possibly because of the high energy density at the time of the flare) occupy a whole bundle of magnetic field lines emerging from the flare area. Thus, the angular distribution of the SCR particles is fixed during the solar flare. It determines the variation of the intensity across the bundle of magnetic field lines. The intensity increases from the leading (lateral) front toward the central channel and then decreases. The distribution should depend on the field geometry and may slowly vary with time owing to velocity variance, diffusion, and drift during the motion from the Sun. The particles generated by the

flare may be retained in substantial numbers for at least 3 days behind the shock-wave front /3/, thus creating a source which replenishes the particle flux downstream from the shock. As a result, we can ignore the variation of the particle flux with time and assume that the drop in intensity is associated with the SCR distribution across the beam as generated at the time of the flare. In this case, the delay time of the direct SCR maximum corresponds to the time required for the principal flux channel to turn with the Sun from its original position at the time of the flare to a position of coincidence with the detector. In all cases, the Archimedian spirals derived from delay measurements have a somewhat greater pitch than the spirals determined from the corresponding active regions and the solar wind velocity. This difference we call the "veering" of particles from the line of force. "Veering" can be caused by drift, directional collective pressure, and shock waves. "Veering" causes differences in the propagation of SCR westward and eastward from the optimal trajectory, i.e., from the spiral "aimed" from the active region to the detector. Figure 1 is an instantaneous directivity chart of the SCR flux based on maximum anisotropy data for six SCR flares. The chart clearly illustrates the westward "veering" from the field line.

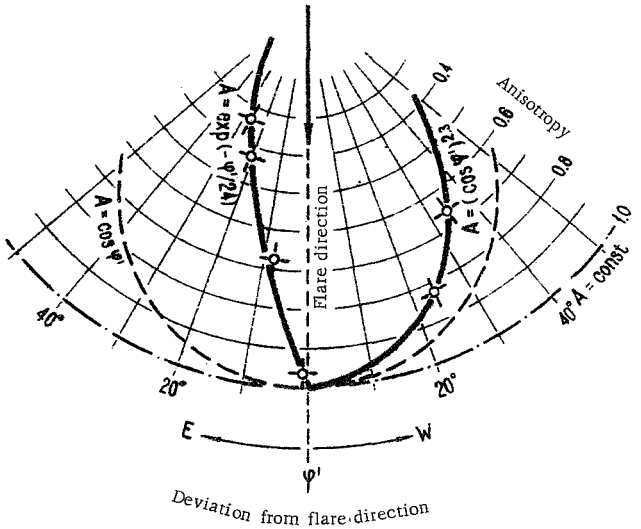

FIGURE 1. Distribution of the maximum SCR anisotropy (thick line) relative to the optimal longitude of the solar flare (about 60°W for 1 a.u.).

Let us consider the characteristics of SCR bursts observed simultaneously with Forbush decreases of the GCR. These events are observed either independently or at the time of the second maximum after the direct arrival of the SCR. For these SCR showers, the delay time of the maximum relative to the time of the solar flare reaches as much as 20 to 80 hr, which corresponds to a mean radial velocity of from 500 to 1500 km/sec, i.e., the velocity of propagation of shock waves from solar flares. The maximum

anisotropy varies from 16 to 37%. These SCR showers are particles generated during the solar flare which are localized between the shock-wave front and the plasma front produced by the same flare. Figure 2a schematically shows the Forbush decrease and the three space regions corresponding to 1) undisturbed medium downstream from the shock-wave front, 2) the enhanced compressed magnetic field between the shock-wave front and the plasma (the GCL decrease phase), 3) the region between the two fronts and the Sun (the GCL recovery phase). Figure 2b shows the same regions for the magnetic fields in the plane of the ecliptic, as viewed from the North Pole. The sections of the spiral lines correspond to the magnetic lines of force, and the dashed arcs are the shock-wave front and the plasma front. The figure is based on Parker's model of a shock wave propagating from a solar flare /4/.

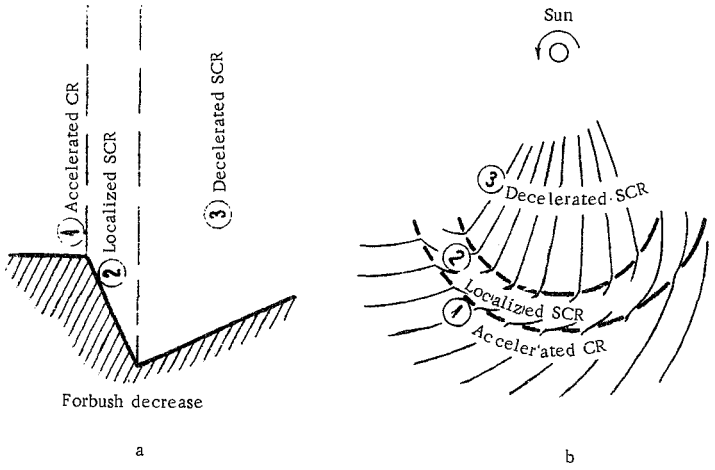

FIGURE 2. Localization of SCR.

The first region contains GCR and SCR particles — leftovers of previous showers or of quiet quasistationary streams — accelerated by the leading shock-wave front. These accelerated particles may produce a maximum before the onset of the Forbush decrease /5/.

The second region contains localized SCR generated by the flare and held up by the shock wave and the hot plasma front. These SCR propagate together with the second layer with the same velocity as the shock wave and the plasma. The SCR moving along the break in magnetic field lines may partially leak out from the localization layer feeding the first region. The anisotropy of the SCR in this layer may thus be fairly high along the field and small in the transversal direction.

The third layer contains particles which left the localized layer, were injected by a later flare, or originated in the active region during a lull between flares. The first two sources should be characterized by a bidirectional anisotropy owing to the motion of the particles between the layer and the Sun. SCR leaving the active region during a lull between

successive flares have a positive anisotropy because of the steady and continued activity of the source.

The above analysis of SCR propagation shows that protons with $1 < E_p < 5$ MeV generated by a solar flare propagate in the interplanetary space mainly by direct motion along the magnetic field lines with velocities corresponding to their kinetic energy and by being transported with the shock wave and the plasma envelope ejected by the flare. The particles are delivered to any point in space by either one of these mechanisms or by a combination of both. Whether or not they reach a certain point is mainly determined by the longitude of the solar flare relative to the detector. For "eastern" and "central" flares the transport mechanism is the dominant factor: direct motion along the lines of force is ruled out because the magnetic field is coiled eastward. For "western" flares the direct motion mechanism predominates, and it may be supplemented by transport as long as the flare is not too close to the limb. The experimental results on hand are insufficient to assess the contribution of the diffusion component to propagation of cosmic rays. The rate of transverse diffusion is apparently less than the transport velocity, and the rate of longitudinal diffusion is also substantially smaller than the direct velocity. The lines of forces in some cases are exceedingly smooth, and "mirror" condensations are observed only at large distances from the Sun ($\geqslant 1.5$ a.u. /3/). In other cases, a whole string of "distributed semitransparent mirrors" may be scattered along the field lines, so that our instruments simultaneously (to within ± 2 hr) detect streams of particles moving in opposite directions at the observation point.

Let us describe a model of propagation of low-energy SCR, injected by a solar flare, to a distance of 1 a.u. from the Sun. Figure 3a shows the position of the beam from three magnetic tubes relative to the detector (point 1) at the time t_0 corresponding to the beginning of a solar flare at a longitude $30° < \varphi < 60°$. At the time t_1, the most energetic particles having zero pitch angle reach the detector, moving along a tube of length l with a velocity corresponding to their kinetic energy. A time Δt after t_1 is required for all the particles injected into this tube with a flux $I < I_{max}$ (including particles of lower energies and particles with nonzero pitch angle) to reach the detector. Further growth of intensity is associated with the rotation of the bundle of tubes together with the Sun and the approach of the central channel with maximum particle density toward the detector. The tube density is fixed at a time close to the flare time t_0 and it is maintained constant by the SCR localized behind the shock wave. At the time t_2, the detector sees a tube carrying the flux I_{max}. The subsequent decrease in intensity is associated with the recession of the central channel from the detector.

Figure 3b corresponds to a situation when the central channel is aimed at the detector (point 2) at the time of the solar flare t_0 ($\varphi = 60°$W). In this case, the intensity reaches its maximum value I_{max} in a time Δt, i.e., the phase of intensity growth due to source rotation is not observed in this case, but all the other features remain as before.

In Figure 3c the flare developed at a time t_0 ($60° < \varphi < 90°$W), when a tube lying eastward of the central channel and carrying a SCR flux $I < I_{max}$ was aimed at the detector (point 3). The time t_1, the delay Δt, and the

dependence of the detected intensity on magnetic tube rotation in this case are exactly the same as before. At a time $t_1 + \Delta t$ the detector will see the intensity I which will steadily decrease thereafter.

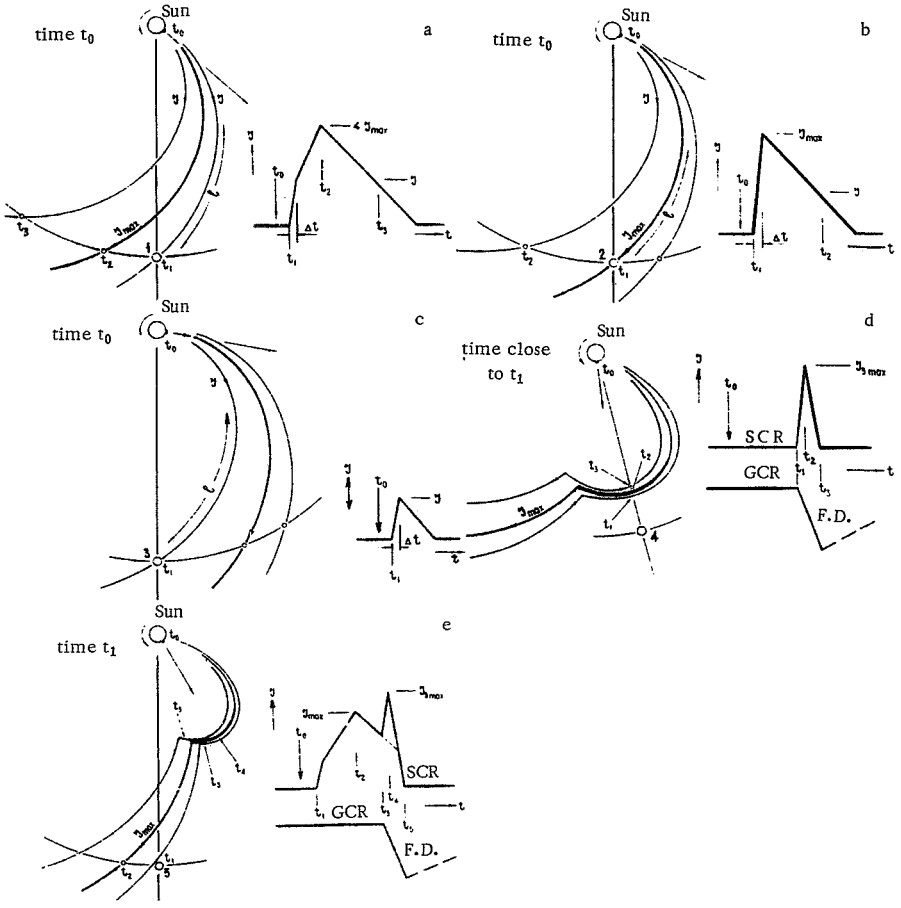

FIGURE 3. Schematic diagrams illustrating the distribution of SCR from a flare.

In Figure 3d, the flare which burst at the time t_0 lies in the eastern part of the Sun disk. The time required for the SCR-filled tubes to turn toward the detector (point 4) is greater in this case than the time for the shock wave to cover the distance from the Sun to the detector. The SCR intensity will therefore start increasing only at the time t_1 corresponding to the arrival of the shock wave and the beginning of the GCR Forbush decrease. This time is determined by the velocity of the shock wave in a given direction and the distance to the detector. The time t_2 will correspond to the maximum flux of localized SCR I_3 max, i.e., the flux in the tube with maximum population, broken and compressed between the

leading and the trailing shock-wave fronts. This time approximately coincides with the middle phase of the GCR Forbush decrease. The time t_3 corresponds to the passage of the trailing front and signifies the beginning of the GCR recovery phase.

The intermediate case shown in Figure 3e corresponds to a solar flare which at the time t_0 lay approximately between the central meridian and 30°W. The development is determined by the relationship between the time needed for the central channel to turn toward the detector (point 5, time t_2) and the time t_3 for the shock wave to reach subsequently the same point. It should be emphasized that all these cases only constitute different facets of the same process of SCR propagation from the flare, as observed at a certain point in space.

Let us consider some results pertaining to the GCR Forbush decrease associated with solar flares. For type II flares accompanied by a Forbush decrease, the mean radial velocities of the shock waves were determined from the known Sun – detector distance and the known time when the decrease began. In seven cases, when the spacecraft and the Earth were at a sufficient distance from each other on the same radius from the Sun, two values of the mean radial velocity were determined: $\overline{V}_1$ to the detector closer to the Sun and $\overline{V}_2$ to the more distant detector. The mean velocity $\overline{V}_3$ in the space between the two detectors was also found /6/. The values obtained for $\overline{V}_1$, $\overline{V}_2$, and $\overline{V}_3$ show that the velocity decreases with distance and time, i.e., the shock waves are decelerated (Figure 4). Assuming that the mean velocity linearly decreases with time, we found for each flare the initial velocities $\overline{V}_0$, the decelerations a, and the distances S_0 at which the shock waves decay completely. The decelerations were found to range from about 140 to 4000 cm · sec^{-2}. The shock waves stop approximately at the same distance from the Sun (between the Earth and the Mars orbits) and the decelerations are $a \sim V_0^2$.

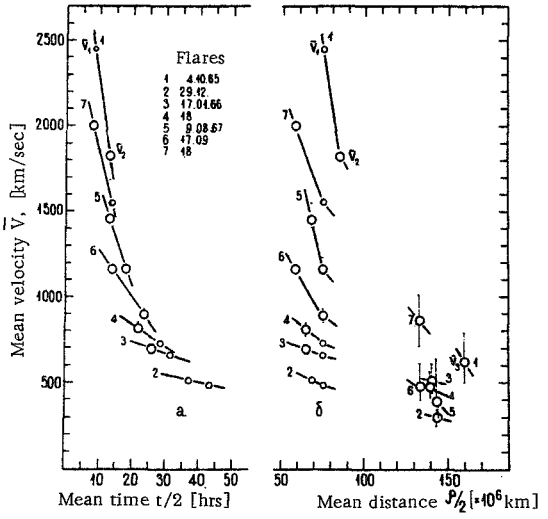

FIGURE 4. The mean shock-wave velocity vs. time (a) and distance (b).

The deceleration of shock waves should lead to a gradual reduction of the Forbush decrease, because of the decrease in the propagation velocity. At a certain distance from the Sun, no Forbush decrease will thus be observed. The solar cosmic rays localized behind the shock-wave front gradually leak out and accumulate near the boundary of the modulation region as the shock waves decay. These effects are corroborated by experimental findings. Over the simultaneous trajectory of VENUS-2 and ZOND-3 in December 1965 and January 1966, the Forbush decreases caused by the flares of 29—30 December 1965 and 17—18 January 1966 and observed by VENUS-2 had all but disappeared at distances of from 1.29 to 1.31 a.u. according to ZOND-3 measurements, although the SCR enhancements were observed on ZOND-3 (Figure 5).

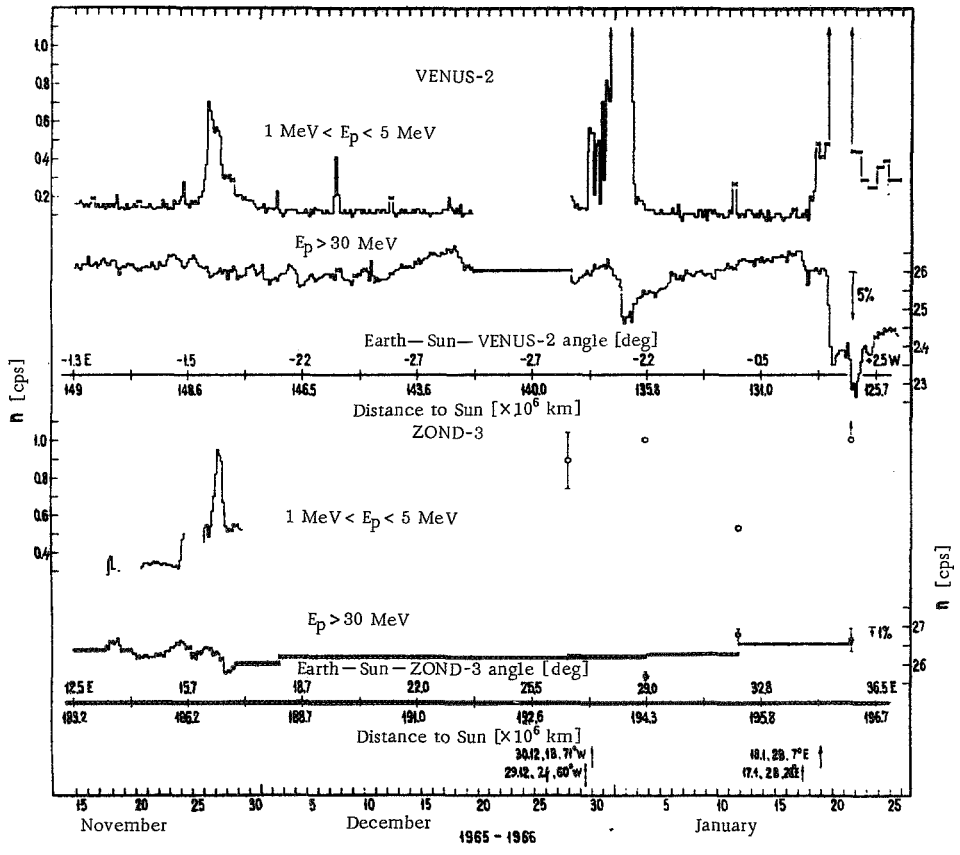

FIGURE 5. SCR and GCR intensity over simultaneous flight trajectories of VENUS-2 and ZOND-3. The arrows indicate solar flares.

The analysis of the depth and the steepness of the Forbush decrease shows a tendency toward a shallower decrease as one moves away from the Sun and away from the flare direction. The steepness of the Forbush

decrease diminishes more rapidly than its depth; this is associated with the longer duration of the decrease phase, i.e., with the noticeable spreading of the region between the leading and the trail shock-wave fronts during the motion of the shock wave from the Sun.

Observations of the Forbush decreases in a weakly disturbed medium reveal a break in the phase of the intensity drop corresponding to an increase in steepness. At high energies (>1 BeV), the increase in steepness is insignificant (approximately by a factor of two), and at low energies (> 30 MeV) it is quite substantial (by a factor of about 6 — 8). This fall in the GCR intensity may be qualitatively interpreted by assuming a semitransparent mirror moving from the Sun toward the detector. This mirror will screen off the GCR flux reaching the detector. When the mirror has reached the detector, the fall of intensity occurs inside the mirror. For low-energy cosmic rays the transparency factor is clearly smaller than for high-energy cosmic rays. The intensity of the low-energy cosmic rays will therefore fall more gently and gradually before the mirror and more steeply behind the mirror than the intensity of the high-energy cosmic rays.

Let us consider the results of the analysis of GCR variations, i.e., the shallow intensity decreases of the GCR caused by the magnetic fields of quasistationary corpuscular streams from active regions which turn together with the Sun.

At a distance of 1 a.u. from the Sun, the structure of the interplanetary magnetic field proposed by Parker /4/ for the solar wind and by Mustel /7, 8/ for corpuscular streams appears to be made up of discrete magnetic tubes with various field strengths, oriented on the average along the Archimedes spiral in the plane of the ecliptic. The rotation of the interplanetary magnetic field relative to the detector together with the Sun causes a modulation of the GCR flux which is recorded by the detector as a time-modulation of intensity.

During the flight of ZOND-3 and VENUS-2, i.e., during approximately 6 months, about 30 GCR intensity decreases were recorded ($E_p > 30$ MeV) with depths ranging from about 0.5 to 5% and duration (length of decrease phase) of from about 15 to 65 hr /9/. Each decrease was correlated with a definite active region, viz., with a bright calcium flocculus. Comparison of the successive transits of the active region across the central meridian of the Sun (regardless of the latitude of the active region) with the time of the beginning of the GCR intensity decrease (making allowance for the mean time shift of 5 days for the propagation of the corpuscular stream) reveals a strong correlation between these effects (correlation coefficient $K = 0.955 \pm 0.004$). This comparison confirms that the active regions were properly identified, that the plasma moves quasiradially in the equatorial plane from the active region, and that the magnetic fields of active regions from all latitudes apparently "focus" in the equatorial plane.

The mean radial velocities of the corpuscular streams V_p were determined from the known heliocentric orbits of the spacecraft at the time of observations of the GCR intensity decrease and from the delay of the observed decrease time relative to the transit of the active region across the central meridian. For active regions existing for the duration of more than a single axial rotation of the Sun, the velocity V_p was found to depend

on the phase of development of the active region. High velocities V_p correspond to maximum development of the active region. Observations of some cases of rapid development of active regions outside the central meridian show that these cases are also associated with GCR decreases with a steeper intensity drop. The active regions in these cases apparently eject a high-velocity corpuscular stream which does not move in the radial direction, i.e., the initial phase of this event corresponds to a flare.

Comparison of the "strength" of the active regions, i.e., the product of its area and brightness, with the depth of the GCR decrease reveals a definite correlation between these parameters ($K = 0.83 \pm 0.01$). Some points deviate from this dependence, which is apparently due to latitude effects, presence of M-regions, and rapidly developing active regions. One case of a very bright active region was observed, which did not cause a GCR decrease. This active region apparently did not inject corpuscular streams because of its peculiar configuration and the strength of its magnetic field.

In conclusion, let us consider the propagation of SCR not associated with solar flares in the quasistationary magnetic fields of corpuscular streams. The GCR intensity variations ($E_p > 30$ MeV) measured during the simultaneous flight of VENUS-2 and ZOND-3 (from 17 to 29 November 1965, Figure 5), the two spacecraft traveling at a distance of about $40 \cdot 10^6$ km from each other on the same radius-vector from the Sun, made it possible to establish the structure of the magnetic fields between the orbits of these spacecraft.

The field geometry is initially assumed to be in the form of Archimedes spirals. Relevant features, e.g., maxima, minima, steps, etc., were visually identified on the curves of the GCR intensity variation recorded on VENUS-2 and ZOND-3. The recording time t of each feature was determined and the time delays Vt between the corresponding features on VENUS-2 and ZOND-3 were found. For each t, a certain hypothetical velocity V_c was calculated, which characterized the pitch of the Archimedes spiral. Note that V_c characterizes the position of the magnetic field front of the cropuscular stream, and may thus have values ranging from 0 to $\pm\infty$ in various sections of magnetic tubes bent in the shape of a zigzag or a loop. V_c is equal to the plasma velocity only in undisturbed sections in cases of regular ejection of plasma from the active region /9/.

SCR streams of other than flare origin were also observed over the simultaneous flight trajectory of VENUS-2 and ZOND-3. Figure 5 shows that the position of the individual SCR maxima on ZOND-3 relative to the GCR variations is different from that on VENUS-2: the shift Vt between the SCR maxima is smaller than the shift between the GCR details at the same points. The velocity V_c can be calculated from the shift Vt between the SCR streams. The V_c for the SCR streams is invariably greater than the corresponding velocities of the corpuscular streams, i.e., the SCR propagate along a spiral with a greater pitch. Thus, SCR of other than flare origin show a definite westward "veering" from the helical magnetic fields, like the SCR generated by flares. The same effect was observed on the simultaneous flight trajectory of IMP III, ZOND-3, and MARINER IV /2/.

The probing of the interplanetary space by low-energy cosmic rays thus discloses the quasihelical structure of the interplanetary magnetic fields originating in the active solar regions and turning together with the Sun. These magnetic fields are disturbed by the traveling shock waves originating during solar flares. The shock waves rapidly decay, breaking up between the Earth and the Mars orbits. Solar cosmic rays propagating in helical magnetic fields "veer" westward. Low-energy solar cosmic rays are effectively transported from solar flares behind shock-wave fronts.

Bibliography

1. Vernov, S.N., A.E. Chudakov, P.V. Vakulov, Yu.I. Logachev, G.P. Lyubimov, A.G. Nikolaev, and N.V.Pereslegina.— Izvestiya AN SSSR, 31(8):1296. 1967.
2. Vernov, S.N., A.E. Chudakov, P.V. Vakulov, E.V. Gorchakov, N.N. Kontor, S.N. Kuznetsov, Yu.I. Logachev, G.P. Lyubimov, A.G. Nikolaev, N.V. Pereslegina, and B.A. Tverskoi.— Trudy V Vsesoyuznoi ezhegodnoi zimnei shkoly po kosmofizike, Apatity, p.5, Izd. Kol'skogo filiala AN SSSR. 1968.
3. Vernov, S.N., N.N. Kontor, S.N. Kuznetsov, Yu.I.Logachev, G.P. Lyubimov, and N.V. Pereslegina.— Doklad na Vsesoyuznoi konferentsii po fizike kosmicheskikh luchei, Tashkent. 1968.
4. Parker, E.N. Interplanetary Dynamic Processes.—New York, Wiley. 1963.
5. Rao, U.R., K.G. McCracken, and R.P. Bukata.— J. Geophys. Res., **72**:4325. 1967.
6. Lyubimov, G.P.— Astronomicheskii tsirkulyar, AN SSSR, No.488:4. 1968.
7. Mustel', E.R.— Astronomicheskii zhurnal, **37**:403. 1960.
8. Mustel', E.R.— Astronomicheskii zhurnal, **39**:619. 1962.
9. Vernov, S.N., Yu.I. Logachev, G.P. Lyubimov, and N.V. Pereslegina.— Doklad na Vsesoyuznoi Konferentsii po fizike kosmicheskikh luchei. Tashkent. 1968.

PROPAGATION OF 1.5 MeV SOLAR PROTONS IN THE INTERPLANETARY SPACE

S.N. Vernov, E.V. Gorchakov, and G.A. Timofeev

Observations from interplanetary automatic stations and ground installations provided extensive experimental data concerning bursts of protons of solar origin /1 – 3/. In this connection, the problem of the proton transport from the source in the solar flare is of considerable significance.

Charged particles generated on the Sun propagate in the interplanetary magnetic field, which is made up of two components: the regular magnetic field of the Sun and the randomized magnetic field of the inhomogeneities. At the relevant distances $R \sim 1$ a.u., the protons should move almost parallel to the field lines because of the conservation of the magnetic moment in the Sun's regular field. However, the magnetic field inhomogeneities scatter the charged particles, thus essentially affecting their trajectory and distribution in time and in space. We will consider the propagation of 1.5 MeV protons in the interplanetary field. The regular field of the Sun is taken to vary as $1/R^2$. The interaction of a proton with the magnetic field inhomogeneities is given if we know the mean free path between the inhomogeneities and the mean angle of scattering by inhomogeneities, σ. An important parameter characterizing the transport process is the transport length Λ. In our case, the transport length, which is understood as the free path corresponding to the mean scattering angle $\pi/2$, is given by the equation

$$\Lambda = l \left(\frac{\pi}{2\sigma}\right)^2.$$

We assumed that the free path l, the mean scattering angle σ, and hence the transport length Λ are all independent of the heliocentric distance. The motion of a proton between inhomogeneities is governed by considerations of magnetic moment conservation.

The problem was solved by the Monte Carlo technique. The proton is injected into the interstellar field at a distance of 10^{-2} a.u. from the Sun at 30° to the field line. The first stage deals with the selection of the motion of the proton prior to collision with the first inhomogeneity. The heliocentric distance to the interaction point is calculated from the free path, and the pitch angle of the proton before the interaction is determined from the heliocentric distance. The next stage is concerned with the calculation of the scattering angle of the proton, and the pitch angle after the interaction is found. The procedure is repeated until the proton leaves the relevant region of space ($R \approx 10^{-2} - 2.0$ a.u.). Having analyzed

a sufficient number of protons in this way, we find the angular and the time dependence of the proton intensity at a distance of 1 a.u. from the Sun. We ignored the transverse diffusion of protons. In terms of starting assumptions, this corresponds, e.g., to uniform injection of protons into a field tube whose width is large compared to the Larmor radius.

We analyzed the motion of protons in the interplanetary field for three values of the transport length, Λ = 1.0, 0.3, and 0.1 a.u. Calculations show that the fundamental characteristic features of the time dependence of the proton bursts are determined by the transport length Λ, irrespective of the particular choice of the free path length l and the mean scattering angle σ. At first, instantaneous injection of protons was assumed. (The results of some calculations carried out assuming instantaneous injection were published in /4/.) Figure 1 shows histograms of the proton distribution angles for Λ = 1.0 a.u. The vertical axis gives the number of protons crossing a field line at a point with heliocentric distance R = 1.0 a.u. in a range of angles $\Delta\theta$ = 30°. We see from Figure 1 that in the high-intensity phase of the burst, the bulk of the protons at a distance of 1 a.u. cross the field line with pitch angles between 30 and 60°. (Our distribution refers to pitch angle intervals. If we change over to solid angles, the maximum of the distribution shifts, as expected, to 0 – 30°.) Eventually the protons fill uniformly the front hemisphere, and an isotropic distribution is finally established.

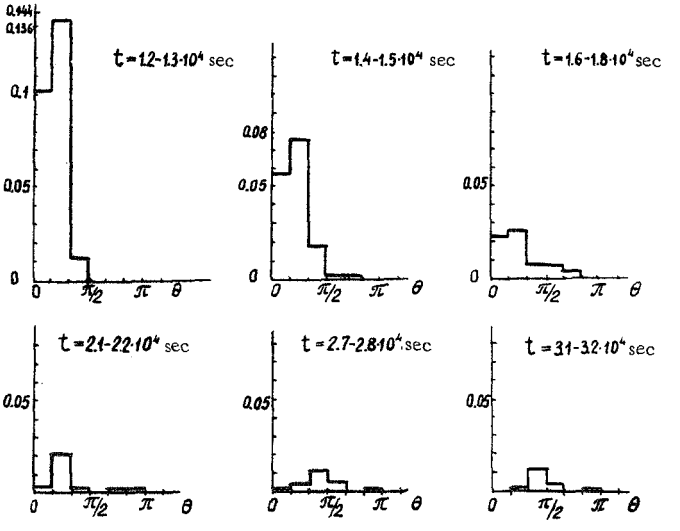

FIGURE 1. Angular distribution of 1.5 MeV protons at various times. Instantaneous injection.

Our calculations give the conditions of applicability of the diffusion theory to proton transport. Figure 2 is the time curve of the proton intensity at a distance of 1.0 a.u. for transport lengths Λ = 1.0 and 0.1 a.u. (for Λ = 1.0,

the results were obtained from two independent series of tests, designated by dots and circles). The solid curves correspond to the diffusion theory. Figure 2b shows that for $\Lambda = 0.1$ a.u. the diffusion theory gives a fair approximation to the results of our calculations. For $\Lambda = 1.0$ a.u. (Figure 2a), proton transport cannot be described in terms of the diffusion theory. In this case, our results considerably deviate from the diffusion-theoretical curve. Moreover, according to the diffusion theory, the intensity maximum is attained before the direct arrival of protons (10^4 sec). Note that calculations made with $\Lambda = 0.3$ a.u. do not fit the diffusion theory either.

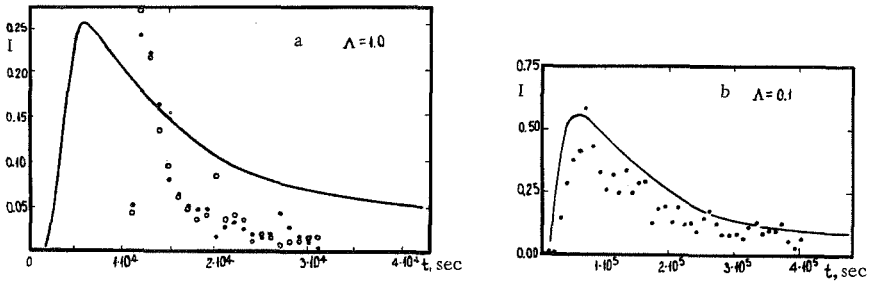

FIGURE 2. Time curves of intensity for different transport lengths:

a) $\Lambda = 1.0$ a.u., b) $\Lambda = 0.1$ a.u.

Anisotropy is an important characteristic of the proton distribution. Figure 3 plots the calculated time curve of the ratio of the intensity of the particles moving away from the source I_+ to the intensity of the particles moving toward the source I_- at a heliocentric distance R = 1.0 a.u.

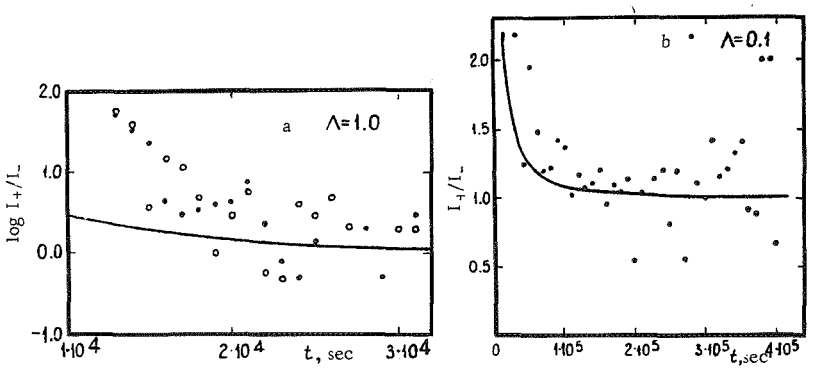

FIGURE 3. The ratio of the number of protons moving away from the Sun I_+ to the number of protons moving toward the Sun I_- for different transport lengths. Instantaneous injection.

a) $\Lambda = 1.0$ a.u., b) $\Lambda = 0.1$ a.u.

For transport lengths $\Lambda = 0.1$ a.u. (Figure 3b), which are small compared to the heliocentric distance, the distribution is nearly isotropic during the entire burst, except for the initial phase. This result is in good agreement with the diffusion theory (solid curves). For $\Lambda = 1.0$ a.u. (Figure 3a), the anisotropy is very high ($I_+/I_- = 10$) during the entire burst.

Bursts of cosmic rays of solar origin experimentally detected at distances of about 1 a.u. from the Sun show great variety. The duration of the burst and the anisotropy of the proton distribution greatly vary in different particular cases. Of particular interest are the highly anisotropic proton bursts with $A \sim 50-80\%$ ($A = (I_+ - I_-)/(I_+ + I_-)$) which persist for a few days. According to our calculations carried out assuming a constant transport length, a burst with a considerable anisotropy should be observed for transport lengths comparable with the heliocentric distance, i.e., $\Lambda \approx 1$ a.u. However, if the protons are injected instantaneously, the burst duration is short, about 10^4 sec. To obtain a burst duration of a few days, different injection conditions should be assumed, or alternatively the transport length should be taken as a function of the distance. Retaining a constant transport length, we considered the case of extended injection of protons, which continued at a uniform rate for $5 \cdot 10^4$ sec. In this problem, the dependences obtained under the assumption of instantaneous injection are functions of the source. Figure 4 plots the results of calculations for $\Lambda = 1.0$, 0.1 a.u.

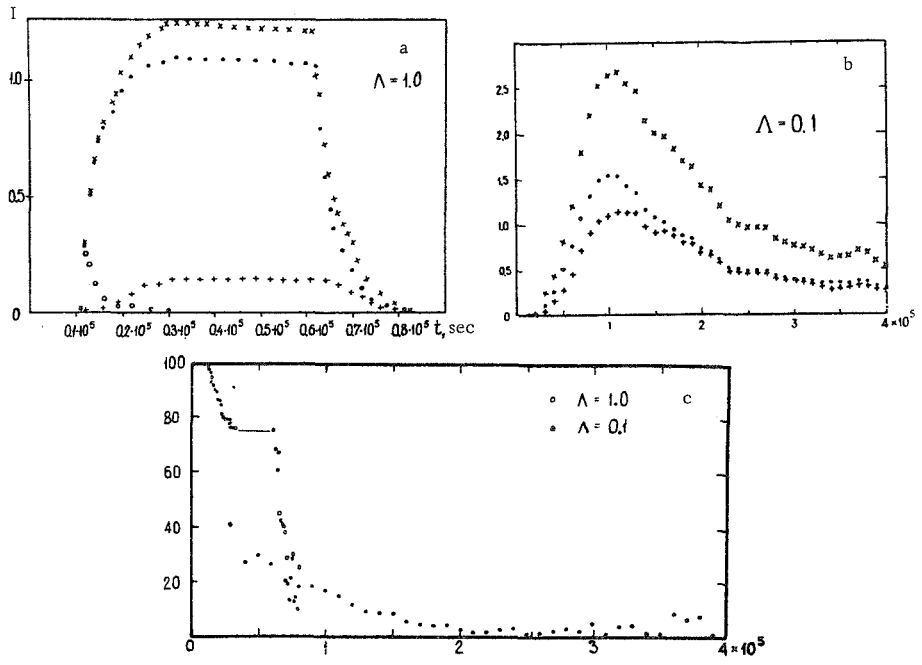

FIGURE 4. Time curves of I, I_+, I_- (a, b) and anisotropy $A = (I_+ - I_-)/(I_+ + I_-)$ (c). Uniform injection for $5 \cdot 10^4$ sec.

x — total intensity of protons, o — intensity of protons moving away from the Sun, + — intensity of protons moving toward the Sun.

As could be expected, the characteristic features of a proton burst from an instantaneous source are transferred to the case of continued injection: transport lengths $\Lambda = 0.1$ a.u. which are small compared to the heliocentric distance R = 1.0 a.u. correspond to long bursts of low anisotropy (Figure 4b), whereas transport lengths $\Lambda = 1.0$ a.u. give short bursts of high anisotropy (Figure 4a). Note that for $\Lambda = 1.0$ a.u. the anisotropy is high during that phase of the burst when the proton intensity is high (Figure 4c). It seems that the observed highly anisotropic proton bursts which persist for a few days /3/ can be attributed to prolonged injection of protons followed by propagation in a medium with $\Lambda = 1.0$ a.u. As the recorded proton bursts show a great variety of intensity time curves, the duration of injection should be determined for each particular case separately.

Bibliography

1. Vernov, S.N., A.E. Chudakov, P.V. Vakulov, Yu.I. Logachev, G.P. Lyubimov, and N.V. Pereslegina.— Izvestiya AN SSSR, Ser.fiz., 31(8):1255. 1967.
2. Charakhch'yan, A.N. and T.N. Charakhch'yan.— Geomagnetizm i aeronomiya, 6(3):406. 1966.
3. Vernov, S.N., A.E. Chudakov, P.V. Vakulov, E.V. Gorchakov, N.N. Kontor, S.N. Kuznetsov, Yu.I. Logachev, G.P. Lyubimov, A.G. Nikolaev, N.V. Pereslegina, and B.A. Tverskoi.— Trudy V Vsesoyuznoi ezhegodnoi zimnei shkoly po kosmofizike, Apatity, p.5, Izd. Kol'skogo filiala AN SSSR. 1968.
4. Getselev, I.V., E.V. Gorchakov, and G.A. Timofeev.— Trudy Mezhdunarodnogo simpoziuma sotsialisticheskikh stran po solnechno-zemnym svyazyam, Izd. KrAO. 1968.

INVESTIGATION OF PROTON FLUXES IN THE 1.50—50 MeV RANGE WITH ZOND-4 AND ZOND-5 AUTOMATIC INTERPLANETARY STATIONS

M. M. Bredov, A. A. Kolchin, V. V. Lebedev, and G. P. Skrebtsov

Investigation of low-energy cosmic rays has yielded valuable data on the structure of the interplanetary magnetic field and the mechanism of solar modulation. However, a comprehensive study of the corresponding phenomena in the interstellar space is impossible without periodic measurements of the solar activity. The bulk of reports published on the subject were based on data collected in periods of minimum solar activity /1, 2, 3/. Later findings are reported in one source only /4/.

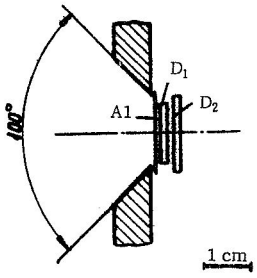

FIGURE 1. Schematic diagram of the PS-1 instrument.

The ZOND-4 and ZOND-5 interplanetary stations were launched on 2 March and 15 September 1968, respectively. Each remained in orbit for about 7 days. The payload included equipment for measuring proton fluxes between 1.5 and 50 MeV. One of the instruments, PS-1 device (Figure 1), was a sandwich of two Li-drifted silicon detectors. One of the two detectors (D2) was connected with the other detector D1 by an anticoincidence circuit. D1 had an area of 1.5 cm^2, D2 an area of 2.5 cm^2; the thickness of these detectors was 2.3 and 1.5 mm, respectively. The detectors were screened from light by aluminum foil. An electronic circuit isolated pulses corresponding to detection of protons between 1.5 — 10 and 10 — 20 MeV by D1. The geometrical factor of the instrument was 3.9 cm^2 sterad.

The other instrument (Figure 2) was a telescope (PT) comprising two identical Li-drifted silicon detectors D3 and D4, 1.2 mm thick and 2.5 cm^2 in area each. The opening angle of the sensitive cone was 100°. A1, A2, and A3 are aluminum absorbers. An appropriate choice of the absorber thickness and the height of the discrimination thresholds made it possible to record protons of 30 — 35 MeV and 45 — 50 MeV.

Figure 3 shows the proton detection efficiency of the telescope vs. the kinetic energy of the proton. Note that the discrimination thresholds in this telescope were so chosen that the instrument responded to protons only, and not to any other particles.

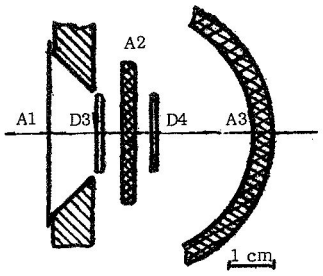

FIGURE 2. Schematic diagram of the PT instrument.

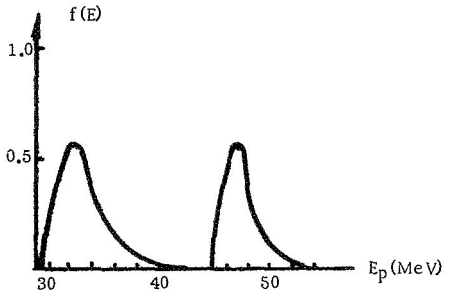

FIGURE 3. Proton counting efficiency vs. the kinetic energy.

The proton measuring equipment was oriented so that the instruments in the spinning interplanetary station scanned mainly in a plane perpendicular to the plane of the ecliptic. Over certain sections of the trajectory, however, midcourse maneuvers were carried out and the orientation changed. In the present report, we mainly consider the results obtained with ZOND-5.

The proton measuring equipment was turned on after the boost stage, when the station was on its course to the Moon. The first data were obtained at a distance of 22,000 km from the Earth, when the station was crossing the outer radiation belt. The PS-1 channel (1.5 — 10 MeV) recorded a high counting rate which fluctuated (increasing and decreasing) as the station was moving away from the Earth, and then gradually settled to the level measured outside the magnetosphere. The PT-1 and PT-2 channels (30 — 35 MeV and 45 — 50 MeV, respectively) did not register an increased count rate in the radiation belt. Brief "bursts" of the counting rate, which did not last more than a minute, were picked up in the PS-1 channel all the way to a distance of about 100,000 km from the Earth. Measurements carried out from this distance to the time when the equipment was turned off at a distance of about 80,000 km from the Earth on the way back are described in the following. The measurement data apparently characterize the conditions in the "free" interplanetary space between the Earth and the Moon which prevailed between 16 and 21 Sept. 1968. Figure 4 plots the time variation of the count rate as recorded on 19 Sept. 1968 from 03^h20^m to 04^h05^m in three channels at a distance of about 350,000 km from the Earth. The variation of the count rate observed during this period was typical of the entire trip. The rms error is indicated for the maximum and the minimum PS-1 reading. The statistics of the events in the PT-1 and PT-2 channels are insufficient for drawing any quantitative conclusions over times of the order of one or several minutes.

Figure 5 summarizes the data on the counting rates in the various channels for the entire period from 11^h16^m on 15 Sept. 1968 to 13^h30^m on 21 Sept. 1968. The points on this plot were obtained by averaging the readings taken over periods ranging from 45 to 140 min.

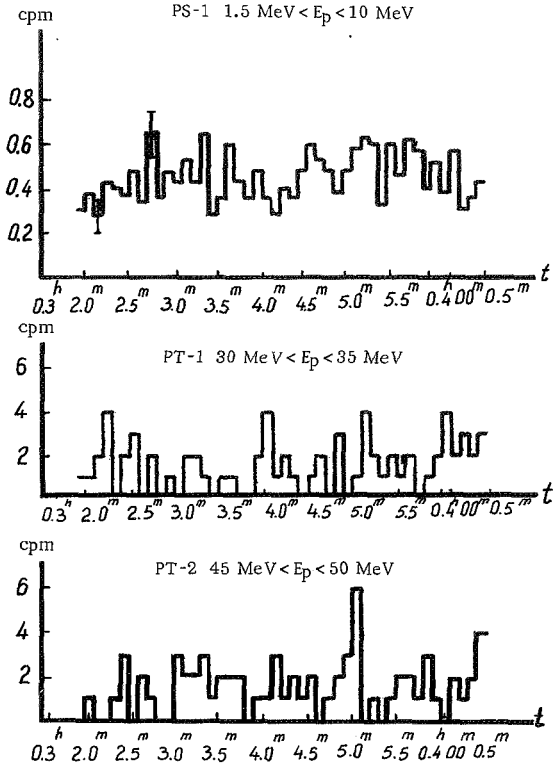

FIGURE 4. Variation of the count rate with time.

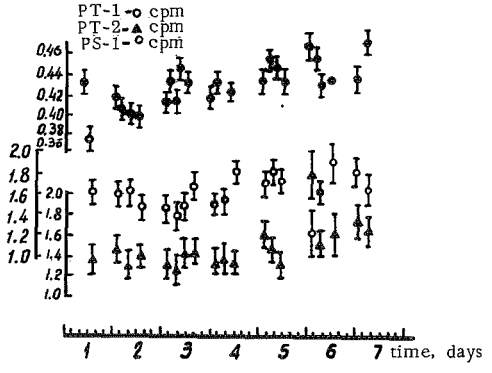

FIGURE 5. Count rate data for the period from 15 to 21 Sept. 1968.

Daily averaging brings out more clearly the slight increase in the count rate in the PS-1 channel from 0.39 to 0.46 sec^{-1} during the relevant period with a rms error of less than 0.01 sec^{-1}. The count rates in the PT-1 and PT-2 channels also showed a slight increase. On the whole, however, the instruments did not detect any significant change in the count rate between 15 Sept. and 21 Sept. 1968 which could have been attributed to a radical change in the physical conditions in the Earth—Moon space.

The relatively short duration of the proton stream records (ZOND-5 landed on 21 Sept. 1968) makes it impossible to decide what the instruments measured exactly, whether the "quiet" background between flares or perhaps a gradual increase in the intensity of solar protons. Since ZOND-5 was launched in a year of maximum solar activity, the latter assumption seems quite probable.

As we have already noted, ZOND-5 sometimes changed its orientation in space as a result of midcourse maneuvers. The count rate in all the channels nevertheless remained fairly constant, and we may thus introduce for our purposes a "mean intensity" of the proton stream, which is directly related (through the geometrical factor of the instrument) to the mean count rate. This approach is essentially equivalent to the assumption of an isotropic proton flux during the averaging period.

We give here the mean proton intensities obtained in our experiments:

1.5—10 MeV	—	$I = 0.9 \cdot 10^3$ m^{-2} $sterad^{-1}$ sec^{-1}
10—20	—	$I = 40$
30—35	—	$dI/dE = 35$ m^{-2} $sterad^{-1}$ sec^{-1} MeV^{-1}
45—50	—	$dI/dE = 50$

The intensities recorded by ZOND-4 in March 1968 fall somewhat below these values.

Bibliography

1. Vernov, S.N., A.E. Chudakov, P.V. Vakulov, Yu.I. Logachev, G.P. Lyubimov, A.G. Nikolaev, and N.V. Pereslegina.— DAN SSSR, 171:847. 1966.
2. van Allen, J.A., L.A. Frank, S.M. Krimigis, and H.K. Hills.— Science, 149:1228. 1965.
3. Fan, C.Y., M. Pick, K.R. Pyle, J.A. Simpson, and D.R. Smith.— J. Geophys. Res., 73:1555. 1968.
4. Grigorov, N.L., V.G. Kurt, V.N. Lutsenko, V.L. Madyev, N.F. Pisarevskii, and I.A. Savenko.— Kosmicheskie Issledovaniya, 7:137. 1969.

DYNAMIC ALIGNMENT OF ATOMIC AND MOLECULAR SPINS AS A NEW METHOD OF DETERMINATION OF THE INTERPLANETARY MAGNETIC FIELD

D. A. Varshalovich

The state of atoms, molecules, and ions in various astrophysical systems is generally characterized by their concentration, velocity distribution, and degree of ionization or excitation, but no information is given concerning the spin state of the particles. The spins are assumed to be randomly distributed, without interacting with any other systems. This assumption, however, is valid in isolated cases only.

STATIC AND DYNAMIC SPIN ALIGNMENT

A rarefied medium in thermodynamic equilibrium in the absence of external fields is isotropic. All directions in this medium are equivalent, so that the particle energy cannot depend on the orientation of the particle spins in space. Particles differing only in the projection M of the spin $\vec{I}$ on the quantization axis have the same energy

$$\varepsilon_M = \varepsilon_{M'}, \tag{1}$$

for any allowed M and M' (I, I − 1, I − 2, . . . , −I). As a result, from Boltzmann's equation,

$$\frac{R_M}{R_{M'}} = e^{-\frac{\varepsilon_M - \varepsilon_{M'}}{kT}}, \tag{2}$$

the population R_M of all the (2I + 1) states corresponding to different spin orientations is constant, i.e., all the possible values of the spin projection M are equiprobable. In other words, the spins are entirely randomized and the medium as a whole is isotropic. This situation obtains, e.g., in the dense atmospheric layers, where the population of the various energy levels is determined by collisions of the particles with the equilibrium gas.

The spins of the particles in a medium in thermodynamic equilibrium can be aligned by a sufficiently strong external field, such that the magnetic energy is greater than or comparable with the thermal energy:

$$\mu H \geq kT. \tag{3}$$

In this case, the energy levels of the particles are split into (2I + 1) sublevels characterized by different M values, and in accordance with the

Boltzmann equation (2) the populations of these sublevels are all different. The maximum population is characteristic of the lowermost sublevel, the one with M = 1 if the magnetic moment of the particle is positive $\mu>0$, or M = −1 if $\mu< 0$. This implies that the particle spins are preferably aligned along the field $\vec{H}$ (or against the field). This is known as the case of static alignment. The necessary condition of static alignment, (3), is hardly ever satisfied in the known astrophysical systems. For example, in the interstellar medium, for $H\sim 10^{-6}$ Oe and $T\sim 100°K$, $\mu H\sim 10^{-26}$ erg, whereas $kT\sim 10^{-14}$ erg. Even in magnetic stars, with $H\sim 10^{3}$ Oe and $T\sim 10^{4}°K$, $\mu H\sim 10^{-17}$ erg and $kT\sim 10^{-12}$ erg. Therefore, static spin alignment associated with strong external fields is impossible in outer space.

In non-equilibrium media, however, an entirely different alignment mechanism is possible — the so-called dynamic spin alignment, whereby the particle spins are aligned through interaction with a directional beam of radiation or a stream of fast particles passing through the medium /1/. Thus, the optical emission and the radio waves from stars and nebulae, as well as beamed corpuscular streams piercing the interstellar medium, interact with the interstellar particles changing their momentum distribution and also aligning their spins. The momentum effects (radiation pressure and solar wind) are freely discussed in astrophysical literature, whereas the problem of the dynamic alignment of atomic and molecular spins in the interstellar medium has been ignored so far. And yet, both effects are closely interrelated, since both linear momentum and angular momentum are transferred in collisions. Angular momentum transfer is even more effective in the sense that the incident beam first aligns the medium particles and only then drags them along.

The fundamental reason for the dynamic spin alignment is to be sought in the spin-spin and spin-orbit interaction of the particles with the incident stream (photons, protons, electrons, etc., either polarized or nonpolarized). This interaction, however, may lead to spin alignment only if the angular distribution of the incident particles is anisotropic. Thus, a directed beam of unpolarized light scattered by a random medium will produce spin alignment even if the angular scattering function is spherically symmetric. The resonance scattering of photons is the most effective for spin alignment, since the resonance scattering cross section is exceptionally high and also because the photon spin s = 1ħ is always directed along (or against) the direction of wave propagation (transversality of electromagnetic waves). The angular distribution of particles is generally isotropic, whereas radiation fluxes are mostly anisotropic.

NECESSARY CONDITIONS AND THE MECHANISM OF OPTICAL SPIN ALIGNMENT

The analysis of conditions in various astrophysical systems has shown that resonance scattering of directional fluxes of unpolarized radiation constitutes the main process of spin alignment in outer space /2/. The necessary conditions for this optical dynamic spin alignment are encountered in numerous astrophysical systems, such as the interstellar

and interplanetary medium, nebulae, outer layers of stellar and planetary atmospheres, comets, etc. The main distinctive feature of all these systems is that their density is low and the collisions are ignorable,

$$W_{col} < W_{rad}, \tag{4}$$

whereas the radiant fluxes are very powerful and essentially anisotropic,

$$\frac{\Delta\Omega}{4\pi} \ll 1, \tag{5}$$

since the optical thickness is low,

$$\tau < 1. \tag{6}$$

Under these conditions resonance scattering will inevitably lead to spin alignment. We may therefore maintain that, unlike the static spin alignment, the dynamic alignment is an exceedingly widespread natural phenomenon. In laboratories, dynamic spin alignment is very difficult to create and it can be sustained even for very brief periods of time only by means of special experimental setups /3/. The spin system rapidly relaxes to an isotropic equilibrium state. On the other hand, the necessary conditions for optical spin alignment are always observed in tremendous regions of outer space. Nature itself constantly maintains the alignment. The mechanism of optical resonance spin alignment is illustrated by the simple and vivid example of a two-level atom with spin I = 1 in the ground state and spin I' = 0 in the excited state (Figure 1).

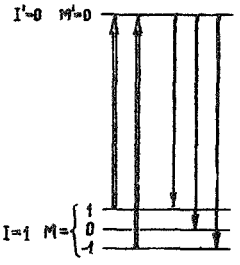

FIGURE 1. Level diagram illustrating the mechanism of optical spin alignment. I = 1 and I' = 0 are the particle spins in the ground and the excited state, respectively. M is the projection of the spin on the direction of the incident photon beam.

If the incident light is unpolarized, the beam contains right- and left-polarized photons in equal proportions. These photons are characterized by different projections of their angular momentum on the quantization axis, $m_\gamma = 1$ and $m_\gamma = -1$. There are no photons with $m_\gamma = 0$, because of the transversality of the electromagnetic field.

In virtue of angular momentum conservation, a resonance photon with $m_\gamma = \pm 1$ can be absorbed only by an atom with $M = \pm 1$, bringing it to an excited state with $M' = M + m_\gamma$; atoms in substate M = 0 cannot be excited by this mechanism. Therefore, atoms occupying the substate M = 0 can be excited to a state with a different M value only by collisions among themselves. On the other hand, excited atoms may drop with equal probability to all the M substates, since I = 0 and all the physical properties of a spin-zero system are independent of its spatial orientation; in particular, the matrix elements which determine the transition probabilities are independent of the projections m_γ and M. Thus, each scattering event increases the population of the M = 0 level and consequently the population of the $M = \pm 1$ levels is steadily depleted. If the system is subjected for a sufficient length of time to a beam of resonance photons, virtually all the atoms will be converted to a substate with M = 0, irrespective of their

initial spin alignment, and the medium will become transparent to the resonance radiation. Complete transparency of the medium is of course attainable only if there are no interatomic collisions. It is moreover assumed that the resonance radiation is directed in a narrow solid angle along the quantization axis. Note that the loss of opacity in this case is entirely different from the phenomenon observed in intense radiation fluxes, when the populations of the upper and the lower levels become equal; here the medium becomes transparent following the alignment of spins of the atoms in the lower level, an effect observable even in low-intensity radiation. Spin alignment does not necessarily result in complete transparency of the medium. Depending on the spins I and I' and on the angular distribution and polarization of the aligning radiation, we end up with partial loss of opacity or, conversely, partial suppression of transparency to resonance radiation. Moreover, if the ground state has a fine structure, the different magnetic sublevels of the upper state may undergo a population inversion relative to the corresponding lower sublevels as a result of spin alignment, i.e., there is a possibility of coherent amplification of the resonance radiation transmitted through the medium. This effect is possible, e.g., in the case of HI /2/ and OH /4/. Since spin alignment may substantially influence the transmission of resonance radiation, it must not be ignored in the analysis of astrophysical observations, since almost the entire body of our data on the interstellar medium (chemical composition, degree of ionization and excitation, etc.) is derived from observations of transmitted resonance radiation.

DESCRIPTION OF SPIN ALIGNMENT AND TRANSITION PROBABILITIES

Unlike static orientation, which is entirely described by a single parameter $\mu H/kT$, dynamic spin alignment is a complex function of several parameters. The spin state of particles is not always a statistical mixture of states with various M: it may also prove to be a coherent superposition. In the latter case, the spin alignment can be described only in terms of the polarization density matrix, and it is not enough to give the populations of the sublevels with different M. Under astrophysical conditions, however, we are often dealing with systems immersed in a magnetic field such that $kT \gg \mu H \gg \hbar (W_{rad} + W_{col})$, and the spin aligning radiation is a stochastic factor (without regular modulation). The polarization density matrix of atoms and molecules in this case is diagonal in M (with H taken as the quantization axis), and the atomic spin alignment can therefore be described in terms of the population of the magnetic sublevels R_{IM} in a coordinate system with the quantization axis pointing along H. These level populations are determined by the usual system of balance equations:

$$\sum_{I'M'} R_{I'M'} W_{I'M' \to IM} = R_{IM} \sum_{I'M'} W_{IM \to I'M'}, \qquad (7)$$

where $W_{IM \to I'M'}$ are the transition probabilities $IM \to I'M'$.

In every real case, we should consider the actual level diagram and the actual transition probabilities associated with all conceivable factors.

To bring out more clearly the dependence of the resonance spin alignment on the atomic spin characteristics and on the properties of resonance radiation, we will first analyze spin alignment of a system of two-level atoms without hyperfine structure. Let I be the ground-state spin, and I' the excited state spin. The probability of electric or magnetic dipole transitions under the above conditions is entirely determined by three parameters $\rho_\mu(\nu)$ — the diagonal elements of the radiation density matrix at the resonance frequency ν in a representation characterized by the μ-projection of the angular momentum of the photon on the quantization axis:

$$\begin{cases} W_{IM \to I'M'} = \gamma_0 \left(C^{IM}_{I'M' \, 1\mu}\right)^2 (1+\rho_\mu) \\ W_{I'M' \to IM} = \gamma_0 \left(C^{IM}_{I'M' \, 1\mu}\right)^2 \rho_\mu \end{cases} \qquad \varepsilon_{IM} > \varepsilon_{I'M'}, \tag{8}$$

where γ_0 is the spontaneous transition probability and $C^{IM}_{I'M'1\mu}$ are the Clebsch—Gordan coefficients. It should be stressed that the transition probabilities $W_{IM-I'M'}$ and hence the populations R_{IM} are independent of the fine features of the angular distribution and the polarization of radiation; substantially different angular and polarization states may have the same parameters ρ_μ. For isotropic unpolarized radiation

$$\rho_1(\nu) = \rho_0(\nu) = \rho_{-1}(\nu) = \frac{I_\nu \lambda^2}{h\nu}, \tag{9}$$

where I_ν is the radiation intensity ($erg \cdot cm^{-2} \cdot sec^{-1} \cdot Hz^{-1} \cdot sterad^{-1}$).

For a directional beam of polarized radiation

$$\begin{cases} \rho_{\pm 1}(\nu) = \frac{3}{2}\left(\frac{\Delta\Omega}{4\pi}\right)\left(\frac{\lambda^2 I_\nu(\vartheta)}{h\nu}\right)\left[1 \pm \eta\cos\vartheta - \frac{\sin^2\vartheta}{2}\left(1-(-)^\tau \xi \cos 2\alpha\right)\right] \\ \rho_0(\nu) = \frac{3}{2}\left(\frac{\Delta\Omega}{4\pi}\right)\left(\frac{\lambda^2 I_\nu(\vartheta)}{h\nu}\right)\sin^2\vartheta\left(1-(-)^\tau \xi \cos 2\alpha\right) \end{cases}, \tag{10}$$

where η and ξ are the degree of circular and linear polarization; ϑ is the angle between the direction of $\vec{H}$ and the beam; α is the position angle characterizing the linear polarization; $\tau = 1$ for electric dipole transitions and $\tau = 0$ for magnetic dipole transitions.

POPULATION OF MAGNETIC SUBLEVELS

Stationary populations of the magnetic sublevels R_{IM} with any I established by optical pumping through all the possible resonance sublevels, i.e., levels with I' = I − 1, I' = I, and I' = I + 1, were calculated /2/ for arbitrary angular distribution and polarization of the incident radiation. The solutions of the balance equations are shown graphically in Figure 2.

Figure 2 plots the populations of the ground-state sublevels R_{IM} for the principal astrophysical cases of spin alignment by low-intensity unpolarized radiation ($\rho_\mu << 1$). The values of R_{IM} are plotted in polar coordinates as a function of the angle θ between the spin aligning beam and the field vector H for various spin values I and I'. The circle marks

the equilibrium populations R_{IM} for any M which are established in an isotropic medium in the absence of directional radiation beams and particulate fluxes. Figure 2 clearly illustrates the changes in the character and the degree of spin alignment with increasing I for integer and half-integer values for various combinations of I and I'. It is also seen that the populations R_{IM} for $I \geqslant 1$ differ from the equilibrium values for any direction of the aligning beam, except $\vartheta \approx 55°$, when $\sin^2 \vartheta = 2/3$ and $\rho_1 = \rho_0 = \rho_{-1}$. In the case $I' = I - 1$ and $\vartheta = 0$, the maximum population is characteristic of the sublevels with the minimum $|M|$ (0 or $1/2$), whereas for $\vartheta = \pi/2$, conversely, the levels with $|M| = 1$ have the largest population. In particular, for $I = 1$ and $\vartheta = 0$, all the atoms are concentrated on the $M = 0$ sublevel.

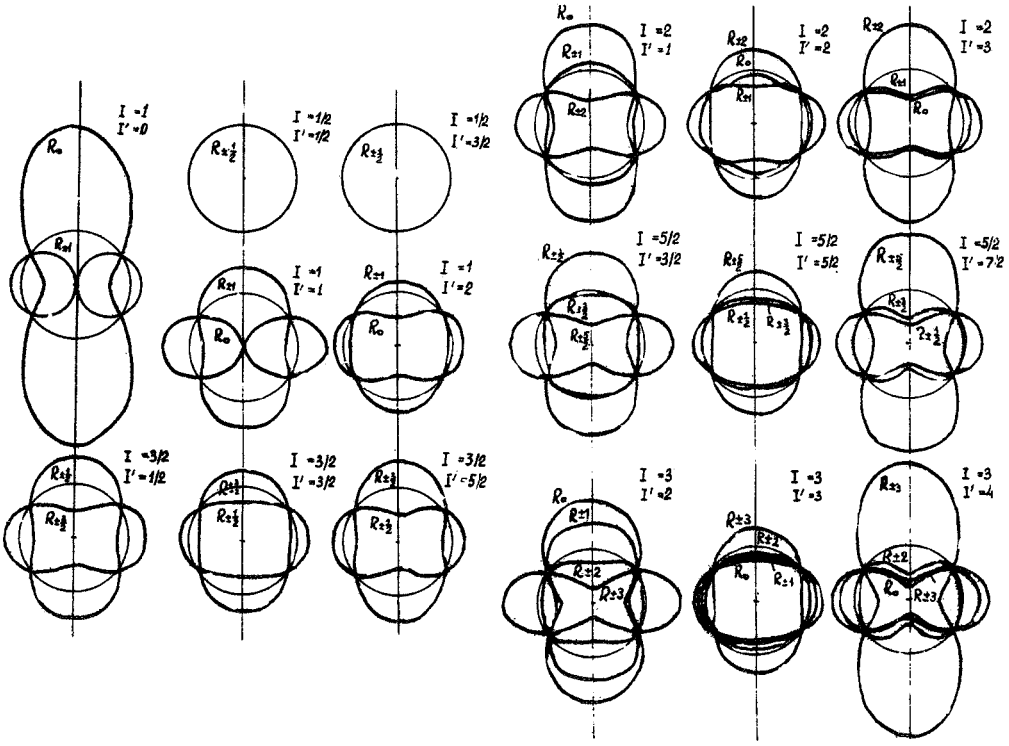

FIGURE 2. The population of the ground-state sublevels R_{IM} established by optical pumping in a beam of unpolarized radiation directed at an angle θ to the magnetic field (polar coordinates; I and I' are the spins of the ground state and the excited state, respectively).

It is also significant that for $I >> 1$ and $I' \geqslant I + 1$, $\theta = 0$, virtually all the atoms are concentrated in the state with $|M| = 1$. This case is significant for the problem of optical spin alignment by molecules with a rotational structure of energy levels. Figure 2 makes it possible to find the populations R_{IM} in a more general case, when the radiation has an arbitrary angular distribution and an arbitrary degree of linear polarization, since then the entire dependence is determined by a single parameter, the ratio

of $\rho_+ = \rho_-$ to ρ_0 corresponding to a well-defined value of the angle θ:

$$\rho_+/\rho_- = \frac{1}{2}(\sec^2\theta - 1). \quad (11)$$

The results of calculations shown in Figure 2 permit assessment of populations of the magnetic sublevels of the ground state R_{IM} in a multilevel system under optical pumping by a continuous-spectrum radiation, without solving the balance equations. If the resonance levels with equal I' play the main role, the resulting populations R_{IM} are the same as for a single resonance level with I', irrespective of the actual number of the resonance levels. In a general case, on the other hand, the relative contributions from all the resonance levels with I' = I − 1, I' = I, and I' = I + 1 should be known.

The preceding results also make it possible to evaluate the spin alignment of atoms and molecules as a result of their interaction with a directed beam of fast electrons or protons, since the field of a fast charged particle is largely equivalent to the field of a transverse electromagnetic wave.

A METHOD FOR DETERMINING THE DIRECTION OF $\vec{H}$

Allowance for spin alignment of atoms and molecules in the interstellar medium introduces significant corrections in the determination of partial density, degree of excitation, etc. It also provides, however, qualitatively new information on the anisotropy of physical conditions in a given astrophysical system and primarily on the anisotropy of the radiation field. The dependence of the populations R_{IM} of the magnetic sublevels established by optical pumping on the direction of the magnetic field $\vec{H}$ enables us to apply this effect to the determination of the direction of $\vec{H}$ in a given region of space. This method is applicable to the case of weak fields, when all other optical methods fail. Let us consider a particular example.

The D_1 (λ = 5896 Å) and D_2 (λ = 5890 Å) lines in the spectrum of comets are produced by single scattering of the solar radiation by the Na I atoms in the cometary atmospheres. The intensity ratio of these lines clearly depends on the scattering angle, i.e., it is determined by the differential scattering cross sections. The D_1 line is unpolarized, and its angular distribution function is spherically symmetric, irrespective of the direction of the field $\vec{H}$ or the occupancy of the magnetic sublevels R_{FM}. The situation is different for the D_2 line: this line shows partial linear polarization. The degree of polarization and the angular distribution function of D_2 are significantly anisotropic and both depend on the occupancy R_{FM} of the hyperfine-structure magnetic sublevels F = 1 and F = 2($3S_{1/2}$) of the Na I ground state. The spins of the Na I atoms in the cometary atmosphere are aligned through the scattering of the resonance solar radiation.

We calculated the occupancies R_{FM} of the magnetic sublevels F = 1 and F = 2($3S_{1/2}$). All the resonance levels of Na I were taken into consideration and allowance was made for the interference effects associated with the partial overlap of the hyperfine structure sublevels of the excited states. The table lists resulting R_{FM} values for the two extreme cases: with $\vec{H}$ directed along the comet—Sun radius-vector ($\theta = 0°$ or $\theta = 180°$) and at right angles to this radius-vector ($\theta = 90°$). For $0 < \theta < 90°$ (or $180° > \theta > 90°$), R_{FM} varies monotonically between its extreme values, reaching $R_{FM} = 1.000$ at

$\theta \simeq 55°$. We see from the table that natural optical pumping may shift the occupancies R_{FM} of the individual sublevels by as much as 30% from the corresponding equilibrium values. The R_{FM} values are uniquely related to the angular distribution of the two linearly polarized components of the D_2 line. Measuring the D_1/D_2 intensity ratio and the degree of polarization of D_2, we can find the two angles characterizing the effective direction of $\vec{H}$ in the part of the interplanetary space where the head of the comet moves at the given time. In this case, the Doppler line width $\nu_0(v_T/c) \sim 10^8 - 10^9$ Hz is much greater than the Zeeman splitting $\mu H/h \sim 10^2$ Hz. Therefore, the usual optical method of measuring $\vec{H}$ from the degree of circular polarization at the line wings is inapplicable in practice. The magnitude of $\vec{H}$ can be found by measuring the rotation of the plane of polarization; in the absence of $\vec{H}$ the scattered radiation is polarized at right angles to the scattering plane, whereas in the presence of $\vec{H}$ the plane of polarization is turned through an angle $\Delta\alpha \sim \mu H_1 \tau/\hbar$, where H_1 is the component of $\vec{H}$ in the direction of observation, and τ is the lifetime of the atom in the excited state. Lines with large lifetimes τ should be used in this case.

It is hoped that continuous measurements of relative line intensities and line polarizations in the spectra of comets at various points of their orbit will eventually establish the exact extent of the regular magnetic field around the Sun. Note that direct measurements from space vehicles are practicable only inside a fairly small region near the Earth's orbit, whereas comets provide us with a much simpler and cheaper probe for studying the magnetic field geometry over distances from about 0.3 a.u. to about 3—5 a.u., both inside and outside the plane of the ecliptic.

R_{FM} values for $\theta=0°$ and $\theta=90°$

F, M	R_{FM} (θ = 0°)	R_{FM} (θ = 90°)
2, ±2	1.306	0.878
2, ±1	0.845	1.037
2, 0	0.787	1.139
1, ±1	0.999	1.011
1, 0	0.913	1.020

Bibliography

1. Kastler, A.— J. Phys. et radium, 11:255. 1950.
2. Varshalovich, D.A.— Astronomicheskii Zhurnal, 42:557. 1965; ZhETF, 52:242. 1967; Astrofizika, 4:519. 1968; ZhETF, 59:535. 1969.
3. Bernheim, R. Optical Pumping. New York. 1965.
4. Perkins, F., J. Gold, and E. Salpeter.— Astrophys. J., 145:361. 1967.

RADIATION TRANSFER IN SPACE PHYSICS

Yu. N. Gnedin and A. Z. Dolginov

I. Space physics is one of the most rapidly developing areas of modern science, using a wide range of theoretical and experimental methods. One of the principal subdivisions of space physics deals with the problems of interaction of radiation with matter in the interplanetary space, where the term "radiation" covers both optical and corpuscular radiation, such as hard gamma quanta, electrons, neutrons, protons, etc. The problem of interaction of radiation with matter is one of the traditional subjects in physics, known as the theory of radiation transfer. We distinguish between three classical directions in the theory of radiation transfer. One of these, which has received its maximum development in astrophysics, is concerned with the transmission of visible light (the optical range of wavelengths) through the atmospheres of stars, planets, and nebulae /1, 2/. Another direction, more closely related to the physics of nuclear reactors, deals with the moderation and thermalization of neutrons in solid and gas targets /3–5/. Finally, the third direction investigates multiple scattering of electrons in thick targets /6/. Each of these directions operates with its own tools, which are only seldom applicable to the other directions.

The problem of radiation transfer in space physics differs from the classical theory of radiation transfer not only in terms of the specific physical conditions but also in the more general formulation of the problem and the application of more general methods. This is so primarily because in space physics we are dealing with a wide range of various radiations covering a wide spectrum of energies (the classical methods of the theory of radiation transfer are always adapted to one particular type of radiation in a definite range of energies). Another reason is provided by the specific conditions prevailing in outer space: the interplanetary magnetic field and the interplanetary plasma are highly significant factors.

The characteristic features of radiation transfer in space physics emerge most vividly in the following problems:

1. The problem of propagation of galactic and solar cosmic rays through the interplanetary magnetic field. A detailed analysis of this problem was given in /7–10/.

2. The study of the generation mechanisms of various plasma waves and their propagation through the solar and the interplanetary plasma. A number of topics related to this problem were considered in /11, 12/. Some topics associated with the transmission of solar radiation through planetary atmospheres and the construction of models of planetary atmospheres are treated in /13, 14/.

3. The investigation of physical processes in cometary atmospheres, which is closely linked with the general problem of interaction of radiation with an expanding gas in a vacuum. The solution of this problem for comets was given in /15/.

We will consider in detail the following two problems.

The determination of the composition of planets and other celestial bodies is one of the most important tasks of space physics. The necessary information is obtained by measuring the total flux and the energy spectrum of radiation leaving the surface of the celestial body. The outgoing radiation may originate either from the decay of radioactive elements entering the composition of the planets or from the interaction of the planetary material with hard solar radiation and cosmic rays. The cosmic rays hitting the planet trigger certain nuclear reactions whose products are neutrons and hard gamma radiation. Significant information can be obtained by measurements of the neutrons produced in the surface layer. The validity of the method of measurement of surface radiations for obtaining information on the chemical composition of planets, in particular lunar rocks, was indicated in a number of published studies /16–20/ and in the paper by S.V. Viktorov, G.V. Kir'yan, and G.E. Kocharov at the Fifth All-Union School of Space Physics in Apatity (1968).

Orbiting stations and space vehicles have by now measured the X-ray and the gamma-ray spectrum of the lunar surface. The results of these measurements were published in /21, 22/.

Neutron measurements probe the composition of surface rocks to a much greater depth than the analysis of other radiations does. Neutrons are moreover highly sensitive to the presence of hydrogenous material. Observations of the neutron flux from planets shrouded in thick atmospheres, carried out outside the Earth's atmosphere, will provide valuable information on the composition of the planetary atmospheres. The problem thus reduces to the determination of the spectrum and the angular distribution of the neutrons emitted by the planetary surface.

The second important problem is concerned with the interaction of protons with the Earth's atmosphere. Protons penetrating into the atmosphere cause Balmer emission in the polar aurorae. Observations established that the H_α, H_β, and H_γ lines had wide contours which could be interpreted as Doppler broadening of the spectral lines of atomic hydrogen produced as a result of charge exchange processes between the protons and the atmospheric atoms and molecules. Extensive literature has been published /23, 24/ in which the energy and the angular distributions of the incoming protons is derived from the observed profiles of hydrogen emission lines. The reliability of the proton energy distributions recovered in this way is highly questionable, however: on the one hand, our knowledge of the effective cross sections of a number of processes which play an important role in the generation of moving excited hydrogen atoms is deficient and, on the other hand, the entire problem of distribution of protons and neutral hydrogen atoms in multiple charge exchange processes has not been solved. The difficulty is that protons interacting with the atmospheric gases capture electrons from the gas atoms and are thus converted to hydrogen atoms. The hydrogen atoms formed in this way change the direction of their linear momentum and lose energy while interacting with the target atoms, become ionized again, and so on.

Since at energies below 30 keV the charge exchange cross section for protons with the atoms of various gases is several times greater than the ionization cross section of atomic hydrogen, the proton spends a substantial proportion of its life as a neutral hydrogen atom, colliding several times with the target atoms. Multiple scattering of neutral hydrogen atoms therefore significantly influences the energy and the angular distribution of protons in the medium. The determination of the energy spectrum of protons penetrating into the upper atmosphere near the poles is of great importance in the physics of the atmosphere and nearby space. Once this spectrum is determined, we will be able to assess the effect of the auroral protons in the heating up and ionization of the polar upper atmosphere.

Finally, another important problem in the physics of interplanetary space is concerned with the interaction of ultraviolet radiation of the Sun ($L_y - \alpha$) with the interplanetary neutral hydrogen. Observations of the scattered $L_y - \alpha$ radiation so far provide the only source of information concerning the neutral hydrogen in the space around the Sun. Some topics pertaining to this problem were considered in /25/. Thus, even a partial listing of the main problems of space physics immediately reveals the significance of multiple scattering, or radiation transfer.

II. Multiple scattering is generally described by the so-called transfer equation, which is derived from considerations of particle flux balance:

$$\vec{n}_1 \nabla I_i(\vec{r}, \vec{P}_1) = -N_0 \sigma_{oi}(P_1) I_i(\vec{r}, \vec{P}_1) + \sum_{\kappa} \int d\vec{p}\, W_{i\kappa}(\vec{P}_1, \vec{p}) I_\kappa(\vec{r}, \vec{p}) + Q_i(r, \vec{P}_1). \qquad (1)$$

Here $I_i(\vec{r}, \vec{P}_1)$ is the intensity of the scattered particles. It gives the number of particles (photons, electrons, atoms) in a given state i with momentum $\vec{P}_1$ passing in unit time through a unit area at point $\vec{r}$ at an angle ϑ_1 to the given direction $\vec{n}_0$;

$$W_{i\kappa}(\vec{P}_1, \vec{p}) = \frac{N_0 (1+\gamma)^2}{m P_1} \sigma_{i\kappa}(\vec{P}_1, \vec{p}) \delta\left[\frac{P_1^2}{2m} - \frac{p^2}{2m} + \frac{(\vec{P}_1 - \vec{p})^2}{2M} + \varepsilon_i - \varepsilon_\kappa \right], \qquad (2)$$

where $W_{i\kappa}$ is the transition probability of the incident particle from state κ with momentum $\vec{p}$ to state i with momentum P_1; δ is a function which ensures the conservation of energy in single scattering; $\sigma_{i\kappa}$ is the differential cross section for the transition of the particle from state κ with momentum $\vec{p}$ to state i with momentum $\vec{P}_1$. It is related in the usual way to the quantum-mechanical transition amplitude A of the particle:

$$\sigma_{i\kappa}(\vec{P}_1, \vec{p}) = \sum_n A^*_{in}(\vec{P}_1, \vec{p}) A_{n\kappa}(\vec{P}_1, \vec{p}), \qquad (3)$$

where m is the mass of the incident particles, M is the mass of the target atom.

The factor $(1+\gamma)^2 (m\vec{P}_1)^{-1}$ arises from the normalization of $W(\vec{P}_1, \vec{p})$ to a quantity equal to the reciprocal of the range of the incident particle:

$$\sum_i \int d\vec{P}_1\, W(\vec{P}_1, \vec{p}) = N_0 \sigma_0(P), \qquad (4)$$

where N_0 is the concentration of the scattering atoms in the medium.

The first term in the right-hand side of equation (1) describes the loss of particles in state i with momentum $\vec{P}_i$ as a result of collisions with target atoms, and the second term describes the addition of particles to this state. The third term $Q_i(\vec{r}, \vec{P}_i)$ describes the flux of incident particles undergoing multiple scattering (the particle source).

What are the physical quantities characterizing the transfer equation? First it follows from the transfer equation (1) that the scattering intensities add up at any point in the scattering medium (the balance of particle fluxes) and no effects are observed associated with the wave nature of the incident particles. Further, the transfer equation includes the cross sections of elementary processes. It is readily seen that if the characteristics of the medium depend only on the one coordinate x, the transfer equation is qualified by a single nondimensional combination $L(x) = \int_0^x N_0(x)\sigma_0 dx$ which is known as the optical thickness (or optical depth) in the theory of light scattering.

On the other hand, from the point of view of quantum mechanics, the interaction of a beam of particles with target atoms is a wave-mechanical effect, described as wave functions, wave packets, phases of the wave function, interference, etc. The transfer equation thus only provides an approximate description of multiple scattering, and the conditions of its applicability must be clearly formulated. Certain attempts have been made to "canonize" the transfer equations and thus use it in problems where the strict applicability conditions are not satisfied (we should be particularly careful in plasma physics). Other authors — especially astrophysicists — often try to solve the transfer equation with an excessive accuracy which does not fit within the restricted framework of its applicability.

III. We will start with the principal condition of applicability of the transfer equation: the wavelength λ of the incident radiation should be much less than the total range Λ of the particle in the medium ($\lambda \ll \Lambda$). When this condition is satisfied, waves scattered by different force centers do not interfere. Indeed, the attenuation of the incident coherent beam is caused, on the one hand, by true absorption in collisions and, on the other hand, by large-angle scattering of particles (i.e., large momentum transfer). The coherence is broken in this process, i.e., waves scattered by different force centers cannot interfere and are lost from the coherent beam. We can estimate the scattering angles for which the coherence is not broken. The angle should be such that the momentum transfer $p\vartheta$ falls inside the quantum-mechanical uncertainty in the momentum, Δp. Although a plane monochromatic wave ($\Delta p = 0$) hits the target, the uncertainty inside the scattering volume is other than zero. The spatial position of the particle is pinpointed by the scattering events, and it therefore cannot have a definite momentum. The mean distance between scattering events is of the order of Λ, so that $\Delta p \Lambda \sim 1$ (the uncertainty relation). Hence $\Delta p \sim \Lambda^{-1}$, i.e., $p\vartheta \sim \Lambda^{-1}$ or $\vartheta \sim \lambda/\Lambda$. If $\lambda \ll \Lambda$, interference effects can be ignored virtually in the entire range of angles and we may use the transfer equation. The applicability conditions of the transfer equation were studied in detail in /26, 27/.

IV. Although the transfer equation was originally derived about 50 years ago, the analytical solution was obtained in very few cases only. The classical problem of the theory of radiation transfer is the problem of a point source in an infinite medium. If a finite medium is to be considered (even in the case of scattering without energy losses), substantial mathematical difficulties arise and no analytical solution can be found. Although

the application of numerical techniques is very helpful, they obscure the qualitative picture of the phenomenon. We will therefore proceed with a qualitative treatment of multiple scattering of a particle (or a quantum) in a medium. For simplicity, we start with the case of scattering which does not involve substantial energy losses ($\gamma \ll 1$).

First let us introduce the physical parameters describing multiple scattering. Let $\sigma_s = \int d\vec{n}\,\sigma(\vec{n}\vec{n}_0)$ be the total scattering cross section of a particle in a single collision, σ_0 the total collision cross section, including true absorption, $\varepsilon = \sigma_s \sigma_0^{-1}$ a parameter characterizing the scattering probability in a single collision, $1-\varepsilon$ a quantity characterizing the probability of true absorption in a single interaction event. For a medium without absorption, ε is equal to unity. In general, ε is a function of energy, radically influencing the energy and the position distribution of the particles in the medium.

Let us now introduce a parameter describing the angular distribution of particles in the medium. This angular scattering function is defined as $\varkappa(\vec{n}_1\vec{n}_0) = \sigma(\vec{n}_1\vec{n}_0)\sigma_0^{-1}$. If the scattering cross section is isotropic, the angular scattering function is a constant number, equal to $(4\pi)^{-1}$. A particle may move from one point in the medium to another either by direct flight, without scattering, or as a result of multiple collisions ("diffusion").

The radiation density at a point 2 is expressed by the equality $n(x) = (\varepsilon/4\pi)\int I(\vec{n}_1\vec{n}_0; x)\,d\vec{n}_1$ which can be developed to the form

$$n(x) = e^{-x} + C(\varepsilon)\exp(-\beta x). \tag{6}$$

The distance x is measured in units of the total range of the particle in the medium. $C(\varepsilon)$ is a constant which depends on ε. $\beta = \beta(\varepsilon)$ is the reciprocal of diffusion. For simplicity, the radiation density at point 1 is taken equal to unity (again an infinite medium is considered). β is a highly important physical quantity in the theory of radiation transfer: it describes the process of multiple scattering. Whereas the total range of the particle in the medium, Λ, gives the mean distance covered by the particle to its first collision, irrespective of whether this is scattering or true absorption of the particle, the diffusion length determines the mean distance traversed by the particle to the first true absorption event. The total range thus corresponds to the loss of the particle from the beam following a collision event (scattering or true absorption), whereas the diffusion length specifies the mean distance that the particle covers before it is annihilated by true absorption. It is clear from physical considerations that the diffusion length depends on the probability of true absorption of a particle. If the true absorption is low, $1-\varepsilon \to 0$, the diffusion length increases indefinitely, $\beta \to 0$. If the elastic scattering cross section is small and all the processes in the medium are determined by true absorption, $\varepsilon \ll 1$, the diffusion length is equal to the total range of the particle in the medium, since in this case true absorption provides the only mechanism for knocking particles out of the beam. Calculation of the reciprocal diffusion length for the case of low true absorption, $1-\varepsilon \ll 1$, gives

$$\beta = \left[\frac{3(1-\varepsilon)}{\varepsilon}\left(1 - \frac{\varepsilon}{3}\varkappa_1\right)\right]^{\frac{1}{2}}, \tag{7}$$

where $\varkappa_1$ is the coefficient in the expansion of the angular scattering function in Legendre polynomials $\mathcal{P}_\ell(\vec{n}_1 \vec{n}_0)$ with $\ell = 1$:

$$\varkappa(\vec{n}_1 \vec{n}_0) = \frac{1}{4\pi} \sum_\ell \varkappa_\ell \mathcal{P}_\ell(\vec{n}_1 \vec{n}_0). \tag{8}$$

We thus have the following expression for the diffusion length squared Λ_d^2:

$$\Lambda_d^2 = \frac{1}{3(1-\varepsilon)} \Lambda \Lambda_T , \tag{9}$$

where Λ_T is the transport length, defined as the mean range of the particle for large-angle scattering ($\vartheta_1 > 0$):

$$\Lambda_T = \varepsilon \Lambda \left[\int d\vec{n}_1 (1 - \vec{n}_1 \vec{n}_0) \varkappa(\vec{n}_1 \vec{n}_0) \right]^{-1}. \tag{10}$$

The diffusion length is thus directly proportional to the square root of the product of the mean free path and the transport length. Given the diffusion length, we can assess the contribution from pure scattering and true absorption to multiple scattering without solving the transfer equation. Consider a plane target of thickness x_0. Then if $x_0 \Lambda_g^{-1} \equiv \beta (x_0/\Lambda) \gg 1$, the particles are lost from the beam mainly on account of true absorption. If $x_0 \Lambda_d^{-1} \ll 1$, pure scattering is the main factor in multiple scattering events.

Let us now consider the variation of radiation density (see (6)) at large distances from the radiation source ($x \to \infty$) if $1 - \varepsilon \ll 1$, i.e., when the true absorption in a single collision is unlikely. It is readily seen that for $x \to \infty$ and $1 - \varepsilon \ll 1$,

$$n(x) \to C(\varepsilon) \exp(-\beta x),$$

i.e., in an infinite medium particles diffuse over large distances from the source. Regarding the angular distribution of scattered particles, simple physical considerations show that diffusion leads to definite isotropization of the angular distribution irrespective of the particular angular scattering function of each individual force center. Deep inside the medium, the scattering intensity $I(\vec{n}_1 \vec{n}_0; x)$ has the form

$$I(\vec{n}_1 \vec{n}_0; x) = I_0(x) + I_1(x) \vec{n}_1 \vec{n}_0, \tag{11}$$

where $I_1(x) \ll I_0(x)$.

If the medium is characterized by pure scattering, i.e., $1 - \varepsilon \ll 1$, and the optical thickness is high $x_0 \Lambda^{-1} \gg 1$, the angular distribution of the transmitted radiation is nearly isotropic; it is adequately described by the formula $1 + {}^3/_2 \cos \vartheta_1$. The approximate expression $1 + 1.5 \cos \vartheta_1$ describes with fair accuracy the angular distribution of the outgoing radiation at angles between 60° and 90°. The largest error (~14%) is observed at angles close to 0°. The angular distribution function $1 + {}^3/_2 \cos \vartheta_1$ has a simple physical meaning. Calculation of the particle flux reaching the target surface $x = x_0$ in case of this angular distribution gives zero: $\int_0^1 d\cos\vartheta_1 \left(1 - \frac{3}{2}\cos\vartheta_1\right) \cos\vartheta_1 = 0$. This result is often used as a boundary condition in the calculation of physical processes in nuclear reactors (the so-called Marshak boundary condition).

In a high-absorption medium ($\varepsilon \ll 1$), the intensity of scattered radiation at angles $0 \leq \vartheta_1 \leq \pi/2$ is determined by the direct transmitted beam, decreasing exponentially with the diameter of the scattering system: $\exp(-x_0 \Lambda^{-1})$. This result corresponds to the case of low diffusion, when scattering is entirely determined by "fly-through" particles. As the absorption decreases, the contribution from diffusion becomes more significant, and the intensity of scattered radiation starts decreasing more slowly with the increase in system diameter: $\exp(-x_0 \Lambda_d^{-1})$, where $\Lambda_d > \Lambda$. Finally, in a pure scattering medium ($1 - \varepsilon \ll 1$) without absorption, diffusion makes the scattered intensity inversely proportional to the thickness of the scattering volume, provided it is greater than the mean free path of the particle in the medium to start with. The intensity of reflected radiation in this case is equal to the intensity of reflection from a semi-infinite space plus terms of the order Λx_0^{-1}.

V. Let us consider the multiple scattering of particles in a plane material layer with allowance for the slowing down caused by collisions. We will concentrate on particles which lose a considerable part of their energy in these collisions, so that the energy E_1 is much less than the initial energy E_0. The physical parameter characterizing the slowing-down properties of the medium is the so-called moderation length $\tau\Lambda$, where $\tau^2 = (6\gamma)^{-1} \ln (E_0/E_1)$. This is the analog of the diffusion length in monoenergetic transport of particles. We recall that $\gamma = m M^{-1}$ is the ratio of the incident particle mass to the mass of a scattering atom. In what follows, we invariably take the incident particle to be much less massive than the target atom.

Note that the angular distribution of particles which have lost a substantial proportion of their initial energy is independent of energy in a fairly wide range. This is so because the angular distribution is mainly shaped at distances of the order of the total free path from the layer boundary, whereas the slowing down mainly occurs in the process of diffusion, which only "smoothes out" the angular distribution. The angular distribution of the outgoing radiation is adequately described by the function $1 + 1.5 \cos \vartheta$; the radiation emerging through $x = 0$ and $x = x_0$ has the same angular distribution. This is so because the two interfaces are virtually equivalent with regard to the highly moderated particles which form deep inside the scattering medium and diffuse in all directions. The anisotropy in the angular distribution, which develops near the layer boundaries, is therefore virtually equal for the radiation emerging through the interfaces $x = 0$ and $x = x_0$.

The number of particles of a given energy emerging through $x = x_0$ depends on the thickness of the layer, reaching a maximum for $x_0 \simeq \Lambda\tau$. The energy spectrum of these particles is described by

$$\frac{dn(E_1, x_0)}{dE_1} \sim \left(\frac{x_0}{\Lambda}\right)^2 \frac{1}{E_1 \tau^5} \exp\left[-\frac{x_0^2}{4\Lambda^2\tau^2} - \frac{1-\varepsilon}{2\gamma\varepsilon} \ln \frac{E_0}{E_1}\right]. \qquad (12)$$

For layer thicknesses less than $\tau\Lambda$, the particles are not slowed down to the energy E_1, and in thicker layers they are slowed down to lower energies. For $\Lambda\tau \ll x_0$ we have particles which, for a given energy loss, propagate very far from the boundary of the region where the radiation sources are contained. It follows from (2) that the smaller the scattering angle, the

smaller are the energy losses in collision. Therefore, for $x_0 \gg \tau\Lambda$, the particles emerging from the plane layer have mainly lost a small fraction of their initial energy and their angular distribution is prominently stretched in the forward direction.

The intensity of the radiation emerging through the interface $x = 0$ significantly depends on the relationship between the characteristic dimension L of the region containing the radiation sources and the moderation length of the particles in the medium. Thus, if the moderation length $\tau\Lambda$ is much greater than L, the energy spectrum of the radiation is given by

$$\frac{dn(E_1,0)}{dE_1} \sim \frac{1}{E_1\tau^3} \exp\left(-\frac{1-\varepsilon}{2\gamma\varepsilon} \ln\frac{E_0}{E_1}\right). \qquad (13)$$

If the moderation length is much smaller than the characteristic dimension of the source region, the energy spectrum of the radiation emerging through the $x = 0$ interface is given by

$$\frac{dn(E_1,0)}{dE_1} \sim \frac{1}{E_1\tau} \exp\left(-\frac{1-\varepsilon}{2\gamma\varepsilon} \ln\frac{E_0}{E_1}\right). \qquad (14)$$

Note that the dependence of the number of scattered particles on the reciprocal value of the mean atomic weight of the entire medium is also determined by the relationship between the moderation length $\tau\Lambda$ and the size of the source region (the generation length) L. Specifically, $n(E_1, x=0) \sim \sqrt{\gamma}$ if $L \ll \tau\Lambda$ and $n(E_1, x=0) \sim \gamma^{-1/2}$ if $L \gg \Lambda\tau$. A detailed theory of the slowing down of particles in matter is presented in /3, 28/.

VI. Let us now consider the determination of the energy spectrum and the neutron flux produced by the interaction of cosmic radiation with the surface of celestial bodies. The energy spectrum of the galactic cosmic protons is peaked at 1 BeV. The interaction of high-energy particles (protons, neutrons, pions) with the nuclei of elements is currently the subject of theoretical and experimental studies /29, 30/, and very few details are available at present. Experimental investigations show that the interaction of a high-energy particle with a nucleus proceeds in two stages. During the first stage, the incident particle creates a cascade inside the nucleus. The cascade releases several nucleons from the nucleus with energies substantially higher than 10 MeV and with an anisotropic angular distribution. At the same reaction stage neutral and charged pions are created, which interact with the nuclei and trigger other nuclear reactions releasing fast nucleons. At the second stage of the reaction, the nucleus remaining after the ejection of the fast nucleons "relieves" itself of the excitation by a characteristic evaporation mechanism. In the course of evaporation, the nucleus emits neutrons with an isotropic angular distribution and an energy spectrum $E_0^{\ell-1}\theta^{-\ell}\exp(-E_0\theta^{-1})$ /30/, where E_0 is the energy of the evaporating neutrons, $\theta \sim 1$ MeV (evaporation temperature), $\ell = 16/11$. The cascade nucleons created during the first stage of the nuclear reaction produce in their turn evaporating neutrons through (n,n') and (p,n') reactions. The source function in our problem thus describes isotropically distributed evaporating neutrons. In what follows, we will require some detailed information regarding this source. We will be dealing with neutrons whose energy E_1 is substantially less than the initial

energy E_0. These neutrons do not originate in the source: they are produced as a result of multiple scattering and slowing down in the medium.

The following three problems associated with neutron radiation attract considerable attention at this stage. The first problem deals with the determination of neutron radiation generated in terrestrial rocks by the action of secondary nucleons which are produced in the atmosphere and then reach the Earth /31/. This problem is of considerable significance for the purposes of neutron logging on the Earth, since the natural neutron background has to be determined with high accuracy. The second problem is concerned with the determination of the spectrum of epithermal neutrons produced by the cosmic rays in the Earth's atmosphere. The third problem aims at a determination of the composition of lunar rocks from the neutron radiation emitted from the surface of the Moon. This problem was studied in some detail by the present authors in collaboration with A.I. Tsygan /32/, and also in /20/. As an illustration, let us estimate the flux of neutrons with energies from 1 eV to several MeV leaving the surface of the Moon. Using the equations of the previous section, we write

$$n(E_1, E_2) = 2j\kappa L^{-1}(\tau_1 - \tau_2), \tag{15}$$

where j is the flux of incident cosmic protons, κ is the number of 10 MeV neutrons generated by a single proton and then slowed down in the medium (the source neutrons), L is the generation length of these neutrons (the characteristic dimension of the source region). The most difficult point in flux determination is the calculation of κ and L, which essentially depend on the particular interaction of the proton with the nucleus. We will not consider this problem, although it is definitely solvable /30/. Using (15) and the SURVEYOR-5 data on the composition of the lunar surface /33/, we can estimate the neutron flux emerging from the surface of the Moon. In accordance with the SURVEYOR-5 data, the predominant elements in the composition of the lunar surface at the mooning site were oxygen (58±5)% and silicon (18.5±3)%. We will therefore carry out the numerical calculations for the compound SiO_2, which in all probability is a component part of the lunar rocks. Taking the peak energy in the spectrum of evaporating neutrons as the initial neutron energy ($E_0 \sim 4$ MeV) and using $E_1 \sim 4$ eV for the final energy, we find $n = 0.62\ j\kappa = 10\ \text{cm}^{-2}\text{sec}^{-1}$. Let us evaluate the effect of hydrogen impurity on the outgoing neutron flux. The mean reciprocal mass number of a mixture of elements is given by

$$\bar{\gamma} = \frac{1}{2} C_H + \sum_i \gamma_i C_i, \quad C_i = \frac{N_{0i}\sigma_{0i}}{\sum_i N_{0i}\sigma_{0i}}, \tag{16}$$

where N_{0H} is the hydrogen concentration, N_{0i} is the concentration of the i-th element.

Consider a mixture of Si with 0.6% H. Then from (16) $\bar{\gamma} = 1/14$, whereas for pure Si, $\gamma = 1/28$. We thus see that even a small hydrogen impurity substantially influences the neutron flux, reducing it approximately by a factor of 1.5–2. This reduction of neutron flux at energies between 4 eV and 4 MeV occurs because of the high elastic scattering cross section of hydrogen for neutrons. As a result, hydrogen acts as a highly effective neutron moderator, slowing down the neutrons to energies below 4 eV.

Note that a mixture containing 99.4% Si and 0.6% H has the same slowing down properties as pure nitrogen.

Heavy element impurities increase the neutron flux. This flux increase is associated with the fact that the mean number of evaporating neutrons per heavy nucleus is approximately one order of magnitude higher than for the light nuclei. For example, a 10% lead impurity in SiO_2 roughly doubles the neutron flux.

VII. A complete solution of the problem of interaction of cosmic protons with the Earth's atmosphere requires knowledge of the distribution function of protons and neutron hydrogen atoms in the atmosphere. Strictly speaking, we have to solve a set of two couplet rate equations for the distribution function, allowing for the possible transition of the proton into the neutron hydrogen state as a result of charge exchange and for a reverse transition as a result of ionization. Detailed analysis of the physical features of the process, however, will substantially simplify our solution.

The main components of the upper atmosphere at altitudes of 150 – 500 km are atomic oxygen, molecular oxygen, and molecular nitrogen. Now, the charge exchange cross sections of protons in these gases with the production of an excited hydrogen atom is much lower than the cross section for charge exchange producing a ground-state hydrogen atom. It therefore seems that neutral hydrogen is produced in the ground state and is then excited by inelastic collisions with the atmospheric gases. We can also ignore the difference in the translational energy of the excited hydrogen atoms produced by various inelastic collisions and radioactive transitions. This approximation is quite justified since the energy of protons and hydrogen atoms in the Balmer emission region is two orders of magnitude higher than the excitation energy. Finally, the most important factor is that the mean free path of a neutral hydrogen atom in the atmosphere is much longer than the mean free path of a proton. This result clearly emerges from the table, borrowed from /34/. Let us compare the energy losses over the mean free path of a neutral hydrogen atom and a proton, respectively. The energy lost by a neutral hydrogen atom over its mean free path is obtained using (31) from the equality $2\tau = 1$:

$$\tau = \sqrt{\frac{1}{6\gamma} \ln \frac{E_0}{E_1}} = \sqrt{\frac{1}{6\gamma}} \sqrt{\ln \left(1 + \frac{\Delta E}{E_1}\right)}.$$

Mean free path of a proton and a neutral hydrogen atom in the Earth's atmosphere, km

Height, km	$H^+ \rightarrow H$	$H \rightarrow H^+$
700	9900	
600	4300	
500	490	10,000
400	98	2000
300	19	300
200	4	30
180	2	
150	1	5
120	0.2	

The condition $4\tau^2 = 1$ gives $\Delta E/E_1 \approx {}^3/_2\,\gamma \sim 1/9$ for the atmosphere. Thus, a neutral hydrogen atom loses about $^1/_9$ of its initial energy over the free mean path. The energy losses of protons can be found from the results of /35/: a proton with energies between 1 and 30 keV loses to ionization events about 100 eV in each collision. We see that the main energy losses are associated with the neutral hydrogen atoms, so that the angular and the energy distribution of protons in the medium is determined by the scattering and the slowing-down of the neutral hydrogen atoms produced in charge exchange reactions.

The angular and the energy distribution of protons and neutral hydrogen atoms thus can be determined directly from equations (12) and (13). Using these equations, we can also determine the intensity of Balmer emission and the energy spectrum of the original proton beam. In accordance with the preceding theory, the angular distribution of the neutral hydrogen atoms is described by $1 + \alpha \cos \vartheta_1$, $\alpha \leq {}^3/_2$. Some authors /23, 24, 36/ determined the angular distribution of protons from the angular distribution of the Balmer emission. The experimental data lead to an angular distribution of the form $1 + \alpha \cos \vartheta_1$, $0 \leq \alpha \leq 2$, but the data are insufficient for an exact determination of the coefficient α. It is hoped that satellite and rocket measurements in the very near future will provide direct data on the distribution function of penetrating protons, which can be used as a basis of comparison with the theory.

Bibliography

1. Chandrasekhar, S. Radiative Transfer.— New York-Denver. 1960.
2. Sobolev, V.V. Perenos luchistoi energii v atmosferakh zvezd i planet (Radiant Energy Transfer in Stellar and Planetary Atmospheres).— Moskva, Gostekhizdat. 1956.
3. Davison, B. Neutron Transport Theory.— Clarendon Press, Oxford. 1957.
4. Weinberg, A.M. and E.P. Wigner. The Physical Theory of Nuclear Chain Reactors.— Chicago, Univ. of Chicago Press. 1958.
5. Galanin, A.D. Teoriya yadernykh reaktorov na teplovykh neitronakh (Theory of Thermal-Neutron Nuclear Reactors).— Moskva, Atomizdat. 1959.
6. Scott, W.T.— Rev. of Mod. Phys., 35:231. 1963.
7. Dolginov, A.Z. and I.N. Toptygin.— ZhETF, 51-1771. 1966.
8. Dolginov, A.Z. and I.N. Toptygin.— Geomagnetizm i Aeronomiya, 7:967. 1967.
9. Parker, E.N.— Phys. Rev., 110:1445. 1958.
10. Dorman, L.I. and L.I. Miroshnichenko. Solnechnye Kosmicheskie Luchi (Solar Cosmic Rays).— Moskva, Izd. "Nauka." 1968.
11. Kaplan, S.A. and V.N. Tsytovich.— UFN, 97:77. 1969.
12. Tsytovich, V.N. and A.S. Chikhachev.— Radiofizika, 12:26. 1969.
13. Sagan, C. The Origin and Evolution of Atmospheres and Oceans. New York. 1964.

14. Sagan, C. and I.B. Pollack.— J. Geophys. Res., 72:469. 1967.
15. Gnedin, Yu.N. and A.Z. Dolginov.— Astronomicheskii Zhurnal, 18:181. 1966.
16. Konstantinov, B.P., M.M. Bredov, S.V. Viktorov, G.V. Kir'yan, G.E. Kocharov, and B.O. Naidenov.— DAN SSSR, 181:55. 1968.
17. Berkner, L.V. and H. Odishaw (Editors). — Science in Space. New York, McGraw-Hill. 1961.
18. Hayakawa, S.— Space Res., 3. 1962.
19. Kranev, H.W., G.L. Schroedev, G. Davidson, and I.W. Carpenter.— Nature, 152:3726. 1966.
20. Lingenfelter, R.E., E.H. Canfield, and W.N. Hess.— J. Geophys. Res., 66:2665. 1961.
21. Mandel'shtam, S.L., I.P. Tindo, G.S. Cheremukhin, L.S. Sorokin, and A.B. Dmitriev.— Kosmicheskie Issledovaniya, 6:119. 1968.
22. Vinogradov, A.P., Yu.A. Surkov, G.M. Chernov, F.F. Kirnozov, and G.B. Nazarkina.—Kosmicheskie Issledovaniya, 5(6):874. 1967.
23. Gal'perin, Yu.I. In: "Polyarnye Siyaniya i Svechenie Nochnogo Neba." No. 1:70. Moskva, Izdatel'stvo AN SSSR. 1963.
24. Gal'perin, Yu.I., I.A. Polyektov, and I.I. Sobel'man.— Geomagnetizm i Aeronomiya, 6:633. 1966.
25. Kurt, V.G. and T.A. Germogenova.— Astronomicheskii Zhurnal, 44:352. 1967.
26. Gnedin, Yu.N. and A.Z. Dolginov.— ZhETF, 45:1136. 1963.
27. Gnedin, Yu.N. and A.Z. Dolginov.— Astronomicheskii Zhurnal, 18:800. 1966.
28. Tsygan, A.I. Thesis.— Leningrad, FTI AN. 1969.
29. Metropolis, N., R. Bivins, and M. Storm.— Phys. Rev., 110: 185 and 204. 1958.
30. Koshin, V.A. and E.S. Matusevich.— Atomic Energy Rev., 6. 1968.
31. Gorshkov, G.V. and O.S. Tsvetkov.— Atomnaya Energiya, 26:27. 1969.
32. Gnedin, Yu.N., A.Z. Dolginov, and A.I. Tsygan.— Kosmicheskie Issledovaniya (in press).
33. Turkevich, A.L., E.J. Franzgrote, and I.H. Patterson.— Science, 158:635. 1967.
34. Davidson, G.T.— J. Geophys. Res., 70:1061. 1965.
35. Dalgarno, A. and G. Griffing.— Proc. Roy. Soc., A248:415, London. 1958.
36. Vaisberg, O.L.— In: "Polyarnye Siyaniya i Svechenie Nochnogo Neba," 9:24, Moskva, Izdatel'stvo AN SSSR. 1962.

SPACE-PHYSICAL INVESTIGATIONS IN THE LABORATORY

I. M. Podgornyi

Shock waves constitute one of the most interesting phenomena which take place in the interplanetary plasma and in the solar corona. Since the solar wind is a kind of supersonic plasma stream, its interaction with the objects in the interplanetary space and the interaction between plasma clouds moving with different velocities will inevitably generate shock waves. The main distinction between these plasma shock waves and the shock waves in the Earth's atmosphere involves the particular mechanism of energy dissipation of the plasma streaming motion. When a shock wave is formed in a dense gas, e.g., in front of a supersonic aircraft, the energy is dissipated through molecular collisions between the gas particles. The width of the shock in this case is therefore of the order of $\lambda = 1/n\sigma$, where σ is the effective cross section for the interaction of molecules and n is the concentration of molecules.

In the interplanetary space, the particle concentration is approximately 10^{-19} of the concentration in the ground air, and the characteristic free paths of electrons and ions are substantially greater than the measured shock width. A similar situation is observed under laboratory conditions, when the shock wave in a thin plasma is produced by a so-called magnetic piston.

Let us consider in some detail one particular case, namely the case of a shock parallel to the magnetic field lines frozen into the plasma. The formal hydrodynamic treatment of the plasma behavior in a magnetic field is applicable to low-density plasma when the free path is substantially greater than the Larmor radius. If the wave amplitude in a low-pressure plasma is sufficiently small, the state behind the shock is independent of the particular dissipation mechanism. The pressure gradient in this case is mainly determined by the magnetic pressure and the starting equations are considerably simplified (the equation of energy flux conservation may be omitted). Sagdeev /1/ has shown that this treatment in the case of small amplitudes leads to a distinct oscillatory structure of the shock with an oscillation scale c/ω_0, where $\omega_0 = \sqrt{\frac{4\pi ne^2}{m}}$ is the Langmuir frequency, n, e, m are the electron concentration, the electron charge, and the electron mass, c is the velocity of light. Among the various damping mechanisms which are not related to Coulomb collisions, we should first mention reflection from the magnetic field maxima of particles with velocities close to the shock wave velocity. Dissipation may occur due to particle scattering by microfluctuations which are associated with the onset of instabilities.

A different behavior is observed for an oblique wave, i.e., a wave whose front forms a finite angle with the direction of the magnetic field lines. If $\theta > \sqrt{\frac{m}{M}}$ (M is the ion mass), the oscillatory structure of the shock is substantially different. The oscillations overtake the shock and their characteristic scale is $\frac{c}{\Omega_0}\theta$, where $\Omega_0 = \sqrt{\frac{4\pi e^2 n}{m}}$ is the ion Langmuir frequency.

The oscillatory structure is observed for Mach numbers smaller than some critical value. The critical value of the Mach number for a straight wave is about 3. For Mach numbers greater than M_{cr}, the shock topples over, just like the crest of a sea wave in shallow water. This "surf" gives rise to countercurrents. When the velocity of countercurrents exceeds the velocity of ionic sound $\sqrt{T_e/M}$, ionic sound instability develops. The scattering of particles by microfluctuations increases the effective scattering length, i.e., it leads to effective dissipation of streaming energy. The shock width in this case is $\sim c/\Omega_0$.

A typical experimental setup for the study of a collision-free shock wave propagating across the field is shown in Figure 1 /2—6/. The plasma is produced by a preliminary discharge in the solenoid magnetic field. A one-loop coil with low-inductance feeders is inserted into the solenoid. The discharge of a condenser bank produces a sharp increase of the magnetic field, so that a magnetic wall is created between the coil and the plasma, compressing the plasma in the axial direction with a super-Alfven velocity. The magnetic wall (piston) generates a shock wave, and if the coil is sufficiently large the shock may develop to steady-state conditions.

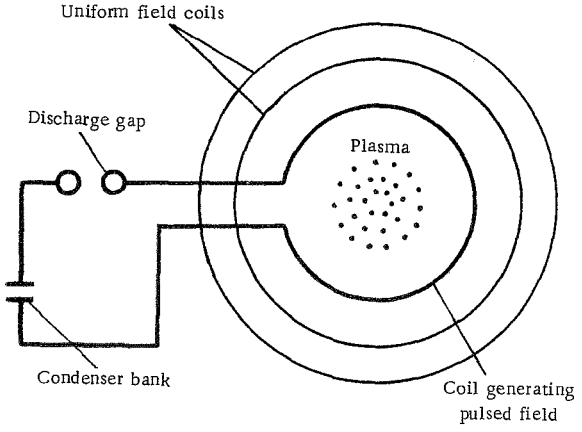

FIGURE 1. Experimental setup for studying a collisionless shock wave.

In accordance with the theoretical predictions, a distinct oscillatory structure with a scale of $\sim c/\omega_0$ is observed for $M < M_{cr}$. For supercritical Mach numbers, no oscillations are observed and the shock width

is of the order of c/Ω_0. These experiments demonstrate the generation of collision-free shock waves, but the results are not entirely suitable for comparison with measurements in outer space. It is clear from the above examples that, even for the same initial conditions, the shock wave is substantially different for Mach numbers below and above the critical value. These two extreme cases, however, by no means cover the entire range of various shock waves generated in a collision-free plasma. Therefore, simulation of the interaction of the solar wind with various objects in the interplanetary space is impossible without correct reproduction of the space conditions in the laboratory.

The experimental findings provided by satellites and rockets are sufficient for an approximate classification of the interaction effects of the solar wind with three objects — the Earth, the Moon, and Venus. Analysis of these effects will enable us to come up with a proper formulation of the simulation conditions for some phenomena associated with the solar-wind interaction. Each of the three cases above has its own characteristic features. Shock waves were discovered around Earth and Venus, but the generation mechanism is essentially different in these two cases. The interaction of the solar wind with the Moon does not produce a shock wave. Let us consider the simulation problem for each of these cases separately.

EARTH

The space around the Earth is the best studied part of the interplanetary space. There is a wealth of material for detailed comparison with various theoretical assumptions. On the other hand, only partial information can be obtained by direct measurements in outer space, and simulation experiments are essential for filling in the blanks.

The flow of the solar wind past the geomagnetic field creates a magnetosphere free from the solar wind plasma, and the interface acts as a magnetic piston. To create a magnetosphere in laboratory experiments, the skin-layer thickness should be less than the magnetosphere dimension, i.e., we should have

$$Re_m = \frac{4\pi\sigma L \bar{v}}{c^2} \gg 1, \qquad (1)$$

where Re_m is the magnetic Reynolds numbers, σ is the plasma conductivity, L is the characteristic dimension of the magnetosphere, $\bar{v}$ is the streaming velocity. Calculating the conductivity from Coulomb collisions

$$\sigma = 12\, T_e^{3/2}\,(\mathrm{eV})\,\mathrm{ohm}^{-1}\,\mathrm{cm}^{-1}, \qquad (2)$$

we obtain for the interaction of the solar wind with the geomagnetic field $Re_m \sim 10^{12}$. When choosing the laboratory conditions, we should remember that the collective processes in plasma increase the effective frequency of collisions. As a result, the plasma conductivity calculated from equation (2) may differ in its order of magnitude from the true plasma conductivity. Hence, the electron temperature of the plasma and the velocity should be chosen so that the condition $Re_m \gg 1$ is satisfied with an adequate margin

(of several orders of magnitude). In the experiments carried out at the Institute of Space Research, Re_m was taken of the order of 10^4 for $\bar{v} = 3 \cdot 10^7$ cm/sec and $T_e \sim 15$ eV.

We know from the theory of collisionless shock waves that the type of the shock wave, and in particular, the shock width and structure, are determined by the following nondimensional parameters:

1. The Mach number $M = \bar{v} / \sqrt{\frac{T_e}{M}}$.

2. The Mach number relative to the Alfven velocity $M_A = \frac{\bar{v}}{H/4\pi\rho}$, where $\rho = Mn$ is the plasma density.

3. The ratio of the gas-kinetic plasma pressure to the magnetic pressure $\beta = \frac{nk(T_e + T_j)}{H^2/8\pi}$.

4. The ratio of the electron Larmor frequency $\omega_H = \frac{eH}{mc}$ to the Langmuir frequency $\omega_0 = \sqrt{\frac{4\pi ne^2}{m}}$. A nondimensional parameter $\alpha = (\omega_H/\omega_0)^2$ is generally introduced.

5. The ratio of the electron temperature to the ion temperature.

In addition to the above conditions, simulation of a collisionless shock wave also requires that the free path length in an undisturbed stream be large compared to the characteristic scale of the experiment (dipole size, shock width).

If the phenomenon is a continuous function of the nondimensional parameters, there is no need to maintain exactly constant values of these parameters, which anyhow greatly differ from unity. It is only essential that the nondimensional parameters for the laboratory plasma be much greater (or much smaller, as the case may be) than unity, as in the interplanetary space, but it is not necessary to strive to attain the correct orders of magnitude. This principle was actually adopted in the model experiments carried out at the Institute of Space Research /7–9/. The table below lists the experimental conditions required for the simulation of the magnetosphere and the collisionless shock wave generated by the interaction of the solar wind with the geomagnetic field. Solar wind conditions are given for comparison purposes.

	Electron temperature, eV	Ion temperature, eV	Concentration, cm^{-3}	Velocity, cm/sec	Magnetic field in plasma, Oe
Space	20—50	10	$5 \cdot 10$	$3—5 \cdot 10^7$	10^{-4}
Experiment	15	5	10^{13}	$3 \cdot 10^7$	40

MOON

The Moon has no magnetic field, so that no shock wave can form in its interaction with the solar wind. However, as long as there are no detailed measurements of the magnetic field around the Moon, we cannot rule out the possibility of formation of a shock wave due to condensation of the magnetic field lines frozen into the plasma as the plasma stream flows

around a high-conductivity body. For low-conductivity bodies or for bodies with a nonconducting shell, there are two configurations of the induced magnetic field which may produce a shock wave.

1. The average conductivity of the planet is high and the skin-layer depth $\delta = \frac{c^2}{4\pi\sigma\bar{v}}$ is small compared to the planetary radius. The field lines do not penetrate into the interior, and an "induced" magnetosphere is formed at the surface. In other words, the conditions favor the formation of a shock wave in a supersonic plasma stream. The condition for shock formation in this case has the form

$$\frac{8\pi\sigma_{Moon} R_{Moon} \bar{v}}{c^2} >> 1.$$

Insertion of numerical values gives $\sigma_{Moon} >> 10^4$ CGSE, or 10^{-8} ohm^{-1} cm^{-1}, which corresponds to the conductivity of slate. The conductivity of paper, Na glass, and porcelain is four orders of magnitude lower. The average conductivity of the Moon is so far unknown, not even to orders of magnitude and no simulation experiments could therefore be carried out.

2. The other hypothesis of shock wave formation near the Moon is associated with the assumption of a conducting core at the center of the planet (Figure 2).

With this geometry, the incident plasma is absorbed by the lunar surface, and the magnetic field lines of the solar wind freely penetrate into the low-conductivity region until they are stopped by the conducting core. The field lines bypass the core, forming an induced magnetosphere. If the low-conductivity layer is sufficiently thick, this induced magnetosphere does not emerge on the day side of the planet. In this case, a shock wave around the Moon could form only far from the Moon – Sun center line.

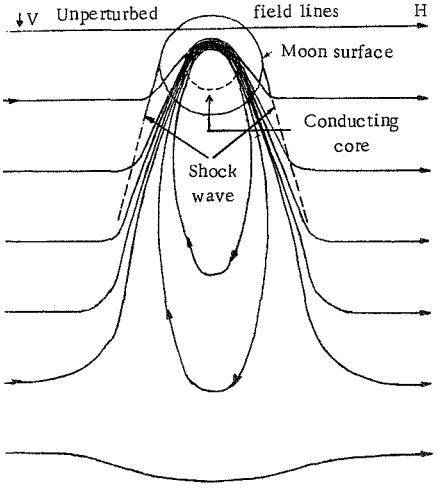

FIGURE 2. Formation of a shock wave around the Moon.

Until recently, the question of the formation of a shock wave near the Moon remained within the framework of pure hypothesis, and only the measurements of the magnetic field geometry by the three Explorers (33, 34, and 35) provided adequate factual data for analysis. One of the Explorers remained in a lunar orbit and carried out measurements on the night side of the Moon /10/. It was established that no shock wave formed around the Moon and no field distortion or concentration was observed on the day side, i.e., the Moon absorbs the incident plasma and the field lines freely pierce the bulk of the planet. A shadow trail with a markedly reduced plasma

concentration is observed on the night side of the Moon. The magnetic field in the trail is somewhat higher than in the nearby solar wind.

The Explorer measurements traced the propagation of the spatial magnetic field fluctuations through the bulk of the Moon. Fluctuations of about 5 sec duration were found to propagate through the Moon without noticeable distortion, which points to an average conductivity of 10^{-8} – 10^{-7} ohm^{-1} cm^{-1}.

VENUS

The measurements carried out from VENUS-4 /11/ show that at a distance of about 19,000 km from the surface of Venus the plasma concentration and the magnetic field strength increase markedly. This effect can be interpreted as formation of a shock wave. The existence of a shock wave around Venus cannot be attributed to the same physical factors that we use to explain the shock wave around the Earth. The main difference is that Venus has no magnetic field which could provide the magnetic piston. Under these conditions, a shock wave can form only around high-conductivity objects, when the time for the plasma to traverse one diameter is less than the spin time. We should again distinguish between two possible types of distortion of the frozen magnetic field in the solar plasma.

1. Venus has a high-conductivity core. The magnetic field lines encircling the planet and forming the induced magnetosphere will lie outside the bulk of the planet if the thickness of the low-conductivity envelope is less than 300 km /11/, i.e., $^1/_{10}$ of the Earth's mantle. Otherwise, the induced magnetosphere is retained inside the planet on the day side and a shock wave will form only far from the point of attack.

2. The upper atmospheric layers act as a conducting sphere. The requisite ionization is caused by the absorption of solar radiation. Particle traps recorded charged particle concentrations of about 10^3 near Venus, so that the second assumption seems justified.

Let us consider the conditions for the simulation of the solar-wind interaction with Venus. Our problem is to investigate the effects associated with the formation of a shock wave at the interface between the plasma envelope of the planet and the undisturbed stream of solar plasma. The absence of a magnetic field around Venus signifies that the interaction in fact takes place between a stream with a frozen magnetic field and a stream initially free from any fields. The allowed parameters of the artificial solar wind in simulation experiments were considered in connection with the shock wave around the Earth. We will now have to choose the conditions for the plasmoid simulating the Venusian ionosphere. The main conditions can be stated in the following form.

1. Plasmoid skin-layer thin compared to the shock width, i.e., $\frac{4\pi\sigma\bar{v}\delta}{c^2} \gg 1$.

Here δ is the shock width. Taking $\delta = 5$ cm, which corresponds to the experimental value, we get $\sigma \gg 5 \cdot 10^{11}$.

2. For a steady-state shock wave to form, the stream pressure $\rho\bar{v}^2$ should be equal to the plasmoid pressure, i.e., $\rho\bar{v}^2 \sim n_2 kT_2$. Inserting the ρ and $\bar{v}$ values of the artificial solar wind, we get $n_2 kT_2 = 4 \cdot 10^{15}$ eV/cm^3.

3. To avoid destruction of the fast ions in the transitional layer through charge exchange with the neutral gas and thus maintain the pressure balance at the interface, we should have $\lambda_{tr} >> \delta$. For the given hydrogen plasma velocity $\bar{v} = 3 \cdot 10^7$ cm/sec, this condition can be written in the form $n_0 \ll 10^{14}$ cm^{-3}.

A nonmagnetized hydrogen plasma with $n_2 = 2 \cdot 10^{14}$ cm^{-3} and electron temperature $T_2 = 20$ eV meets these requirements. The neutral gas under these conditions burns out in less than one microsecond.

A plasma with $T = 20$ eV and $n = 10^{14}$ cm^{-3} can be produced without difficulty in an external magnetic field, but it is very difficult to avoid frozen-in fields. These difficulties, however, are of a technical nature only, so that in principle the interaction of the solar wind with Venus can be simultated in the laboratory.

LABORATORY EXPERIMENT

The experiments carried out at the Institute of Space Research /7, 9/ studied the interaction of an artificial solar wind with the parameters listed in the table with a two-dimensional magnetic dipole simulating the Earth. The aim was to reproduce the main effects taking place near the Earth's magnetosphere. The field of the two-dimensional dipole was set up by two parallel conductors with current flowing in opposite directions. The distance between the conductors was 2 cm. This geometry permitted measurement of the plasma concentration directly, without introducing any distortions into the system. In actual measurements, the beam from a laser interferometer /13, 14/ was directed parallel to the conductors, i.e., it propagated along a line of constant plasma concentration (apart from edge effects). In a three-dimensional dipole, the conversion from the average concentrations along the beam to local concentrations involves very tedious calculations and does not give accurate results. The magnetic field distribution was measured with probes.

The results of the magnetic measurements show that the plasma stream displaces the dipole field on the "day" side from the region where the magnetic pressure $H^2/8\pi$ is less than the stream pressure $\rho \bar{v}^2$. Near the dipole the magnetic field intensity increases, forming a plasma-free space — a magnetosphere. The extent of the magnetosphere in these experiments was about 10 cm. Near the magnetosphere boundary, a collisionless shock wave separates. The magnetic field strength and the concentration increase by a factor of 3—4 at the shock. The shock is 5 cm wide, which corresponds to the ratio c/Ω_0, where c is the velocity of light and $\Omega_0 = \sqrt{\frac{4\pi e^2 n}{M}}$ is the ion plasma frequency. Measurements carried out from artificial Earth satellites also give the value of c/Ω_0 for the shock width near the Earth.

Among the various modes of streaming energy dissipation, we should primarily mention particle scattering by ionic-sound oscillations and instability of magnetohydrodynamic waves as a result of pressure anisotropy (Alfven and magnetic sound instability). Both these mechanisms are effective in the interplanetary plasma and in the laboratory for $T_e > T_i$

and $\beta \gtrsim 1$. Since the excitation of ionic-sound oscillations has been previously studied in magnetic piston experiments /3/, our experiments were mainly concerned with energy dissipation through Alfven instability /16/.

The Alfven instability develops when $nkT_{\parallel} > nkT_{\perp} + \frac{H^2}{4\pi}$. Its characteristic length is of the order of the ion Larmor radius and its frequency is Ω_0. Experiments carried out by the present author jointly with E.M. Dubinin and G.G. Managadze (these experiments included correlation measurements) showed that the magnetic field fluctuations at the shock are consistent with the assumption of Alfven instability.

In addition to simulation experiments with a collisionless shock wave, the night side of the magnetosphere was also studied. Laboratory experiments /7 — 9/ established the formation of a geomagnetic tail with a neutral layer, produced by the anomalous diffusion of plasma through the boundary of the magnetosphere and subsequent entrainment of the magnetic field by the plasma stream. The results of the laboratory experiment fit the measurements of aritificial Earth satellites.

All the results of laboratory measurements show that certain effects associated with the interaction of the solar wind with the geomagnetic field can be effectively simulated in the laboratory. The observation of these effects in the laboratory is naturally immeasurably simpler than in outer space. The advantages of simulation experiments are particularly obvious in cases of correlation measurements which have to be carried out simultaneously at different points in space.

Bibliography

1. Sagdeev, R.Z.— In: "Voprosy Teorii Plazmy," 4:20, Moskva, Atomizdat. 1963.
2. Zagorodnikov, S.P., G.E. Smolkin, and G.V. Sholin.— Conference on Ionized Gases. Belgrad. 1965.
3. Alikhanov, S.G.— MAGATE Conference on Thermonuclear Fusion. Novosibirsk. 1968.
4. Paul, J.W.M., G.C. Goldenbaum, A. Iivoshi, L.S. Holmes, and R.A. Hardcastle.— Nature, 216:363. 1967.
5. Khintts, E.— MAGATE Conference on Thermonuclear Fusion. Novosibirsk. 1968.
6. Robson, A.E. and Dzh. Sheffil'd.— MAGATE Conference on Thermonuclear Fusion. Novosibirsk. 1968.
7. Managadze, G.G. and I.M. Podgornyi.— DAN SSSR, 180:1333. 1968.
8. Podgornyi, I.M. and G.G. Managadze.— Vestnik AN SSSR, No.7:38. 1968.
9. Managadze, G.G. and I.M. Podgornyi.— Geomagnetizm i Aeronomiya, 8:612. 1968.
10. Ness, N.F.— Conference on the Physics of the Moon and Planets, Kiev. 1968.
11. Gringauz, K.I., V.V. Bezrukikh, L.S. Musanov, and T.K. Breus.— Kosmicheskie Issledovaniya, 6:411. 1968.

12. Dolginov, Sh.Sh., E.G. Eroshenko, and L.N. Zhuzgov.— Kosmicheskie Issledovaniya, 6:561. 1968.
13. Managadze, G.G., I.M. Podgornyi, and V.D. Rusanov.— Geomagnetizm i Aeronomiya, 8:545. 1968.
14. Managadze, G.G., I.M. Podgornyi, and V.D. Rusanov.— In: "Voprosy Teorii Plazmy," Part 2, Moskva, Atomizdat. 1963.
15. Kaufman, R.L.— J. Geophys. Res., 72:2323. 1967.
16. Kenel, C. and R.Z. Sagdeev.— J. Geophys. Res., 72:3303. 1967.
17. Ness, N.F.— J. Geophys. Res., 70:2989. 1965.

THE TRAPPING OF CHARGED PARTICLES BY THE MAGNETIC FIELD WITH ALLOWANCE FOR IONIZATION LOSSES

D. Kh. Morozov

Several mechanisms have been proposed for the trapping of charged particles by the geomagnetic field /1/. We shall consider here still another possible mechanism of trapping high-energy protons by the magnetic field. A method is developed for analyzing the trapping of protons at energies when the drift approximation is inapplicable. The simplified model calculations used in this paper can only provide a qualitative description of the effect, but the method as such can be extended to cover more sophisticated models.

Consider the following model: a magnetic dipole μ at the center of a spherically symmetric concentration of matter of density $\rho = \rho_0 R(r)$ is irradiated with a beam of protons of energy E_0. At $r \to \infty$ the proton beam is homogeneous and isotropic. We will consider the motion of particles in the equatorial plane of the dipole only. For $\rho_0 = 0$ (unperturbed motion), the behavior of the protons is described by Störmer's theory. The integrals of motion are

$$M_0 = \frac{m r^2 \dot{\varphi}}{\sqrt{1-\frac{v^2}{c^2}}} + \frac{e\mu}{cr} \quad \text{and} \quad E_0, \tag{1}$$

and the particle Hamiltonian is written in the form

$$H_0 = \sqrt{\left[\left(\frac{M}{r} - \frac{e\mu}{cr^2}\right)^2 + p_r^2\right]c^2 + m^2c^4}. \tag{2}$$

The particles arriving from infinity at a given point in space may have momenta ranging inside the cone of allowed directions. The interaction with matter (scattering, ionization losses) alters the particle momenta and the cone itself, and as a result particles are trapped by the magnetic field. If the perturbation caused by the material medium is small, only particles near the surface of the cone can be trapped. Scattering may cause both a change from infinite to finite motion and a change in the opposite direction. Ionization losses, on the other hand, only convert infinite motion to finite. We will consider the role of ionization losses, ignoring scattering effects. The equations of motion of the particle take the form

$$\dot{M} = -\rho \left|\frac{dE}{dl}\right| \frac{r^2\dot{\varphi}}{v}, \quad \dot{p}_r = -\frac{\partial H_0}{\partial r} - \rho \left|\frac{dE}{dl}\right| \frac{\dot{r}}{v}, \tag{3}$$

where dE/dl are the ionization losses per 1 g/cm^2.

We assume that the ionization losses for motion along an unperturbed path are much less than the energy E_0. Then $Q=\frac{1}{v}\left|\frac{dE}{dl}\right|\rho_0$ may be regarded as a small parameter, and we should take its value for $v = v_0$. The motion of ionization losses can thus be described as motion with a new Hamiltonian,

$$H = H_0 + Q H_1 , \; H_1 = R(r)\cdot\varphi\left(M - \frac{eM}{cr}\right)\frac{\sqrt{1-\frac{v^2}{c^2}}}{m} + f(M, p_r, r) \tag{4}$$

and a new retarding force

$$\mathcal{F}_r = -Q\left\{R(r)\,i - \frac{\partial}{\partial r}\left[R(r)\left(M - \frac{eM}{cr}\right)\frac{\sqrt{1-\frac{v^2}{c^2}}}{m} - f\right]\right\}.$$

Applying the ordinary theory of perturbations, as it crystallized in celestial mechanics, we make the substitution of variables /2/

$$\begin{aligned} M &= M' + Q\frac{\partial S}{\partial \varphi}, \quad p_r = p_r' + Q\frac{\partial S}{\partial r}, \\ \varphi' &= \varphi + Q\frac{\partial S}{\partial M}, \quad r' = r + Q\frac{\partial S}{\partial p_r}. \end{aligned} \tag{5}$$

The function S is defined so that to first approximation in Q, the Hamiltonian H is independent of φ'. Then M' is an integral of motion in the first approximation of the perturbation theory. To meet this condition, S should satisfy the equation

$$\frac{\partial H_0}{\partial M}\frac{\partial S}{\partial \varphi} + \frac{\partial H_0}{\partial p_r}\frac{\partial S}{\partial r} - \frac{\partial H_0}{\partial r}\frac{\partial S}{\partial p_r} = -H_1 . \tag{6}$$

This equation separates into two different equations for $p_r > 0$ and $p_r < 0$.

A particular solution of the equation for $p_r < 0$ is

$$S_1 = \varphi\int_{\infty}^{r}\frac{\left(M_0 - \frac{eM}{cr}\right)R(r)\,dr}{\sqrt{p_0^2 - \left(\frac{M_0}{r} - \frac{em}{cr^2}\right)^2}}, \tag{7}$$

and for $p_r > 0$

$$S_2 = \varphi\left[\int_{r}^{\infty}\frac{\left(M_0 - \frac{eM}{cr}\right)R(r)dr}{\sqrt{p_0^2 - \left(\frac{M_0}{r} - \frac{eM}{cr^2}\right)^2}} - 2\int_{r_{min}}^{\infty}\frac{\left(M_0 - \frac{eM}{cr}\right)R(r)dr}{\sqrt{p_0^2 - \left(\frac{M_0}{r} - \frac{eM}{cr^2}\right)^2}}\right], \tag{7'}$$

where p_0 is the unperturbed momentum of the particle, $r_{min} = (\sqrt{2}-1)\sqrt{\frac{lM}{cp_0}}$ is calculated from the unperturbed equation. These solutions where chosen so that for $r = r_{min}$, $S_1 = S_2$ and for $r \to \infty$, $S_1 \to 0$.

If R(r) falls off sufficiently fast, the particle angular momentum M after emergence from the material medium is

$$M = M_0 - 2Q\int_{r_{min}}^{\infty}\frac{\left(M_0 - \frac{eM}{cr}\right)R(r)dr}{\sqrt{p_0^2 - \left(\frac{M_0}{r} - \frac{eM}{cr^2}\right)^2}}, \tag{8}$$

where M_0 is the initial angular momentum of the particle.

The change in linear momentum for motion along an unperturbed path can also be calculated without difficulty. Upon emerging from the material medium

$$p = p_0\left[1 - 2Q\int_{\tau_{min}}^{\infty}\frac{R(\tau)\,d\tau}{\sqrt{p_0^2 - \left(\frac{M_0}{\tau} - \frac{e\mu}{c\tau^2}\right)^2}}\right]. \tag{9}$$

Note that a small perturbation may only trap particles with $M > 0$, since the linear momenta of particles with $M < 0$ lie near the axis of the cone of allowed directions. The trapping condition thus requires real positive solutions of the equation

$$\frac{p_\varphi}{p} = \frac{\frac{M}{\tau} - \frac{e\mu}{c\tau^2}}{p(\tau)} = 1. \tag{10}$$

Inserting (8) and (9) in (10) and retaining only terms of first order in Q, we obtain the equation

$$\tau^2 - \tau\frac{M^*}{p_0} + \frac{e\mu^*}{cp_0} = 0, \tag{11}$$

where $M^* = M_0(1 + 2QA) - 2QB$, $\mu^* = \mu(1 + 2QA)$,

$$A = \int_{\tau_{min}}^{\infty}\frac{R(\tau)\,d\tau}{\sqrt{p_0^2 - \left(\frac{M_0}{\tau} - \frac{e\mu}{c\tau^2}\right)^2}}, \tag{12}$$

$$B = \int_{\tau_{min}}^{\infty}\frac{R(\tau)\left(M_0 - \frac{e\mu}{c\tau}\right)d\tau}{\sqrt{p_0^2 - \left(\frac{M_0}{\tau} - \frac{e\mu}{c\tau^2}\right)^2}}. \tag{13}$$

Equation (11) is solvable if

$$\frac{M^{*2}}{p_0^2} - \frac{4e\mu^*}{cp_0} \geq 0. \tag{14}$$

In the zero approximation, this condition corresponds to the inequality

$$M \geq M_{cr}^0 = 2\sqrt{\frac{e\mu p_0}{c}}.$$

However, under our assumptions a particle is trapped whenever it reaches the material medium, so that M must be less than M_{cr}^0. The initial angular momenta of the trapped particles should therefore fall between the limits $[M_{cr}^0;\ M_{cr}^0 + \Delta M]$, where ΔM is defined by the equation

$$M_{cr}\Delta M + 2Q\left[A\left(M_{cr}^0 - \frac{2\mu e p_0}{c}\right) - BM_{cr}^0\right] = 0.$$

If R falls off sufficiently fast, A and B can be calculated as follows:

$$A = \psi_1(\tau_{min})\int_{\tau_{min}}^{\infty}\frac{R(\tau)\,d\tau}{\sqrt{\tau - \tau_{min}}},\quad B = \psi_2(\tau_{min})\int_{\tau_{min}}^{\infty}\frac{R(\tau)\,d\tau}{\sqrt{\tau - \tau_{min}}}.$$

This gives

$$B = -\frac{\sqrt{2}-1}{2}AM_{cr}^0. \tag{15}$$

Then

$$\Delta M = (\sqrt{2} - 2) Q c A M^{\circ}_{cr}. \tag{16}$$

To calculate A, we should assume a particular form for R(r). Let $R(r) = e^{-\alpha(r - r_{min})}$, then

$$\Delta M \approx -0.31 (Q/\sqrt{\alpha}) (M^{\circ}_{cr}/p_{\circ})^{3/2}.$$

All particles with momenta between $M^0_{cr} + \Delta M$ and M^0_{cr} are thus trapped by the magnetic field. Their paths are limited by the lines $r = r_{min}$ and $r = r_{max}$, where r_{max} is the first root of equation (11), which because of the smallness of the perturbation does not differ much from the corresponding magnitude in the unperturbed case. It is readily seen that even a slight change in energy is sufficient to stop the subsequent circuits of the path of the trapped particles from penetrating into the dense atmospheric layers. Indeed from equation (11) we have

$$r_{min} = -\frac{M^*}{2p_{\circ}} + \sqrt{\left(\frac{M^*}{2p_{\circ}}\right)^2 + \frac{e/M^*}{\alpha p}} \tag{17}$$

After tracing n half-circuits,

$$M^* = M_{\circ}(1 + nQA) - nQB, \; p^* = p(1 + nQA), \; \Delta p = -nQAp_{\circ}. \tag{18}$$

Inserting (18) in (17) and expanding in powers of Q, we find

$$r_{min} = r^{\circ}_{min} \left(1 - 2.4 \frac{\Delta p}{p_{\circ}}\right), \tag{19}$$

where r^0_{min} is the minimum distance from the center along the first circuit.

Thus, as the momentum drops by only 5%, r_{min} increases approximately by 800 km. As a result, the particle lifetime is sufficiently long.

Bibliography

1. Tverskoi, B.A. Dinamika radiatsionnykh poyasov Zemli (The Dynamics of the Radiation Belts of the Earth).— Moskva, "Nauka." 1968.
2. Arnol'd, V.I. — UMN, 18(6): 91. 1963.

A CONTRIBUTION TO THE THEORY OF PARTICLE ACCELERATION IN INTERPLANETARY PLASMA

M. E. Kats and A. K. Yukhimuk

The spectral density of the ionic-sound oscillations in the interplanetary space is calculated in the quasilinear approximation and the integrated intensity spectrum of the particles accelerated by these oscillations is determined. Anisotropy in the velocity distribution of the plasma particles is regarded as the reason for the development of ionic-sound oscillations /1/. The existence of this anisotropy in the solar wind plasma has been confirmed by direct measurements /2/.

The calculated intensity spectrum of the accelerated particles has the form $I(>v) = A \exp(-v/v_0)$, where A = const, v is the velocity of accelerated particles, v_0 is a characteristic constant of the spectrum. The results show that the acceleration by ionic-sound oscillations may indeed be responsible for the observed spectrum of solar cosmic rays /3/.

Bibliography

1. Timofeev, A.V. and V.N. Pistunovich.— In: "Voprosy teorii plazmy," No.5. Moskva, Atomizdat. 1967.
2. Wolfe, I.H., R.W. Silva, and M.A. Myers.— J. Geophys. Res., 71(5):1319. 1966.
3. Freier, P.S. and W.R. Webber.— J. Geophys. Res., 68(6):1605. 1963.

A MECHANISM OF ACCELERATION OF THE SOLAR WIND PLASMA

M. V. Konyukov

Data on the temperature of the solar corona, the ions, and the electrons near the Earth's orbit reveal changes of the total proton energies from -1 keV in the corona to $+1$ keV in the interplanetary plasma. This change points to the existence of a definite plasma acceleration process in the solar corona. This acceleration mechanism was studied within the framework of a steady-state spherically symmetric model of plasma ejection with steady-state almost laminar flow, and the hydrodynamic approximation was applied, at least near the starting level.* The extended energy source accelerating the solar wind plasma is distributed beyond the maximum temperature level in the solar corona (the energy flux due to thermal conductivity at this level is zero), and it is physically identical with the heat source heating the solar corona. This heat source directed away from the Sun generates an energy flux via heat conduction by the electrons, and a positive net energy flow is observed at the level corresponding to the formation of a nearly laminar plasma outflow, despite the considerable negative energy associated with the attraction of the Sun. Since the total energy flow is conserved, the proposed acceleration mechanism is essentially a mechanism transforming the energy flow associated with the electron heat conduction into a flow of hydrodynamic ion energy. This energy conversion mechanism is attributed to the presence of an ambipolar electric field and collisional energy transfer from electrons to ions.

The proposed acceleration mechanism was analyzed using the equations of steady-state spherically symmetric plasma ejection in the two-fluid approximation. The nondimensional parameters of the problem /1/ were calculated from the experimentally observed total mass flow in the solar wind, the temperature in the solar corona, and the position of the level where the nearly laminar flow conditions originated, as derived from the observed density distribution. The resulting values of the reciprocal Reynolds number are such that the asymptotic methods are not applicable, and the analysis of the solutions of the starting system of equations therefore had to be carried out numerically. Certain caution should be exercised in the application of the numerical methods to the analysis of the model equations. After all, the model equations are valid only when the

* If generation of solar wind through ejection into interplanetary space of plasma jets accelerated to considerable energies is ignored, plasma acceleration is possible only in the region of frequent collisions since it is there that the attainable energy fluxes are substantially higher than the hydrodynamic ion energy flux at the starting level. The case when the turbulent motion energy is considerably higher than the thermal energy seems to be unlikely under the conditions of the solar corona and the interplanetary plasma.

hydrodynamic approximation applies. Thus, the Cauchy problem can be formulated for the starting level, since it is chosen in the region where the hydrodynamic approximation is valid, or a boundary-value problem can be formulated choosing the levels of known velocity in the region where this approximation applies. The second level must not be chosen near the Earth's orbit, since the results of observation indicate that the hydrodynamic approximation is inapplicable in this region. Analysis of a large number of alternatives has shown that 1) the hydrodynamic ion energy flux increases due to contribution from the electron heat conduction, 2) the hydrodynamic approximation for the electrons breaks down before the electron heat conduction flux is fully transformed into the hydrodynamic energy flux. Since in the collisionless region, the energy flow by heat conduction is ruled out, a transition layer should exist between the hydrodynamic region and the collisionless region, and it is in this layer that the final acceleration of the ionic plasma component occurs.*

The acceleration mechanism of the solar wind plasma should not only raise the plasma ions to the required energy but also account for the following experimental factors: a) $T_i > T_e$ in the heat source region and $T_i < T_e$ in the interplanetary plasma, b) the temperature falls off monotonically with distance from the starting level, c) collisionless flow conditions develop. The proposed acceleration mechanism, unlike Parker's hydrodynamic acceleration mechanism and its modifications /2, 3, 4/, naturally leads to these properties of the outflowing plasma /1/.

The frozen-in magnetic fields, with small transverse components, markedly suppress the transport coefficients under the conditions of the solar corona, so that the problem becomes essentially inviscid with zero thermal conductivity. The reciprocal Reynolds and Peclet numbers calculated from these coefficients are so small that the variation of velocity and temperature can be studied using asymptotic series in powers of the reciprocal Reynolds number /5/. The equations obtained under these conditions are only compatible with Parker-type solutions, which do not meet conditions (b) and (c) above, as formulated in /6/. This implies that the contribution of magnetic fields at the source of the heat-conduction energy flow and at the site of plasma acceleration is insignificant.

Bibliography

1. Konyukov, M.V. O mekhanizme uskoreniya plazmy, vytekayushchei iz Solntsa (Acceleration of Plasma Ejected from the Sun).— Preprint FIAN, No. 149. 1967.
2. Parker, E.N. Dynamic Processes in the Interplanetary Plasma. 1965.
3. Sturrock, P.A. and R.A. Hartle.— Phys. Rev. Lett., 16:628. 1966.
4. Konyukov, M.V.— Trudy FIAN, 38:132. 1967.
5. Konyukov, M.V.— Tezisy dokladov na IV Konferentsii po kometam. Kiev, Izdatel'stvo "Naukova Dumka." 1968.
6. Konyukov, M.V. K teorii istecheniya plazmy iz Solntsa (Theory of Solar Plasma Ejection).— Preprint FIAN, No. 123. 1968.

* Difficulties associated with the solution of the rate equations in the transition layer from the hydrodynamic to the collisionless region render virtually impossible any rigorous analysis of the transition layer, even by numerical methods.

QUASIEQUILIBRIUM STRUCTURES IN THE IONIZED ATMOSPHERES OF STARS AND PLANETS

V. M. Fadeev

The interplanetary space and stellar and planetary atmospheres contain regions of completely ionized gas with particle density $n(\vec{r}, t)$ which either conduct high current densities $\vec{j}(\vec{r}, t)$ or are immersed in external magnetic fields $\vec{H}(\vec{r}, t)$. Both these factors are often combined, and the bulk of the plasma is concentrated in filaments or sheaths. Analysis of the structure of physical objects (plasma formations in this case) reduces to the study of the following three aspects: 1) existence of indivisible system components—elements, 2) interaction and transformation of elements, 3) indestructibility of the object as a system of elements. The choice of the theoretical model is governed by considerations of simplicity, without impairing the principal properties of the objects. We will use the equations describing the macroscopic properties of a singly ionized nonrelativistic ideal gas consisting of n_i ions and n_e electrons. The Maxwell tensor is approximated by the scalar pressure. Quasineutrality is furthermore assumed ($n_i \approx n_e \approx n$) and dissipative effects are ignored.

The plasma in this model is described by the following functions:

$$\rho = n_i m_i + n_e m_e = n m, \tag{1}$$

$$\vec{v} = \frac{1}{\rho}(n_i m_i \vec{v}_i + n_e m_e \vec{v}_e), \tag{2}$$

$$\vec{j} = e(n_i \vec{v}_i - n_e \vec{v}_e) \tag{3}$$

and

$$p = p_i + p_e,$$

where ρ, $\vec{v}$, $\vec{j}$, p are the density, the mean velocity, the current, and the plasma pressure, respectively.

Among the equations for these quantities, the first is the equation for the conservation of the mean momentum of the plasma as one system:

$$\frac{\partial \vec{v}}{\partial t} + (\vec{v}\nabla)\vec{v} = \frac{\vec{j}}{\rho} \times \vec{B} - \frac{\nabla p}{\rho} - \frac{m_i m_e}{e^2}\left(\frac{\vec{j}}{\rho}\nabla\right)\frac{\vec{j}}{\rho}. \tag{4}$$

The second equation is the conservation of momentum for the relative motion of the electron and the ion gas, which is interpreted as a generalization of Ohm's law:

$$\begin{aligned} &m_i m_e (\partial/\partial t + \vec{v}\nabla)\frac{\vec{j}}{\rho} = \vec{E} + \vec{v} \times \vec{B} - \frac{m_i m_e}{e^2}\left(\frac{\vec{j}}{\rho}\nabla\right)\vec{v} + \\ &+ \frac{m_i m_e (m_i - m_e)}{e^3}\left(\frac{\vec{j}}{\rho}\nabla\right)\frac{\vec{j}}{\rho} - \frac{m_i - m_e}{e}\left(\frac{\vec{j}}{\rho} \times \vec{B}\right) + \frac{1}{e\rho}(m_i \nabla p_e - m_e \nabla p_i) = \\ &= \vec{E} + \vec{v} \times \vec{B} - \frac{m_i m_e}{e^2}\left(\frac{\vec{j}}{\rho}\nabla\right)\vec{v} + \frac{1}{e\rho}(m_e \nabla p_e - m_i \nabla p_i) - \frac{m_i - m_e}{e}\frac{d\vec{v}}{dt}. \end{aligned} \tag{5}$$

The third equation is an expression of the conservation of mass:

$$\frac{\partial \rho}{\partial t} + (\vec{v}\nabla)\rho = -\rho \, div \, \vec{v}. \tag{6}$$

Maxwell's equations are also added to the set:

$$rot \, \vec{B} = \mu_0 \vec{j} + \varepsilon_0 \mu_0 \frac{\partial \vec{E}}{\partial t}, \tag{7}$$

$$div \, \vec{E} = \frac{e(n_i - n_e)}{\varepsilon_0}, \tag{8}$$

$$rot \, \vec{E} = -\frac{\partial \vec{B}}{\partial t}. \tag{9}$$

where μ_0 and ε_0 are the magnetic permeability and the dielectric constant of vacuum.

The main distinctive feature of equations (4) and (5) is that, unlike the usual practice in physics, the electron inertia terms are included. Generally /1/, the electron inertia effects are assumed to be negligible, which is not always true for a collisionless plasma ($\nu \to 0$). Electron inertia may prove significant in the region where oppositely directed magnetic fields or currents cross, as it results in a relative motion of the plasma and the field, just as collisions do.

Proceeding from the above equations, we will consider the entire question of the existence of elements in plasma systems. For an element to exist, local equilibrium conditions must be maintained, although the system as a whole may change in space and time. Therefore, let us first consider the stationary equilibrium solutions of the equations. It will be seen in the following that the most widespread structural elements are the theta-pinch, the z-pinch, and the skin pinch (a plasmoid contained in a thin skin layer).

A quasistationary ($\vec{v}(\vec{r}, t) = 0$, $\rho = \rho(\vec{r})$, $\vec{j} = \vec{j}(\vec{r})$) theta-pinch is described by the following equations:

$$\frac{\vec{j}_\varphi}{\rho} \frac{1}{r} \frac{d}{dr}(r A_\varphi) - \frac{u_s^2}{\rho} \frac{d\rho}{dr} + \frac{m_i m_e}{e^2} \left(\frac{j_z}{\rho}\right)^2 \frac{1}{r} = 0, \tag{10}$$

$$-\frac{d}{dr}\left[\frac{1}{r}\frac{d}{dr}(r A_\varphi)\right] = \mu_0 j_\varphi, \tag{11}$$

$$\frac{j_\varphi}{\rho} = \frac{e}{m_i + m_e} \omega r, \tag{12}$$

$$E_r = \frac{m_e^2 u_{se}^2 - m_i^2 u_{ii}^2}{e} \frac{1}{\rho} \frac{d\rho}{dr}, \tag{13}$$

$$\frac{dE_r}{dr} = \frac{e(n_i - n_e)}{\varepsilon_0}, \tag{14}$$

where ω = const is the angular drift velocity of the electrons in an inhomogeneous magnetic field; equation (12) is the partial solution of equation (5) for the φ-component. Equation (13) corresponds to the r-component of Ohm's law and can be applied to determine the space charge field. Eliminating j_φ between (10) and (11) and inserting the integral of (10) in (11), we find

$$d^2\Psi/d\rho^2 + G_n'^2 e^{\Psi} = 0. \tag{15}$$

where

$$\rho = r^2, \quad G_N'^2 = \mu_0 e^2 \omega^2 \rho_0 / 4 (m_i + m_e)^2 u_s^2,$$

$$\psi = \frac{m_i m_e}{2 u_s^2 (m_i + m_e)} r^2 + \frac{e\omega}{u_s^2 (m_i + m_e)} r A_\varphi .$$

The solution of equation (15) studied in /2/ is a theta-pinch of the characteristic size

$$\delta_N = \left[\frac{u_s^2}{(\omega_B \omega - \frac{m_i m_e}{(m_i + m_e)^2} \omega^2)} \right]^{1/2} , \tag{16}$$

where $\omega_B = eH_0/m_i + m_e$. For $\omega \geq eH_0/(m_i + m_e)/m_i m_e$ the structural element loses its identity. The distribution of the magnetic field B_z, the plasma density ρ, and the current density j_φ, is shown in Figure 1.

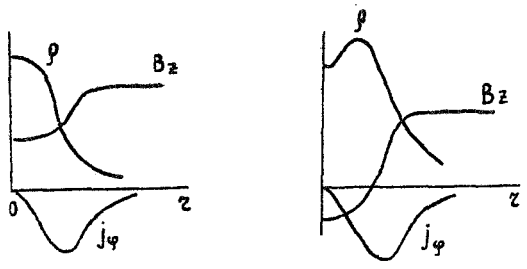

FIGURE 1. Qualitative distribution of the magnetic field B_z, plasma density ρ, and current j_φ for a theta-pinch plasmoid.

Note that, depending on the relationship of the parameters characterizing the gas-kinetic and the magnetic pressure, we have two different density distributions: a bell-shaped distribution and a pipe-shaped distribution. In the case of a pipe-shaped distribution, the inner magnetic field of the plasma is even greater than the external magnetic field, and the field reverses its polarity at the center of the plasmoid.

The existence of a z-pinch follows from the equations

$$\frac{j_z}{\rho} \frac{dA_z}{dr} - \frac{u_s^2}{\rho} \frac{d\rho}{dr} = 0, \tag{17}$$

$$-\frac{1}{r} \frac{d}{dr} \left(r \frac{dA_z}{dr} \right) = \mu_0 j_z , \tag{18}$$

$$\frac{j_z}{\rho} = \frac{e}{m_i + m_e} v_{oz} , \tag{19}$$

$$E_r = \frac{m_e^2 u_{se}^2 - m_i^2 u_{si}^2}{e} \frac{1}{\rho} \frac{d\rho}{dr} , \tag{20}$$

$$\frac{dE_r}{dr} = \frac{e(n_i - n_e)}{\varepsilon_0} , \tag{21}$$

where v_{oz} = const is the drift velocity of electrons in an inhomogeneous magnetic field. Equation (19) is a particular solution of equation (5) for the z-component, and equation (20) is the solution for the r-component.

Using (19) to eliminate j_z from (17) and (18), integrating (17), and inserting the result in (18), we get

$$\frac{1}{\tau}\frac{d}{d\tau}\left(\tau\frac{d\psi}{d\tau}\right) + G_E^2 e^{-\psi} = 0, \tag{22}$$

where $G_E^2 = \mu_0 e^2 \rho_0 v_{0z}^2 / (m_i + m_e)^2 u_s^2 = \mu_0 j_0^2 / p_0$, ρ_0 is the density at a fixed point, $\psi = -\frac{e v_{0z}}{(m_i + m_e) u_s^2} A_z$.

The solution of equation (22) describes a z-pinch /3/ with a characteristic transverse dimension

$$\delta_E = \left[\frac{(m_i + m_e)^2 u_s^2}{\mu_0 e^2 \rho_0 v_{0z}^2}\right]^{1/2} = \left(\frac{p_0}{\mu_0 j_0^2}\right)^{1/2} \tag{23}$$

The distribution of the magnetic field B_φ, the plasma density ρ, and the current j_z is shown in Figure 2.

To establish the existence of a quasistationary skin layer, we use equations (4)—(9). In connection with Ohm's law (5), we take

$$\vec{j} \perp \vec{v}, \tag{24}$$

$$\operatorname{rot} \vec{v} = 0. \tag{25}$$

Decomposing $\vec{E}$ into two components $\vec{j} \parallel \vec{E}_\parallel$ and $\vec{j} \perp \vec{E}_\perp$ and using (4), we replace (5) with two equations:

$$\frac{m_i m_e}{e^2}\left(\frac{\partial}{\partial t} + \vec{v}\nabla\right)\frac{\vec{j}}{\rho} = \vec{E}_\parallel + \vec{v} \times \vec{B} - \frac{m_i m_e}{e^2}\left(\frac{\vec{j}}{\rho}\nabla\right)\vec{v}, \tag{26}$$

$$\vec{E}_\perp = \frac{1}{e\rho}\left(m_e \nabla p_e - m_i \nabla p_i\right) - \frac{m_i - m_e}{e}\frac{d\vec{v}}{dt}. \tag{27}$$

Vector identities and conditions (24), (25) help to reduce equation (26) to the form

$$\frac{m_i m_e}{e^2}\frac{\partial}{\partial t}\left(\frac{\vec{j}}{\rho}\right) - \vec{E}_\parallel = \vec{v} \times \left(\frac{m_i m_e}{e^2} \operatorname{rot} \frac{\vec{j}}{\rho} + \vec{B}\right). \tag{28}$$

Equation (28) is an identity if

$$\frac{m_i m_e}{e^2}\frac{\partial}{\partial t}\left(\frac{\vec{j}}{\rho}\right) = \vec{E}_\parallel, \quad \frac{m_i m_e}{e^2} \operatorname{rot}\left(\frac{\vec{j}}{\rho}\right) = -\vec{B}. \tag{29}$$

For $\rho = \rho_0 = \text{const}$, equations (29) are the ad hoc relationship introduced by London /4/ to explain superconductivity in metals at ultralow temperatures. We see now that these equations are in fact a consequence of Ohm's law when dissipative effects are ignored. Changing over to the potential $\vec{A}(\vec{r}, t)$, we get from (29)

$$\frac{\vec{j}}{\rho} + \frac{e^2}{m_i m_e}\vec{A} = \vec{C}. \tag{30}$$

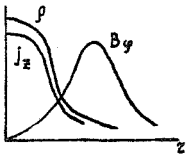

FIGURE 2. Distribution of B_φ, ρ and j_Z in a z-pinch.

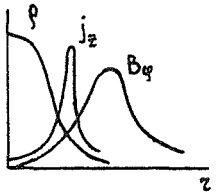

FIGURE 3. Distribution of B_φ, ρ, and j_Z according to Weibel /5/.

Analogous solutions can be expected following the application of (30) to equations (4)—(9). Indeed, for the steady-state case $\vec{A} = \vec{A}(\vec{r})$, Weibel /5/ obtained a computer solution of the form shown in Figure 3. In the one-dimensional plane case $\partial/\partial z = \partial/\partial y = 0$, $\vec{A} = \hat{z}A$, the problem reduces to the equation

$$d^2\psi/d\xi^2 - \psi e^{-\psi^2} = 0, \tag{31}$$

which is readily solved in quadratures:

$$\xi = \int \frac{d\psi}{\sqrt{C - e^{-\psi^2}}} + C_1, \tag{32}$$

where

$$\psi = e/\sqrt{m_i m_e}\, u_s, \quad \xi = e\sqrt{\mu_0 \rho_0 / m_i m_e}\, x.$$

Unfortunately, further integration is impossible, and only qualitative analysis or machine solution should be attempted. The characteristic thickness of the skin layer is

$$\delta_j = (m_i m_e/\mu_0 \rho_0 e^2)^{1/2} \tag{33}$$

Combination of two or three structural elements may lead to more complex configurations, some of which have been studied in /6—8/.

Cylindrical waves propagating in a cold thin plasma transversally to a strong magnetic field were studied in /6/. A set of equations similar to our equations (4)—(9) were solved by numerical integration. Figure 4a shows the typical time and space pattern of the magnetic field B_Z directed along the plasma cylinder. The profiles of the density ρ (Figure 4b) and the current j_φ (Figure 4c) were obtained by an appropriate reduction of the magnetic field profile.

Comparison of the ρ, j_φ, and B_Z in Figure 4 with the corresponding profiles in Figure 3 shows that the curves are completely analogous. Note that although the problem is time-dependent, equation (33) is nevertheless valid for the characteristic size of the current sheath. The formation of a bundle of plasma sheaths observed as the amplitude of the tube of force lines of the initial magnetic field H_{0Z} increases can be apparently interpreted as a result of particle trapping by the magnetic field associated with electron inertia.

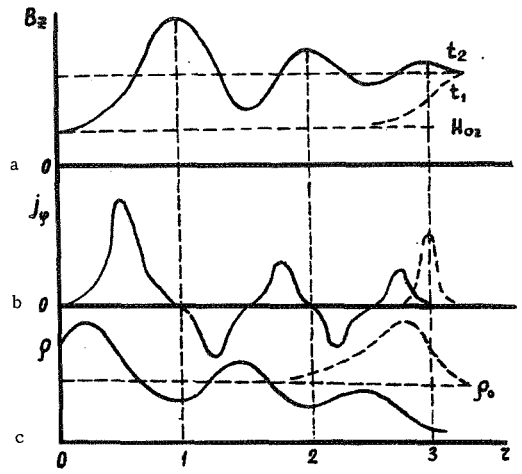

FIGURE 4. Time and space profiles:

a) magnetic field B_z, b) current j_φ, c) plasma density ρ.

A solution corresponding to a plasma sheath contained by the magnetic field of the plasma own current showing a space-periodic structure was derived in /7/. The characteristic sheath thickness is equal to the characteristic filament thickness, where each filament is a local Bennett pinch with δ_E expressed by (23). The inhomogeneous state was proved to be energetically advantageous for the case of a cylindrical current sheath with a z-pinch space-periodic structure /8/. It was moreover established that the number of filaments in a plasma sheath is of the order of magnitude of $I^2/NkTc^2$, where I and N are the total current and the linear number of particles in the current sheath, k is Boltzmann's constant, c is the velocity of light.

The peculiar feature of a self-pinched current sheath is the presence of a neutral plane where the antiparallel magnetic fields cross, so that the conversion of the homogeneous layer into a filamental layer is essentially a topological process. We can thus naturally expect a solution analogous to that derived in /7, 8/ to exist for the case of a plasma sheath focused in a homogeneous magnetic field by the diamagnetic effect of antiparallel plasma currents. The antiparallel currents cross at the neutral plane during the topological readjustment of the sheath. The corresponding topological structure is diagrammed in Figure 5.

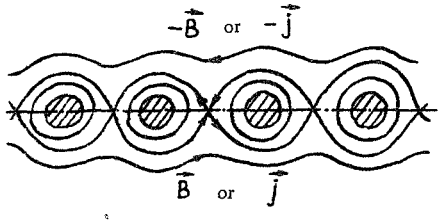

FIGURE 5. Topological conversion of a homogeneous layer into a filamental layer.

The z-pinch and the theta-pinch may form a combined pinch, which will display self-focusing under certain conditions, even without an external field and despite the defocusing effect of the internal field B_z. The necessary condition is that the kinetic pressure and the magnetic pressure of the

longitudinal field be balanced by the pressure of the azimuthal focusing field B_φ.

In auroral regions, the electrons spilling out of traps form high currents with densities of $\vec{j} = 10^{-10} - 10^{-11}$ A/cm^2. Typical temperatures and fields are $T_e = 5 - 10$ keV and $B = 5 \cdot 10^{-1} - 10^{-3}$ gauss. For these parameters, δ_E and δ_j range from a few kilometers to hundreds of kilometers, δ_H is of the order of hundred meters. The magnetosphere tail may have a filamental current structure /7/. For $n < 10$ cm^{-3}, $\varepsilon_p = 0.5 - 1$ keV, $B \sim 2 \cdot 10^{-4}$ gauss, $V_{e0} \sim 2 \cdot 10^6$ cm/sec, the characteristic filament size is $3 \cdot 10^3$ km. The characteristic size of the inhomogeneities for the case studied on PIONEER-6 with the parameters $\varepsilon_p = 13$ MeV, $B = 3 \cdot 10^{-4}$ gauss is

$$\delta_H = 1.4 \cdot 10^4 \text{ km for } \omega = \omega_B ; \quad \delta_H = 10^6 \text{ km for } \omega = 10^{-3}\,\omega_B .$$

If we assume that the fine structure of the galactic arms is determined by the balance between the gas-kinetic and the magnetic pressure and take $B = 10^{-6}$ gauss and $\varepsilon_p = 10^9 - 10^{11}$ eV, we find $\delta_H = 3 \cdot (10^{15} - 10^{16})$ cm for $\omega = \omega_B$ and $\delta_H = 10^{18}$ cm for $\omega \sim 10^{-3}\,\omega_B$. The fit between the observed and the calculated inhomogeneity sizes is really striking for such a crude model.

Further development of the theory should take into account the entire range of experimental factors, including dynamic and dissipative effects. As an example, let us consider the development of polar aurorae of layered and ray structure. Our results suggest the following mechanism of auroral development. Near the geomagnetic pole (the auroral oval), the geomagnetic field lines form a quasicylindrical bundle. The bundle is pinched and then expands following the interaction with the solar wind on the day side and the field lines in the wake of the magnetosphere tail. As a result, an induced field is formed (simultaneously or with a certain time lag):

$$E \sim \delta H / \tau c .$$

Taking $\delta \sim 4 \cdot 10^7$ cm, $H = 10^{-1}$ gauss, $\tau = 10^3$ sec, we get $E \sim \frac{4 \cdot 10^7 \cdot 10^{-1}}{10^3 \cdot 3 \cdot 10^{10}} 300 = 4 \cdot 10^{-5}$ V/cm, which is close to the usual mean field value in polar aurorae. This field is directed along the "oval" in the westward direction for increasing $\vec{H}_0$ and in the eastward direction for a decreasing field; it is distinctly rotational. Since the pinching is asymmetric, the maximum density of field lines is observed on the side where the incoming particles are incident (the day side) or where the external field lines touch (the night side). According to /6/, sheaths of increased density and increased current move to the pole. Streams of high-energy particles penetrating into the current sheaths from the direction of the magnetosphere tail create a system of longitudinal currents which, because of possible inhomogeneities or instabilities, will break into filaments preferentially directed along the magnetic field $\vec{H}_0$ (combined z-theta filaments). This mechanism does not clash with Piddington's theory, and yet it explains the fine structure of the layered and ray aurorae.

Equations (4)—(9) can be applied to consider the crossing of the magnetic field lines in the magnetosphere tail, which is topologically permissible. The dissipation mechanism of the magnetic field in the region where the field lines cross is not clear, however, although dissipation may definitely

take place for $\nu \to 0$. It is shown in /9/, for example, that the electron inertia remains analogous to the collision effects in the sense that it causes effective relative motion of the plasma and the field even for $\nu \to 0$. The problem reduces to the solution of the equations

$$\frac{\partial \vec{v}}{\partial t} = grad\left[\frac{m_i m_e}{2e^2}\left(\vec{c} - \frac{e^2}{m_i m_e}\vec{A}\right)^2 - u_s^2 \ln\rho - \vec{v}^2/2\right],$$

$$\Delta\vec{A} - \varepsilon_0\mu_0 \frac{\partial^2\vec{A}}{\partial t^2} + \mu_0\rho\left(\vec{c} - \frac{e^2}{m_i m_e}\vec{A}\right) = 0,$$

$$\partial\rho/\partial t + (\vec{v}\nabla)\rho = -\rho\, div\, \vec{v},$$

which are derived from (4)—(9) under conditions (24)—(25).

Bibliography

1. Physics of Plasma and Magnetohydrodynamics.— Moskva, IL. 1961. [Russian translations.]
2. Komarov, N.N. and V.M. Fadeev.— ZhETF, 41(2/8):528. 1961.
3. Komarov, N.N. and V.M. Fadeev.— ZhTF, 32(2):133. 1962.
4. de Gennes, P.G. Superconductivity of Metals and Alloys. Translated by P.A. Pincus. — New York, Benjamin. 1966.
5. Weibel, E.S.— Phys. Fluids, 2(1):52. 1959.
6. Berezin, Yu.A.— PMTF, 1:107. 1966.
7. Fadeev, V.M., I.F. Kvartskhava, and N.N. Komarov.— Yadernyi sintez, 5:202. 1965.
8. Komarov, N.N., I.F. Kvartskhava, and B.M. Fadeev.— Yadernyi Sintez, 5:192. 1965; Tezisy dokladov na V Vsesoyuznoi ezhegodnoi zimnei shkoly po kosmofizike. Apatity, Izd. Kol'skogo filiala AN SSSR. 1968.
9. Furth, H.P. Nuclear Fusion, Suppl., Part 1, p.169. 1962.

RADAR ASTRONOMY OF THE SUN

I. M. Gordon

The basic aspects of the radar astronomy of the Sun were first formulated by N. D. Papaleksi in 1946. Following his suggestion, Ginzburg computed the absorption of radio waves in the solar corona /1/. The theory of formation of a reflected signal /2 – 5/ amounts to the following. The ray penetrating into the corona is refracted and, on reaching the point nearest the Sun's center, where the refractive index is close to zero, it is scattered by the electron density inhomogeneities. This scattering is either isotropic or Lambertian. Integrating over the power scattered in the direction of the receiving antenna and allowing for absorption due to Coulomb collisions along the direct and the return paths in the corona, we find the expected power of the reflected signal which is received by the observer. Note that the particular choice of the scattering function does not significantly change the expected result. The receiver power is generally comparable with the power of the signal reflected by an isotropic reflector of area $\pi R_{\odot}^2$. The effective cross section within the framework of the existing theory is essentially determined by the absorption in the corona, i.e., by the global distribution of electron concentration and temperature in the corona. It should be stressed that these parameters are highly stable. Even their variations in the course of the 11-year cycle lead to only insignificant changes in the effective diameter. There is naturally a possibility that the local values of these parameters, e.g., above active regions, may change between wide limits, but since the area of these formations constitutes an insignificant fraction of the Sun's surface, no substantial change (e.g., by one order of magnitude) will be observed in the estimated value of the effective cross section. The higher the frequency, the deeper it penetrates into the corona. Since the collision frequency increases with depth, signal damping is more pronounced at higher frequencies and the effective scattering diameter decreases. The low-frequency range is thus more promising for solar radar astronomy. However, the size of antennas needed to attain satisfactory beam widths imposes a technical limit on the expansion toward longer wavelengths.

The first successful attempt of radar probing of the Sun at 25.6 MHz did not yield any detailed information about the solar corona, since both the antenna size and the transmitter power were low /6/. Systematic experiments aimed at bouncing radar waves of 38 MHz frequency off the Sun were begun in 1964, using a special MIT antenna at El Campo /4, 5/. The knife-edge beam measuring $0.75° \times 6.5°$ permitted making one experiment daily, when the Sun was crossing the meridian. The transmission of the coded signal was 16 min long, and after that the

reception of the bounced signal would begin. Unfortunately, the low resolving power precluded probing separate parts of the solar corona, and the long averaging period made it impossible to study the structure of the reflected signal during a single session. Nevertheless, prolonged systematic experiments revealed highly significant and unexpected data concerning the structure of the reflected signal and the effective cross sections.

The effective cross section was found to vary between unusually wide limits — from a few hundredths to several tens of $\pi R_\odot^2$. These changes are particularly surprising, since within the framework of the current theory they entail enormous changes in the global values of the parameters n_e and T_e, which are definitely unacceptable. The variation of the effective cross section by as much as three orders of magnitude is in striking contrast to the observed stability of the mean values of the parameters of the quiet corona, where the reflected signal forms according to current notions. The structure of the signal reveals similarly surprising features. Together with the "violet" components, corresponding to ascending motions, the signal also contains "red" components, which should correspond to descending motions. The quasi-symmetric distribution of the reflected signal over the frequency shifts should be interpreted, within the framework of the theory of signal reflection from moving inhomogeneities, as an indication of the equiprobable occurrence of ascending and descending motions. This result is at variance with the theory of the solar wind.

Another remarkable feature of the reflected signal structure is the presence of extremely high reflections, up to $3R_\odot$ and higher, whereas the altitude of the layer with n = 0 corresponds to the stationary corona $\sim 1.4 R_\odot$. Reflection at the $3R_\odot$ altitude requires an electron density exceeding hundred-fold the density of the undisturbed corona.

These puzzling results indicate that the radar observations of the Sun cannot be interpreted within the framework of the existing theories. In particular, the existence of effective cross sections $\sim 100 \pi R_\odot^2$ requires high directivity of the bounced signal, since the Sun's image will be much greater than the antenna beam width. The directivity requirements become even more exacting if we remember that, according to /4/, there are periods of high correlation with the area of the flocculi in the central part of the disk (up to +0.95). Hence the conclusion that at least in these periods, most of the components of the reflected signal originated in the corona above the flocculi. Now, since the area of the flocculi is a mere 1% of the visible disk area, and the effective cross sections reached a few $\pi R_\odot^2$ units, it is clear that the reflection should be extremely directional /7 — 10/.

The assumption that most of the reflected signal components form in the corona above the flocculi is borne out by the fact that the spectra of the type-A reflected signal (whose principal components form in a thin layer of the corona at distances between 1.3 and $1.6 R_\odot$ from the center in the direction to the observer) appeared only when a flocculus was observed at the center of the disk. Besides a characteristic structure which proved totally incompatible with the assumption of signal formation by reflection from the global corona, type-A spectra were found to correspond to high effective cross sections. With noncentral flocculi, the effective cross section diminishes and the signal forms at substantially greater depths (type B).

Once type-A signals have been identified with the coronal regions above flocculi, we can find the solar wind velocity gradient above the active regions of the corona. Assuming that the mean frequency shift of a given coronal layer corresponds to the velocity of the plasma in which the signal originates (this is a straightforward conclusion from the scattering mechanisms considered below), we note that a rapid increase of velocity with altitude is sometimes observed above the active corona. This velocity gradient considerably exceeds that predicted by Parker's theory.

The fundamental difficulties encountered in the interpretation of the radar observations of the Sun within the framework of the existing theories indicate /7 — 10/ that the formation of the reflected signal is mainly governed by induced processes of interaction of electromagnetic waves with various wave modes excited in the turbulent coronal plasma /11 — 12/. An example of processes of this kind is provided by the Raman scattering of electromagnetic waves by Langmuir, magnetic-sound, and ionic-sound waves, "whistlers," etc. The limited applicability of computations which ignore the interactions with plasma turbulences was commented on in /3/.

These mechanisms may in principle account for all the observed properties of the reflected signal: the quasi-symmetry in the distribution of the frequency shifts is a result of the frequency change in Raman scattering, $\nu \rightarrow \nu + \nu^p$; the high effective cross sections are the result of predominant back scattering; finally, the high reflections are the result of strong plasma turbulence in the high coronal layers /7 — 10/.

Momentum conservation considerations lead to the following necessary condition for back scattering: $K^p \sim 2K^t$, where K^p and K^t are, respectively, the wave numbers of the wave in plasma and of the electromagnetic wave. In other words, a necessary condition of back scattering is $\lambda^p = \frac{\lambda^t}{2}$.

Let us now consider what wave modes in plasma will produce, through Raman scattering, reflected signal components with the observed frequency shifts $\pm 60 - 80$ kHz. The scattering by Langmuir waves clearly cannot be responsible for the components observed in radar experiments, since it should lead to excessively large frequency shifts. Scattering by magnetic-sound and Alfven waves will not produce back scattering, since it is impossible to satisfy simultaneously the condition of back scattering and the condition which requires that the frequency shifts be equal to the frequency of the scattering waves. The physics of this effect is quite simple. To achieve frequencies of up to 60 — 80 kHz, a sufficiently strong magnetic field is needed. However, for these magnetic field strengths, the velocity and thus also the wavelength are substantially greater than the velocity and the wavelength of the signal. As a result, the signal will undergo small-angle scattering, whereas we are interested in scattering at angles close to 180°. Scattering by "whistlers" cannot produce back-scattering either, since the required characteristics are such that the waves will experience strong Cherenkov damping. Scattering by ionic-sound waves for various values of the electron temperatures and various levels of the ionic-sound turbulence may account for the formation of components with large frequency shifts /7 — 10/.

Excitation of weakly damped ionic-sound waves is possible only in a nonisothermal corona when $T_e \gg T_i$. The radar observations of the Sun at 38 MHz thus apparently indicate the possible formation of extensive

coronal regions with "hot" electrons and "cold" ions above the flocculi. Signal components with small frequency shifts are apparently associated with induced scattering on thermal ions. We have noted above that the fairly narrow angular distribution of the back scattered signal, determined by the k-spectrum of the scattering waves, accounts for the exceptionally large effective cross sections. The increase of the effective cross section may also be associated with the amplification of the signal during its propagation in coronal plasma.*

The "plasma" mechanism of signal reflection naturally explains why the cases of large effective cross sections invariably coincided with enhanced level of solar radio emission and strong fluctuations of its intensity. This distinct correlation is attributable to the fact that the scattering of electromagnetic waves by ionic-sound waves produces the reflected signal components, whereas the scattering of Langmuir waves by the ionic-sound waves in the same volume of turbulent plasma constitutes the source of solar radio emission. The above model can be checked experimentally. The amplification of the reflected signal from any level in the corona is naturally expected to be accompanied by an enhancement of the solar radio emission at the first and second multiples of the electron plasma frequency. Since the altitudes from 1.4 to $3R_\odot$ correspond to Langmuir frequencies from 38 to about 5 MHz, the emission of the turbulent plasma can be detected in the frequency band between 5 and 78 MHz. The attempts to discover signal components scattered by Langmuir waves also deserve attention.

It follows from the preceding that when radar observations are carried out with adequate resolution, the radar picture of the Sun will not be unlike the standard X-ray photographs of the Sun, where the flocculi appear as bright spots against the dark background of the quiet corona /9, 10/. The reason for this likeness is quite obvious. The source of solar X rays is the dissipation of plasma turbulence, while the reflected signal is in fact formed by scattering off the waves in the plasma in somewhat higher layers of the corona /9, 10/. It should be noted, however, that the obvious program which calls for an increase of the resolving power and a reduction of the signal averaging time encounters a number of serious difficulties: the powerful beam of electromagnetic waves proves to be unstable, since induced decay processes may lead to an avalanche growth of Langmuir waves and exponential extinction of the signal. The physical nature of the plasma thus sets an obvious limit to resolving power and time resolution which can be attained in radar observations.

One of the significant results of radar observations indicates that the signal power reflected by a "quiet" corona is either very low or zero. This conclusion primarily follows from the fact that in a number of cases the effective reflection cross section was less than a few hundredths of $\pi R_\odot^2$. Therefore, at least on these days, the "quiet" corona did not reflect at all, or in any event its reflectance was substantially less than the theoretically predicted figure. In view of the stability of the mean characteristics of the "quiet" corona, its contribution to the reflected power is probably low in other cases too. This conclusion is borne out by an analysis of type-A spectra, where the main components originate in

* V.A. Kotel'nikov called our attention to this point during the discussion of I.M. Gordon's paper at the November, 1968, session of the Department of General Physics and Astronomy of the USSR Academy of Sciences.

coronal regions above flocculi, and the total power of the diffuse components whose origin is still uncertain is low. There is no doubt that the interpretation of this fact may yield valuable information about physical processes in the "quiet" corona.

In conclusion let us consider the prospects of radar observations at other, in particular higher, frequencies. Note that the very existence of high reflections and the theory of scattering by plasma waves suggest that high-frequency radar observations of the Sun will probably prove much more fruitful than previously thought. It can be shown that the expected frequency shift in back scattering by ionic-sound waves and by particles is proportional to the frequency of the signal. Thus in high-frequency radar observations, the receiver pass band should be increased. Parker's theory predicted small expansion velocities deep inside the corona and we could thus expect substantially smaller frequency shifts for signal reflection from moving inhomogeneities. This was probably the reason for the failure of the radar observations of the Sun at 430 MHz. Another reason for the failure of these observations could be the low solar activity in the relevant period. It should be emphasized that the extremely valuable information about physical processes in the solar corona which can be obtained from radar observations at various frequencies provides more than sufficient justification for performing these observations in the nearest future.

Bibliography

1. Ginzburg, V.L.— DAN SSSR, 52:487. 1946.
2. Herr, E.— Proc. IRE, 40:660. 1952.
3. Bass, F.G. and S.Ya. Braude.— Ukrainskii Fizicheskii Zhurnal, 2:149. 1957.
4. James, J.C.— IEEE Trans. Antenna and Prop., A-12:876. 1964.
5. James, J.C.— Astrophys. J., 146:356. 1966.
6. Eshleman, V., R. Barthle, and P. Gallagher.— Science, 131:329. 1960.
7. Gordon, I.M.— Astronomicheskii Zhurnal, 45:1002. 1968; ATs, No.447, 30 October 1967.
8. Gordon, I.M.— Astrophys. Lett., 2:49. 1968.
9. Gordon, I.M.— Astrophys. Lett., 3. 1969. (In press).
10. Gordon, I.M.— ATs, No.487. 29 October 1968.
11. Tsytovich, V.N.— UFN, 90:435. 1966.
12. Tsytovich, V.N. Nelineinye protsessy v plazme (Nonlinear Processes in Plasma). Moskva. 1967.

PENETRATION OF AURORAL PARTICLES INTO THE EARTH'S ATMOSPHERE

L. L. Lazutin

During worldwide and polar magnetic storms, complex dynamic processes take place in the Earth's magnetosphere, involving interaction between charged particles, electric and magnetic fields, plasma and electromagnetic waves. These interaction processes accelerate the particles and cause their injection into the Earth's atmosphere at high latitudes. The present review summarizes the characteristics of the injected auroral particles; the atmospheric consequences of this injection (polar aurorae, geomagnetic storms, etc.) and the prehistory of auroral fluxes, i.e., the magnetospheric processes, are considered only in broad outline. The currently available characteristics of the injected particles were mainly derived from observations of aurorae /1, 2/, the absorption of radio noise from outer space /3, 4/, measurements from stratospheric balloons, rockets /5/, and polar-orbit satellites /6/. Each of these methods has its own advantages and shortcomings, and the main points are summarized in the table below.

A significant portion of the characteristics of auroral fluxes discussed in this review were obtained from stratospheric observations. The main advantage of the stratospheric methods is that they provide continuous data over a long period and measure the spectrum and the distribution of the time and space characteristics of the fluxes; the shortcomings of these methods include the limited spectrum range (> 20 keV) and the limited variety of determinable particle species (electrons only).

The second most extensive source of information — polar aurorae — is produced mainly by electron fluxes with energies from 1 to 10 keV.* Hence the origin of the distinction between soft and hard electron fluxes, which is used in what follows. It should be stressed that there is more to the concept of soft and hard electrons than a mere difference in methods of observation.**

In studying particle injection at high latitudes — admittedly a complex phenomenon — there can be several alternative approaches to the analysis of experimental data. The first (the simplest and the oldest) method aims at elucidating the space, time, and energy statistical characteristics of all the particle showers in general. This averaging obliterates numerous important characteristics, but brings out the general pattern of the process, a certain model which may occasionally prove to be aesthetically attractive

* The proton fluxes on the average are one order of magnitude smaller and show a substantially more homogeneous distribution in time and in space. We will therefore deal mainly with electron fluxes. Moreover, the number of direct measurements of auroral protons is unfortunately small.

** The methods and the instruments for X-ray measurements in the stratosphere are described by I. A. Kuz'min in his paper "Instrumentation for the Measurement of X-ray Bremsstrahlung in the Stratosphere in the Zone of Aurora Borealis" in Part 2 of the Proceedings.

(e.g., the Khorosheva – Feldstein ring – oval). The second approach calls for the identification of individual shower types with common energy and dynamic characteristics which are confined to some closed region in space. If a certain type of particle shower has been identified with fair certainty, we can say that the different disturbances are governed by the same acceleration mechanism and that the particle fluxes have the same history in the interval (both space and time) between acceleration and injection into the atmosphere.

Evaluation of various methods of observation as a source of information on the characteristics of auroral particles

Form of observation	Energy range, eV	Flux, spectrum	Angular distribution	Spatial distribution, motion	Variations	Observation time
Polar aurorae	10^2—10^4	Indirectly, from glow altitude and intensity	-	Excellent within limits of instrumental resolution		~10 hrs
Riometers	10^4—10^5	Very roughly from frequency dependence	-	Roughly, using the riometer network	Satisfactory for periods greater than 1 min	Continuously
Radiosondes	$2 \cdot 10^4$—10^6	Adequately, from the X-ray spectrum	-	Roughly from several instrument launchings in different locations, more precisely from combined measurements of narrow-beam detectors	Satisfactory within the limits of instrumental resolution	~10 hrs
Rockets	10^2—10^6	Satisfactory	+		Rapid variations	A few minutes
Satellites	10^2—10^6	Satisfactory, with some time and space averaging	+	Averaged characteristics, hard to separate from time variations	Rapid variations	A few minutes

The third approach calls for a comprehensive analysis of the development of a particular electromagnetic disturbance (a magnetospheric substorm). We are fairly close to perfecting a general model of the magnetospheric substorm, but individual disturbances greatly differ from one another and generalizations based on insufficient material must be avoided. This is a much more difficult approach, since it requires simultaneous measurements by a wide range of ground and airborne instruments. Therefore, it is only recently that publications of this class appeared in the literature /8, 9, 10/. We will not consider this approach in our review.

A general theory probably will be developed only after some progress has been made in the third stage of experimental research, but this is by no means a universal opinion, and the attempts to create a comprehensive theory of polar aurorae are not a passing fashion /11/.

The statistical features of the injection of auroral particles, which have been firmly established by now, amount to the following:

A. The particle injection is highly nonuniform in space and in time; the electron flux may vary by a factor of 10^6 (from 10^2 to 10^7 $(cm^2 sec\ sterad)^{-1}$ for E > 40 keV /6/); the rate of change may reach about one order of magnitude in 5 msec /12/ and the corresponding spatial scale is a few hundreds, and possibly tens, of meters at the boundary of the atmosphere /13/.

B. The particle injection zones form a fairly definite configuration, which hardly changes with time or with the level of magnetic activity. This configuration is fixed relative to the Earth—Sun direction, and the Earth (with the entire network of geophysical stations) spins under it.

C. In the midnight sector, the injection of both soft and hard auroral particles occupies a fairly narrow (5—10°) belt around geomagnetic latitude 65°.

D. The injection belt is split into two around noon; the hard electrons enter the atmosphere approximately at the same latitude as at night, whereas the soft electrons are injected in a narrow belt around 75°.

E. The particle showers near the pole show a greater stability in time; the particle fluxes and the energies are substantially lower than in the auroral zone.

F. In the afternoon sector, the average electron flux reaches a minimum.

These are the basic firm data on the spatial distribution of particle injection. Some less certain, but more detailed models will be considered below.

The data regarding the energy characteristics of the auroral electrons are less certain. The data on polar aurorae (altitude, relation to auroral absorption of radio noise from outer space) show that the average electron energy is substantially softened along the inner oval, from night side to day side /1/. In the outer ring, a reverse situation is observed: the hardest electron fluxes are observed in the morning /14/. Stratospheric data reveal a more complex variation of the energy of hard electrons during the day /15, 16/ (Figure 1).

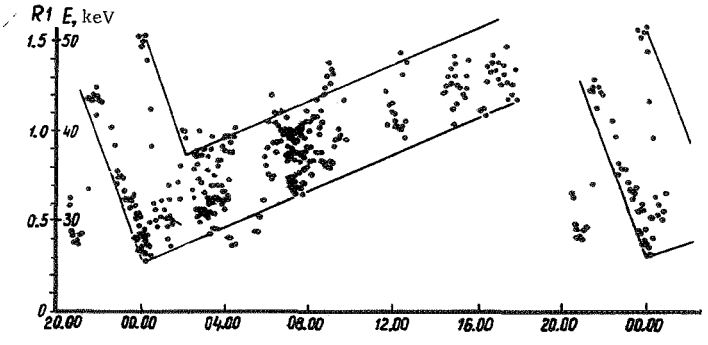

FIGURE 1. The diurnal variation of the spectral changes of the X-ray flux.

There are very few direct measurements of particles in the daytime inner injection zone; detailed studies based on the measurements of polar aurorae were carried out by Starkov and Fel'dshtein /17, 18/, and we will therefore consider the outer injection ring.

EVENING AND MIDNIGHT SHOWER TYPES

The injection of auroral particles reaches its most complex and dynamic character around midnight. Although numerous authors analyzed ground and stratospheric measurements of the midnight particle showers, the nature of the process can be described only in rough outline, with much less precision than for other shower types.

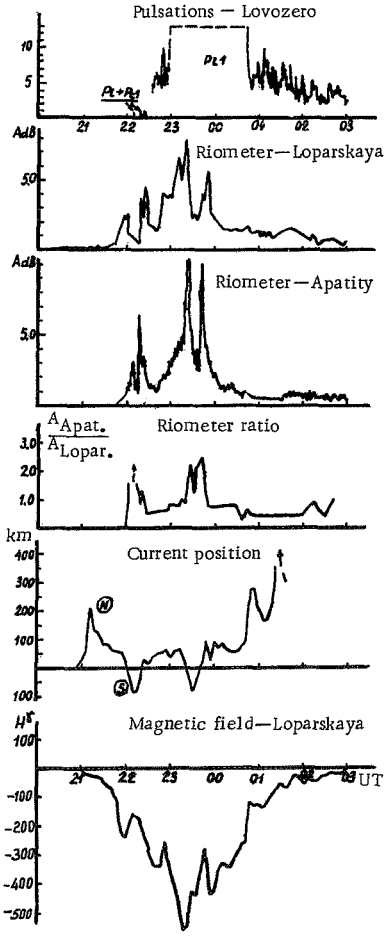

FIGURE 2. The time curve of the midnight electron injection according to /10/.

In the evening (20 — 24 LT), the showers are mostly quiet and structureless, covering an area with a characteristic dimension of D~200 km; the spectrum is at its hardest (E_0~30 — 50 keV)* /15, 19, 20/. On the other hand, satellite measurements /21/ indicate that the electron spectrum early in the evening is softer than at any other time. A similar conclusion emerges from auroral observations /22/; the polar aurorae occur in a homogeneous wide arc in the evening. Pudovkin /22/ attributes this discrepancy in results to the lack of excess X-ray radiation in the stratosphere during the relevant time interval. The measurements thus only give a weak background of hard electrons, which are detectable during the day irrespective of the disturbance level. This conclusion does not follow from the observations of particle fluxes in the stratosphere. Therefore, the most plausible assumption is that two independent fluxes of soft and hard electrons exist, and the different measurement methods respond to a limited spectrum range only. Moreover, the soft electrons may penetrate farther north than the hard electrons.

After the breakup of the polar aurorae, a new phase of particle penetration begins. The electron flux may increase by two orders of magnitude in about 10 msec /8/. As a rule, several bursts with duration from 20 msec /8, 13/ to several tens of minutes are observed. The dimensions of the injection regions are related to

* An exponential spectrum is generally assumed for the auroral electrons, $N(>E) = N_0 \exp(-E/E_0)$.

the burst duration: the shorter the burst, the more localized it is /10/. The instantaneous electron fluxes in these cases are larger than during any other time of the day; the flux of electrons with $E \geq 30$ keV may reach $5 \cdot 10^8$ $cm^{-2} sec^{-1}$ /23/. It is difficult to speak of regularities in the variation of the electron spectrum in this period, since the measurement data are often quite contradictory. The electron spectrum becomes markedly softer during the breakup /9/ or soon after /19/, hard and soft bursts may alternate, soft and hard electron fluxes may be observed simultaneously /19, 15/ and independently /24, 25/. It is hoped that careful analysis of the electron penetration regions during the bursts will shed some light on this problem. Indeed, the electron penetration regions in these cases are small and rapidly moving. Figure 2 shows that the brief electron bursts are injected to the south of the general penetration region; this is evident from the position of the ionospheric currents and from the ratio of the near riometers /10/. Moreover, a latitude separation of particles according to energies is observed, the soft electrons penetrating nearer the pole /26, 9, 27/. The measurement results thus significantly depend on whether the recorder is located in the northern or the southern part of the penetration region.

Breakup injections change into more prolonged injections, which are clearly associated with negative bay disturbances in the H-component of the magnetic field /28/. The corresponding electron spectrum is very soft ($E_0 \sim 10 - 15$ keV), and a satisfactory correlation is observed between the stratospheric X rays and polar aurorae /26, 29/ and Pi-1 micropulsations /10, 30, 31, 32/. In these cases, a latitude separation of particles of various energies is also possible.

SLOWLY VARYING ABSORPTION

In morning hours (06 — 13 LT), riometric and stratospheric data clearly bring out a special type of auroral particle injection, variously known in the literature as Brown-type absorption, slowly varying absorption (SVIA or SVA), or extended morning injections /14, 20, 22, 28, 34/.

The time curve of particle injection (consisting mainly or totally of electrons) is characterized by a rapid growth of intensity (20 — 30 min) and a slow quasi-exponential decrease, which takes 1 — 5 hrs. SVA is characterized by total absence of local geomagnetic disturbances, although a substorm is observed on the midnight meridian at the same time (particle injection, negative bays); the SVA onset lags 1 — 10 min /34/ or 20 — 30 min /33, 56/ relative to the breakup time.

Measurements of the X-ray energy spectrum in the stratosphere /15/ and energy estimates from riometric and photometric data /22/ indicate that the electron spectrum during the SVA is harder than at night during breakup or during negative bays; ground measurements give mean electron energies between 40 and 100 keV /22/, and E_0 according to stratospheric data varies between 15 and 40 keV /34, 19/.

Stratospheric measurements, and especially coordinated flights of several balloon probes launched at different latitudes and longitudes /37/, elucidated a number of new characteristics of SVA. In particular, it was

established that the penetration of electrons occurs simultaneously at points separated at least by as much as several hundred kilometers along the same geomagnetic parallel; the penetration begins to the north of L = 6.5, and then the equatorial boundary of the penetration region moves south with a velocity of some 500 m/sec, retaining its original orientation (Figure 3). The southward motion was observed down to L = 4.5. The decrease in the intensity of the penetrating electrons occurs synchronously over the entire area and begins during the phase of the southward motion.

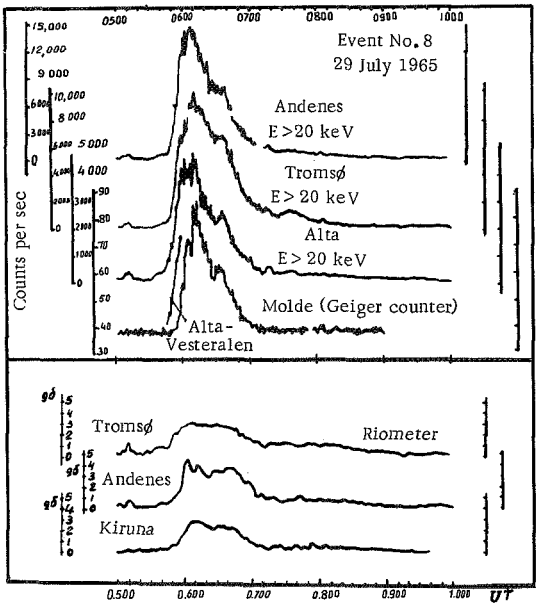

FIGURE 3. SVA curves from flights in Scandinavia.

The X-ray spectrum grows softer during the upward phase of the SVA intensity, and after that the energy increases /37, 19/; the softer spectrum is probably due to the approach of the penetration front to the balloon; the nearer the penetration region to the balloon, the smaller is the relative absorption of the low-energy photons in air. Comparison of the nighttime and daytime SVA shows that this absorption is due to electrons. Some authors, however, point to the possible injection of protons /34/, in particular in the last stage of SVA.

SLOW VARIATIONS (SV)

Slow variations of the electron flux with a period of 300 – 500 sec are often observed during the SVA. The dimensions of the region encompassed by the slow variation are comparable to the SVA dimensions: 200 – 500 km

in latitude and over 1000 km in longitude /38/. There are reports of synchronous variation across the entire injection region /38/ and of a fast motion of the wave from east to west with velocities of 2 — 2.5 km/sec /39/. The electron spectrum during a slow variation is apparently no different from the general background /19, 38/, although random changes in the spectrum were observed /40, 41/: in particular, the maximum was seen to grow softer /41/. The large spectral range of the slow variations is borne out by the cases of synchronous variation of X rays, polar aurorae, and riometer absorption /19, 34, 37/. A magnetic field variation (giant pulsations) /42, 43/ is often observed during the slow variation, both being of approximately the same period.

The slow variation in all probability is related to the modulation of the penetrating electron stream by magnetohydrodynamic waves /42/. The possible association of the slow variations with the variable electrical field produced in the ionosphere as a result of the gravitational oscillations of the air column was also considered /44/. Another important fact is that variations of the electron flux with a period of 100 — 200 sec are also observed in the plasma layer of the magnetosphere tail /45/. Variations of electrons with a period of 300 — 1000 sec were discovered by Lin and Anderson /46/ in the skirt, and the maximum of the observed cases falls in morning hours /46/.

FAST VARIATIONS (FV)

Starting with the breakup and up to the afternoon hours, fast variations with a period of 5 — 30 sec are sometimes superimposed on the smooth variations of the flux of auroral electrons. We should apparently distinguish between two types of FV — the faster type with a period of 5 — 20 sec, which are observed in early morning hours (02 — 10 LT) and the daytime type, which are observed around noon (10 — 15 LT), with a period of 20 — 30 sec /8/. The first type of FV has been studied in greater detail, and we will therefore mainly consider the characteristics of this type.

FV are generally observed against the background of the previously considered slower types of penetrations. They produce a modulation of the main flux, which is more like a pulse modulation than a sinusoidal modulation. The period may prove to be quite stable in a number of cases /8, 47/, bu mostly no distinct period is observed; the period of the daytime FV tends to decrease /37/.

The region corresponding to FV is significantly smaller than the region of the basic slow variations: it occupies 100 — 150 km for both the morning and the daytime types. In a number of cases this region may be larger. Thus, comparison of the data obtained at an altitude of 2350 km and with a radiosonde reveals a certain correlation of pulsations over a distance of up to 400 km in the east — west direction ($\Delta L \sim 0.9$) /48/. Not all the electron penetrations are subjected to FV, and the onset or disappearance of FV is often associated with alternation of the fundamental slow bursts (Figure 4). Measurements of the X-ray spectrum show that the electron flux is somewhat harder at the maximum (by 2 keV) /8/; in other words, the modulation coefficient increases with the increase in energy (from

1.7 to 40 keV to 2.3 — 2.4 for E > 80 keV /49/). The spectrum during the growth phase is harder than during the downward phase of the intensity curve /49/ (Figure 5).

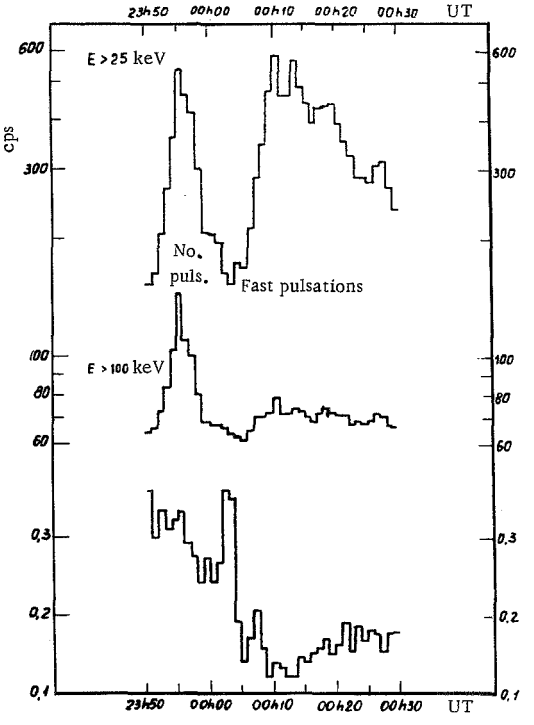

FIGURE 4. Appearance of fast variations with simultaneous change in the energy of the main electron penetrations.

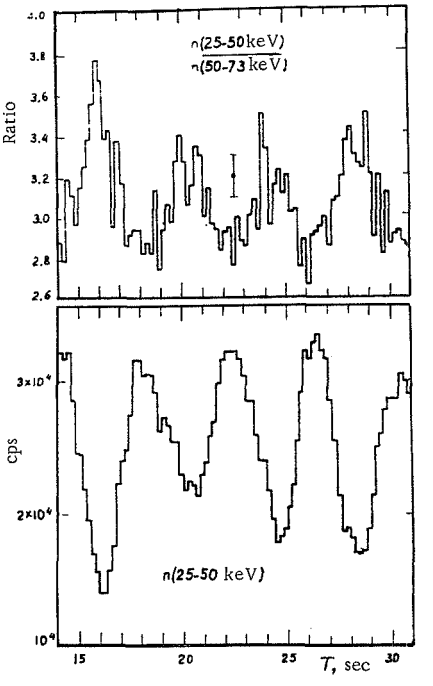

FIGURE 5. The spectrum of fast pulsations.

In some cases, FV have been observed during the spectrum of preferentially slow electrons /50/. The harder electron spectrum at the maximum indicates that this phenomenon cannot be attributed to the passage of inhomogeneous penetration regions above the radiosonde, since in this case a softer spectrum should have been observed /37/. Pulsations of similar periods are often observed in numerous geophysical effects associated with electron penetration. Pulsations with periods of 5 — 15 sec were observed in the auroral absorption of radio noise from space /37/; in the polar aurorae in morning hours /51 — 54/, the pulsations are generally associated with diffuse spots. Finally, Pi-1 pulsations are observed in the magnetic field at night and in morning hours, and in daytime the FV are accompanied by Pc-3 pulsations /31/.

Comparison of the various pulsation phenomena reveals a strict relationship between them. As a rule, the occurrence times coincide and there is no close correlation in the periods of the variations, although in certain cases the correlation is relatively close. Rosenberg et al. /55, 56/

launched a photometer on the same radiosonde, and since the angular characteristics of the detectors also coincided, closely correlated events were observed. Note that the emission in the 5577 Å line lagged behind the fast variation by approximately 1 sec for $\tau \sim 10$ sec, which may be interpreted as a result of relative nearness of the source of variations $(1-2\ R_E)$.

MICROBURSTS

Microbursts are generally observed against the background of quiet injection during the daytime hours, between 4 and 17.30 LT /57/; before noon, they are twice as frequent as in the afternoon hours, showing a central peak at 8.30 LT. The duration of microbursts is from a few minutes to 5 hrs; on the average, a single event comprises 10^3 individual bursts; two groups are generally observed daily for a few days after a magnetic storm. The characteristic duration of microbursts is about 0.2 sec, the recurrence period is about 0.6 sec, and the time between successive groups of bursts is about 10 sec /58/. The morning bursts are asymmetrical: they are described by the expression $1-\exp(-t/\tau_R)$, where $\tau_R \sim 30$ msec, and the downward phase is described by $\exp(-t/\tau_D)$, $\tau_D \sim 200$ msec. Later, after 9.30 LT, the bursts become symmetrical /59/. These symmetrical bursts are the most frequent ones (Figure 6).*

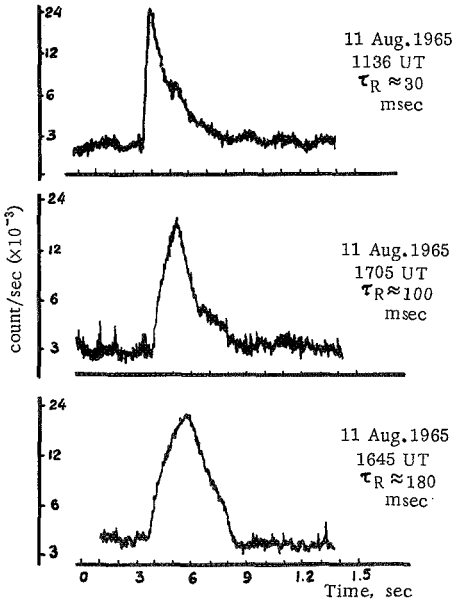

FIGURE 6. Three types of microbursts.

A characteristic particle flux at the maximum is 400—2000 $cm^{-2}sec^{-1}sterad^{-1}$ for $E > 30$ keV /58/; for $E > 60$ keV, the maximum flux is about 100 $cm^{-2}sec^{-1}$ /59/, or 0.2—15 $cm^{-2}sec^{-1}sterad^{-1}keV^{-1}$ /57/. Satellite measurements gave a flux of $3 \cdot 10^{-5}$ $cm^{-2}sec^{-1}sterad^{-1}$ for electrons with $E > 40$ keV, which corresponds to 20 $cm^{-2}sec^{-1}$ /60/. The observations exceeded the background readings by a factor of 20 /12/. Microbursts are observed in the auroral zone, more frequently at L = 6 than at L = 8 /57/, in strips elongated in the north—south direction which drift to the east with a velocity of 250—300 m/sec /58/. During 5% of the total time of observations, microbursts with velocities of up to 10—100 km/sec were observed. Comparison of satellite and balloon data shows that the region of simultaneous

* Very short bursts of 5—25 msec duration were occasionally observed /12/.

penetration extends over 400 km along the parallel and 250 km along the meridian /48, 60/ at L = 6 – 8.5. According to other data, the microburst region is smaller, as small as 40 km, or even 20 km /58/. The microburst spectrum coincides with the background spectrum; E_0 = = 20 – 25 keV /41, 57/, but according to other data the spectrum grows softer during the burst /58/. Rocket measurements record microburst electrons with E ~ 80 – 160 keV and 160 – 320 keV, and there are no electrons recorded between 5 and 20 keV (Figure 7).

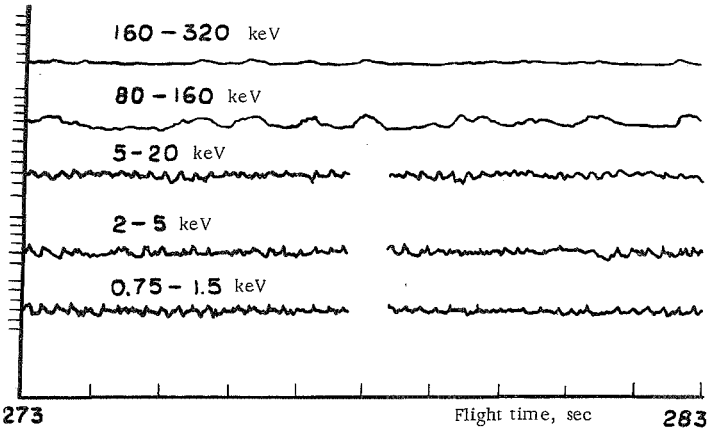

FIGURE 7. Spectral characteristics of microbursts according to rocket measurements.

Satellite observations of microbursts /60/ show that the flux of injected electrons (180°) during a microburst increases at double the rate characteristic of the trapped electrons (90°) (the background behaves in an exactly opposite manner), which does not correspond to the classical cases of penetration, when the fluxes are isotropic. Daytime rocket measurements /62/ revealed a 10-fold increase of the flux in 3 msec (the fastest variation so far recorded), and the high-energy particles preceded the soft particles (60 – 90 and 90 – 150 keV) by 0.01±0.01 sec, or by 0.1 – 0.26 sec in other cases; these figures give for the position of the sources distances ranging between 2.5 and 22 R_E. According to other data /59/, there is no dispersion (< 10 msec), which is either an indication of the nearness of the source or points to a significant interaction between the particles and also between the particles and the field.

In addition to the relation of microbursts to magnetic storms, there is a certain relation of the microbursts to magnetic pulses /30/ in a narrow time interval (11 – 13 LT) and to Pi-1 pulsations; the recurrence period of the microburst groups (10 sec) coincides with the periods of polar aurorae, discussed before.

DAYTIME MINUTE BURSTS (DMB)

Hard X-ray (electron) bursts with a duration of up to several minutes are observed in daytime /64/ (Figure 8). The extent of the DMB region in space is less than 230 km (one measurement /65/).

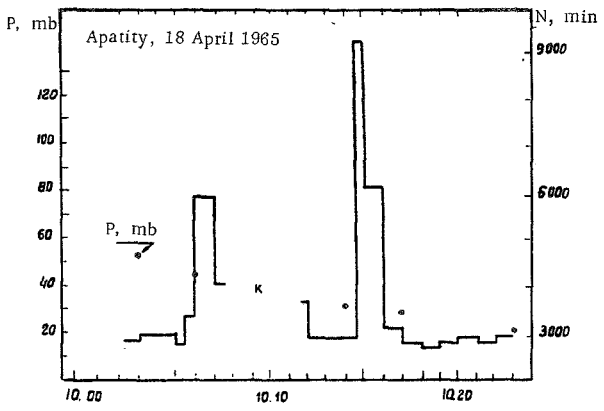

FIGURE 8. Daytime minute bursts.

According to our data /64/, DMB are observed in geomagnetically active periods, but they do not coincide with particular magnetic field or riometer disturbances. A case of DMB during a sudden impulse was described in /37/; the photon spectrum during the DMB (11.06 UT) was harder than before and after Si. According to spectral characteristics and time properties, daytime variations with a period of 95 — 110 sec are close to DMB /66/.

ROCKET MEASUREMENTS

Rocket measurements yield valuable information about the energy distribution of the injected particles in a wide range of energies, about the angular distribution, the composition of particles (in particular, the composition of the auroral protons), and some data about fast flux variations. Rocket measurements are so far fairly isolated and do not lead to any general conclusions in view of the tremendous variety of the space, time, and energy characteristics of the auroral radiation.

Spectrum measurements

Stratospheric measurements give an electron spectrum of the form $I = I_0 \exp(E/E_0)$, where E_0 varies from n to n · 10 keV. Rocket measurements show, however, that this is not always so. In some cases, the spectrum is softer and almost monoenergetic /67 — 69/. Thus a monoenergetic spectrum with $E \simeq 6$ keV with a rapid drop in the high-energy region with $E_0 < 100$ eV was measured at 5577° Å /67/ (Figure 9). Soft spectra with $E_0 \simeq 4$ keV and 8 keV were measured /70/ in IBC-1 and IBC-2 emission. The variation of the (soft) electron flux was substantially

less than the variation of the auroral intensity. A soft non-monoenergetic spectrum consisting of several independent fluxes was measured by Reidy et al. /69/. In general, the fluxes of high-energy electrons cannot be regarded as a "tail" of the soft spectrum; some measurements /24, 71/ point to the possible existence of a second maximum (E ~400 keV), and in other cases the fluctuations in the high-energy region are much larger than in the low-energy region (the electron flux between 80 and 160 keV increased by two orders of magnitude in 50 sec, whereas between 5 and 20 keV it increased by one order of magnitude and between 2 and 5 keV the flux did not change /61/). According to measurements /13/, the maximum variation is observed for energies above 45 keV; for E> 100 keV the variation is smaller, but on the other hand the electron spectrum becomes softer during stable injections /24/. In one measurement, a steady growth of the electron energy from 10 to 15 keV was observed; it was due to the rocket having traveled 100 km in the southward direction (there is a latitude separation of the electrons according to energies /27, 33/, associated with local accelerations toward the pole in the field of about 55 mV/m).

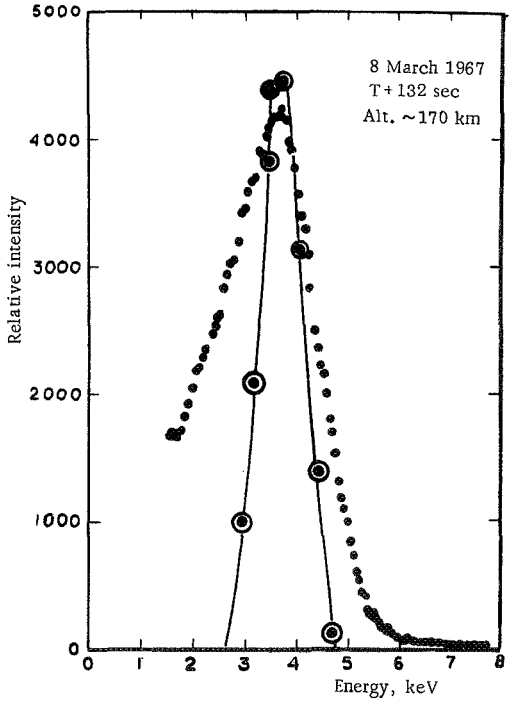

FIGURE 9. Monoenergetic spectrum of injected electrons measured from a rocket. The solid curve is the detector calibration.

Rocket measurements also permitted estimating the fluxes of electrons with energies below 1 keV. The measurements show that the electron spectrum extends beyond the 100 eV energy range, and the flux of these electrons is too high to be regarded as a flux of secondary particles; it may be accounted for by the local acceleration of particles in an electric

field directed along the magnetic lines of force /72, 73/. The same explanation applies to the residual upward electron flux, measured in /74, 75/.

We should stress one characteristic feature of the angular distribution of the particles: the electron flux in the undisturbed case is anisotropic, with a maximum at 90° to the line of force, whereas during penetration the flux is isotropized /24, 61, 74, 76/. The above-described cases of upward electron fluxes (> 40 keV) with intensities increasing the theoretical prediction constitute a deviation from this rule (they are observed for weak fluxes only; no such anomalies occur during high intensity penetrations). The explanation of this effect is to be sought in the modification of the pitch-angle distribution of the electrons by the ionospheric electric field /76/. In case of fast variations, the fluctuations in the loss cone may be one order of magnitude deeper than in a trapped flux /12/.

Measurements of the diurnal variation

Rocket measurements of the diurnal variation and of other statistical characteristics are less reliable than the stratospheric measurements, since the conclusions are based on isolated measurements. On the whole, the results are consistent with stratospheric data. They reveal, first, a greater variation of the spectrum and a higher average intensity of the electron flux at night than in daytime ($1.6 \cdot 10^8$ $cm^{-2} sec^{-1} sterad^{-1} keV^{-1}$ and $6 \cdot 10^7$ $cm^2 sec^{-1} sterad^{-1} keV^{-1}$ for E = 2 keV) /61/ and, second, a harder spectrum in daytime on the average.

Space and time characteristics

Rocket measurements of the space and time characteristics of the electron flux on the whole bear out the stratospheric measurements of the fast variations of the electron flux, as described before. Considerable importance is attached to measurements of small spatial inhomogeneities D~30 m, which are observed from rockets /13, 24/, and time inhomogeneities (of the order of 1 msec); in particular, the existence of a time delay for electrons of various energies should be established. The results of the isolated measurements are still contradictory: in some cases the delay is observed /77/, while in others not /13/.

Rocket measurements of protons corroborate the results of indirect (ground-based) measurements indicating that the proton flux is one order of magnitude less than the electron flux /24, 78, 79/ and is constant in time /13/. The anticorrelation of protons and electrons during injection is particularly interesting /71/; as the electron flux increases and the angular distribution of electrons develops from anisotropic to isotropic, the flux of protons with E> 65 keV changes from isotropic to anisotropic with a maximum at 90° (a reduction by a factor of 5 in the loss cone) and the ascending proton flux exceeds the descending flux. The possible reason for this effect is to be sought in the existence of a local electric longitudinal field. The flux of alpha particles in auroral flow is even

smaller. The fluxes of electrons, protons, and alpha particles are 10^6, $1.4 \cdot 10^5$, and $2.6 \cdot 10^4$ particles/cm^{2}sec · sterad for energies greater than 20, 50, and 50 keV, respectively /79/.

CONCLUSION

The various characteristics of the auroral particles injected into the atmosphere present a fertile ground for the development and the verification of the mechanisms of particle acceleration and motion in the magnetosphere. This problem falls beyond the scope of our review, and we will only make a few general remarks on the subject.

Figure 10 shows a simplified block diagram of the history of auroral particles. It starts with an acceleration mechanism (or several acceleration mechanisms); the accelerated particles either penetrate directly into the Earth's atmosphere or experience certain additional interactions — drift motion, modulation by magnetohydrodynamic or plasma waves, etc. There is a further possibility of the accelerated particles becoming trapped in the radiation belt and later being injected into the atmosphere. Each of the possible acceleration—interaction—injection chains should correspond to a definite type of penetration, and vice versa. If a certain type of injection repeats itself in different cases, we conclude that these cases were characterized by the corresponding mechanisms of acceleration and additional interaction. The different penetration types thus provide the elementary cells from which the overall picture of the phenomenon can be constructed.

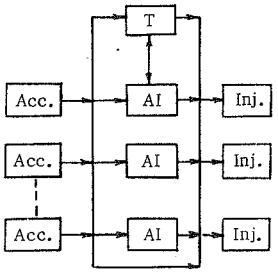

FIGURE 10. A block diagram illustrating the history of auroral particles (acceleration, additional interaction, trapping, injection).

Let us consider the existing models of the penetration zones of auroral particles. Figure 11 schematically shows some of the leading models: a) Khorosheva and Feldstein's zone /2, 17, 18/, b) two penetration zones according to Mishin /80/, c) the currently most popular penetration scheme of Hartz and Brice /81/. The various characteristics of the different penetration types considered above can be reduced to two groups. However, the models of particle penetration hardly improve our understanding of the processes which take place in the magnetosphere during disturbances. Indeed, this approach lumps different types of additional interactions and possibly even different acceleration mechanisms in a single ring zone. It is essential to consider separately the zones corresponding to each known type of particle penetration and also to examine the dynamic behavior of the entire process, e.g., during the development of a substorm. The dynamic approach has recently been worked on by Akasofu /82/; he also published a detailed analysis of the development of a substorm, but unfortunately his starting point was instrumental (a substorm in the X-ray spectrum, a substorm in riometric absorption, etc.), and no classification according to different types of penetration was attempted.

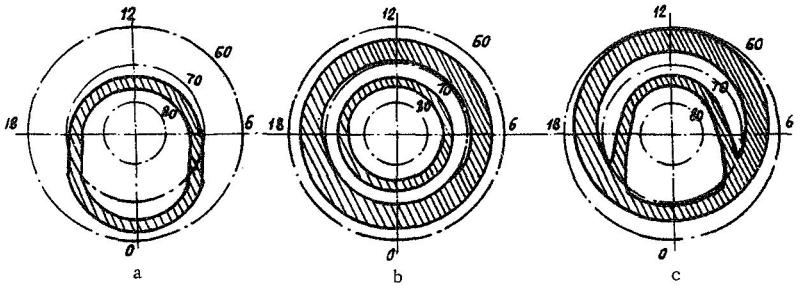

FIGURE 11. Penetration zones of auroral electrons:

a) according to Khorosheva and Feldstein /2,17/; b) according to Mishin and Saifudinova /80/; c) according to Hartz and Brice /81/.

We tried to classify the different penetrations of auroral particles into the Earth's atmosphere at high latitudes. In view of the great diversity and complexity of the phenomenon, the author tried to confine himself to sufficiently reliable experimental data. For this reason, many of the previously mentioned characteristics, which are based on individual measurements, were ignored, the important topic of the possible relation of the penetrating particles to auroral and trapped radiation in the Earth's magnetosphere was not considered, theoretical problems were not discussed. Limitations of space rule out a detailed discussion of the characteristics of auroral protons, auroral particles inside the polar cap, the dynamics of penetration during a substorm. These problems may constitute the subject of a separate paper.

I would like to acknowledge the help of my colleagues at the Cosmic-Ray Laboratory in the course of this project.

Bibliography

1. Isaev, S.I. Morfologiya polyarnykh siyanii (Morphology of Polar Aurorae).— Leningrad, Izdatel'stvo "Nauka." 1968.
2. Khorosheva, O.V.— In: "Polyarnye siyaniya," No.16. Moskva, Izdatel'stvo "Nauka." 1967.
3. Driatskii, V.M.— Geomagnetizm i Aeronomiya, No.6:1061. 1966.
4. Hiltquist, B.— Planet. Space Sci., 8:142. 1961.
5. Ivanov-Kholodnyi, G.S.— In: "Fizika magnitosfery i polyarnye buri," p.171. Irkutsk, Izd. SO Izmiran. 1968.
6. O'Brien, B.J.— Review Presented at the IQSY/COSPAR Symposium. London, England. July, 1967.
7. Kuz'min, I.A. Present Collection, Part 2, p. 139.
8. Parks, G.K., F.V. Coroniti, R.L. Pherron, and K.A. Anderson.— J. Geophys. Res., **73**(5):1685. 1968.
9. Pilkington, G.R., C.D. Anger, and T.A. Clark.— Planet. Space Sci., **16**(6):1685. 1968.
10. Kuz'min, I.A., L.L. Lazutin, G.A. Loginov, M.I. Pudovkin, A.N. Charakhch'yan, and T.N.Charakhch'yan.

In: "Polyarnye siyaniya," No. 17, p. 98. Moskva, Izdatel'stvo "Nauka." 1968.
11. Lomonosov, M.V. Sochineniya (Collected Works), Vol. 3.— Moskva-Leningrad, Izdatel'stvo AN SSSR. 1952.
12. Parks, G.K., D.W. Milton, and K.A. Anderson.— J. Geophys. Res., 72(17):4587. 1967.
13. Mozer, F.S.— J. Geophys. Res., 73(3):999. 1968.
14. Ansari, Z.A.— J. Geophys. Res., 69(21):4493. 1964.
15. Bewersdorf, A., J. Dion, J.P. Legrand, E. Keppler, G. Kremser, and W. Riedler.— Space Res., 7/1:645. 1967.
16. Lazutin, L.L.— Trudy Alma-Atinskoi konferentsii po kosmicheskim lucham. 1966. (In press).
17. Feldstein, Y.I. and G.V. Starkov.—Planet. Space Sci., 15:209. 1967.
18. Starkov, G.V. and Ya.I. Fel'dshtein.— In: "Polyarnye siyaniya," No. 17:22. Moskva, Izdatel'stvo "Nauka." 1968.
19. Barcus, J.R. and T.J. Rosenberg.— J. Geophys. Res., 71(3):803. 1966.
20. Kremser, G. From Aurora and Airglow, p. 477. Chicago. 1967.
21. Fritz, T.A.— Trans. AGU, 47(1):130. 1966.
22. Pudovkin, M.I. Polyarnye magnitnye buri (Polar Magnetic Storms).— Leningrad, Izdatel'stvo "Nauka." (In press).
23. Barcus, J.R.— J. Geophys. Res., 70(5):1237. 1965.
24. Mozer, F.S. and P. Bruston.— J. Geophys. Res., 71(19):4451. 1966.
25. Reidy, W.P., E.R. Hegblom, and J.C. Ulwick.— J. Geophys. Res., 73(9):3072. 1968.
26. Lazutin, L.L. and V.K. Poldutin.— Izvestiya AN SSSR, Seriya Fizicheskaya, 30(11):1804. 1966.
27. Albert, R.D.— J. Geophys. Res., 72(23):5811. 1967.
28. Kremser, G. From "Introduction to Solar-Terrestrial Relations," p. 415. Holland. 1965.
29. Vinkler, D.P.— In: "Radiatsionnye poyasa i geofizicheskie yavleniya," p. 15. Moskva, Izdatel'stvo "Nauka." 1963.
30. Milton, D.W., R.L. McPherron, K.A. Anderson, and S.H. Ward.— J. Geophys. Res., 72(1):414. 1967.
31. McPherron, R.L., G.K. Parks, F.V. Coroniti, and S.H. Ward.— J. Geophys. Res., 73(5):1697. 1968.
32. Wilhelm, K.— J. Geophys. Res., 72(7):1995. 1967.
33. Albert, R.D.— Phys. Rev. Lett., 18(10):369. 1967.
34. Bewersdorf, A., G. Kremser, W. Riedler, and J.P. Legrand.— Arkiv. geophys., 5(2):115. 1967.
35. Pudovkin, M.I., O.I. Shumilov, and S.A. Zaitzeva.— Planet. Space Sci., 16:881. 1968.
36. Pudovkin, M.I. and O.I. Shumilov.— Uchenye Zapiski LGU, Voprosy Geofiziki, No. 17:241. 1967.
37. Bewersdorf, A., G. Kremser, J. Stadness, H. Trefall, and S. Ullaland.-- J. Atmos. Terr. Phys., 30(4):591. 1967.
38. Barcus, J.R. and T.J. Rosenberg.— J. Geophys. Res., 70(7):1707. 1965.
39. Brönstad, K. and H. Trefall.— J. Atmos. Terr. Phys., 30(2):205. 1968.
40. Trefall, H. and K. Bärdsen.— J. Geophys. Res., 68:4909. 1963.

41. Hudson, H.S.— Trans. AGU, 47(3):462. 1966.
42. Anger, C.D., J.R. Barcus, R.R. Brown, and D.S. Evans.— J. Geophys. Res., 68:3706. 1963.
43. Ullaland, S.L., H. Trefall, G. Kremser, and A. Bewersdorf.— J. Atmos. Terr. Phys., 29(4):395. 1967.
44. Parthasarathy, R. and V.P. Hessler.— J. Geophys. Res., 69:2867. 1964.
45. Bame, S.J., J.R. Asbridge, H.E. Felthauser, E.W. Hokes, and I.B. Strong.— J. Geophys. Res., 72(1):113. 1967.
46. Lin, R.P. and K.A. Anderson.— J. Geophys. Res., 71(7):1827. 1966.
47. Brown, R.R. and R.A. Weir.— J. Atmos. Terr. Phys., 29(12): 1611. 1967.
48. Milton, D.W. and M.N. Oliven.— J. Geophys. Res., 72(21):5357. 1967.
49. Brown, R.R. and R.A. Weir.— J. Geophys. Res., 72(21):5531. 1967.
50. Kangas, J.— Ann. Geophys., 24(1):147. 1968.
51. Campbell, W.H. and K. Matsuchita.— J. Geophys. Res., 67:555. 1964.
52. Poldugin, V.K.— Geomagnetizm i Aeronomiya, 7(3):74. 1967.
53. Pinter, S.— Informatsionnyi Byulleten' Sovetskoi Antarkticheskoi Ekspeditsii, No. 61:74. 1967.
54. Paulson, K.V. and G.G. Shepherd.— Canad. J. Phys., 44(4): 837. 1966.
55. Rosenberg, T.J., J. Bjordal, and G.J. Kvifte.— J. Geophys. Res., 72(13):3504. 1967.
56. Barcus, J.R.— J. Geophys. Res., 70(9):2135. 1965.
57. Anderson, K.A., L.M. Chase, H.S. Hudson, M. Lampton, D.W. Milton, and G.K. Parks.— J. Geophys. Res., 71(19):4617. 1966.
58. Parks, G.K.— J. Geophys. Res., 72(1):217. 1967.
59. Venkatesan, D., M.N. Oliven, P.J. Edwards, and K.G. McCracken.— J. Geophys. Res., 73(7):2333. 1968.
60. Oliven, M.N., D. Venkatesan, and K.G. McCracken.— J. Geophys. Res., 73(7):2345. 1968.
61. Chase, L.M.— J. Geophys. Res., 73(11):3469. 1968.
62. Lampton, M.— J. Geophys. Res., 72(3):8817. 1967.
63. Oliven, M.N. and D.A. Gurnett.— J. Geophys. Res., 73(7): 2355. 1968.
64. Lazutin, L.L.— In: "Kompleksnye issledovaniya polyarnoi ionosfery," Moskva, Izdatel'stvo "Nauka." 1969. (In press).
65. Fewersdorf, A., J. Dion, G. Kremser, E. Keppler, J.R. Legrand, and W. Riedler.— Ann. Geophys., 22(1):23. 1966.
66. Evans, D.S.— J. Geophys. Res., 68:1805. 1963.
67. Evans, D.S.— J. Geophys. Res., 72(17):4281. 1967.
68. Evans, D.S.— J. Geophys. Res., 73(7):2315. 1968.
69. Reidt, W.P., E.R. Hegblom, and J.G. Ulwick.— J. Geophys. Res., 73(9):3072. 1968.
70. Ulwick, J.C., W.P. Reidy, and K.D. Baker.— Space Res., 7/1:656. 1967.

71. Mozer, F.S. and P. Bruston.— J. Geophys. Res., 71(19): 4461. 1966.
72. Mathews, D.L. and T.A. Clark.— Canad. J. Phys., 46(3):201. 1968.
73. Ogilvie, K.W.— J. Geophys. Res., 73:2325. 1968.
74. McDiarmid, I.B., E.E. Budzinski, B.A. Whalen, and N. Sikopke.— Canad. J. Phys., 45(5):1755. 1967.
75. McDiarmid, I.B. and E.E. Budzinski.— Canad. J. Phys., 46(8):911. 1968.
76. Cummings, W.D., R.E. LaQuey, and B.J. O'Brien.— J. Geophys. Res., 71(5):1399. 1966.
77. Bryant, D.A., H.L. Collin, G.M. Courtier, and A.D. Johnstone.— Nature, 215(5096):45. 1967.
78. Whalen, B.A., I.B. McDiarmid, and E.E. Budzinski.— Canad. J. Phys., 45(10):3247. 1967.
79. Whalen, B.A. and I.B. McDiarmid.— J. Geophys. Res., 73(7):2307. 1968.
80. Mishin, V.M. and T.I. Saifudinova (Vershinina).— In: "Fizika magnitosfery i polyarnye buri," p. 355. Irkutsk, Izd. SO IZMIRAN. 1968.
81. Hartz, T.R. and N.M. Brice.— Planet. Space Sci., 15:301. 1967.
82. Akasofu, S.I. Polar and Magnetospheric Substorms.— D. Reindel Publ. Co., Dordrecht, Holland. 1968.

MAGNETOSPHERIC ELECTRIC FIELDS AND THE ROTATION OF THE EARTH

B. E. Bryunelli

We have previously mentioned one fundamental difficulty associated with the analysis of the electric field in the magnetosphere, namely that the field geometry emerging from our current concepts regarding the nature of the magnetospheric processes is incompatible with the results of the analysis of geomagnetic disturbances /1, 2/. Indeed, the penetration of charged particles into the Earth's atmosphere entails an influx of matter to the Earth. The motion of plasma to the Earth in the central parts of the magnetosphere tail is also part of the convection scheme proposed by Axford and Hines /3/; to ensure this Earthward motion, the electric field in the magnetosphere should have a high potential on the day side. On the other hand, a polar magnetic disturbance is characterized by one or two current streams flowing along the auroral zone in the westward direction above the morning and the night sectors and in the eastward direction above the day and the evening sectors. Both streams transport positive charges to the evening side of the Earth, and if the motivating force of the current system is localized in these streams, their existence should produce a field with a positive potential on the evening side of the Earth, i. e., the opposite of what emerges from Axford and Hines' convection scheme. I have tried /1, 2/ to treat the magnetospheric field (with a positive potential on the morning side) as the starting point and derive the current systems of the polar magnetic disturbance as a result of the magnetospheric field closing through the ionosphere.

A number of recent reports contain data which bear out or are at least consistent with the assumption of an electric field in the magnetosphere which has a high potential on the morning side. Freeman /4/ observed the motion of low-energy plasma in the magnetosphere which was consistent with Axford and Hines' scheme /3/. It was confirmed /5/ that the electron energy on the morning side of the magnetosphere tail is higher than that on the evening side. Vasyliunas /6/, equating the effect of convection and the Earth's rotation at the surface of the plasmosphere, estimated the strength of the magnetospheric field and derived the following expression (after inserting the numerical values of the constants):

$$E = 0.4\left(1 + \frac{K_p}{5}\right) \text{ V/km.} \qquad (1)$$

Piddington /7/ studied the effects of the asymmetry of the radiation belt, associated with the injection of fresh particles on the night side only.

He showed that the resulting electric field is opposed to the magnetospheric field and should make the plasma drift to the Earth.

The uncertainty regarding the electric field in the magnetosphere motivated a new research program at the Soviet Polar Geophysical Institute. The starting premise of this program was the assumption, advanced by V.B. Lyatskii, that the processes linked with the rotation of the Earth play a leading role in these phenomena. The following chain of effects can be reconstructed as possibly leading to generation of a large-scale electric field.

In the high latitudes, there are several regions where the geophysical effects display certain peculiar features. Thus, there is a zone of maximum recurrence frequency of the polar aurorae (the auroral zone, or the Fritz zone /8/), which corresponds roughtly to geomagnetic latitude 65°. Nikol'skii /9/ pointed to the possible existence of a second, inner auroral zone at geomagnetic latitude of about 75°, where the activity increases in daytime. Khorosheva /10/ and Feldstein /11/ introduced the concept of an instantaneous auroral zone, which is tangent to the Fritz zone on the night side and to the inner zone on the day side. Aurorae occur only along a certain oval, and the diurnal rotation of this oval is responsible for the inner and the outer zone acting as two envelopes. The oval is positioned at the site of injection of high-energy electrons /12/, and this led to the assumption that the oval represents a separating line between the lines of force which close through the parts of the magnetosphere near the Earth and the lines of force trailing off into the tail. In /13/ an enhancement of geomagnetic activity was detected on the day side of the Earth, which is associated with the formation of neutral points in the magnetosphere, with the solar wind blowing past these points. According to the calculations of Mead /14/ and Taylor and Hones /15/, the lines of force crossing the equatorial plane near the magnetospheric boundary enter the Earth at a latitude corresponding to a neutral point. It therefore seems that the geometry of the lines of force in the magnetosphere corresponds to that shown in Figure 1: lines of force forming the boundary of the magnetosphere emerge from the geomagnetic parallel corresponding to the inner auroral zone; they close both through the equatorial plane near the Earth and through the tail, which they reach along the outer part of the magnetopause. The daytime section of the inner zone corresponds to a neutral line on the surface of the magnetosphere. The lines of force emerging on the night side of this zone trail off into the tail, dividing it into parts filled with field lines emerging from the polar cap and from the region lying between the inner zone and the oval. We will refer to the latter region as the auroral region. The magnetic flux from these regions is approximately $6 \cdot 10^{16}$ and $3 \cdot 10^{6}$ maxwell, respectively. It is generally assumed that the north and the south halves of the tail are separated by a neutral layer, whose field (of the order of 1 gamma) is perpendicular to the interface /16/. At large distances from the Earth, a more complex picture is observed, the perpendicular field component often reverses its sign, but since on the whole the field was found to diminish /16/, we will take this component to point northward on the average (with the same magnitude as above). The existence of this perpendicular component should lead to a steady decrease of the magnetic flux in the tail, and it seems that the flux from the auroral region vanishes at a distance of 100—150 Earth radii.

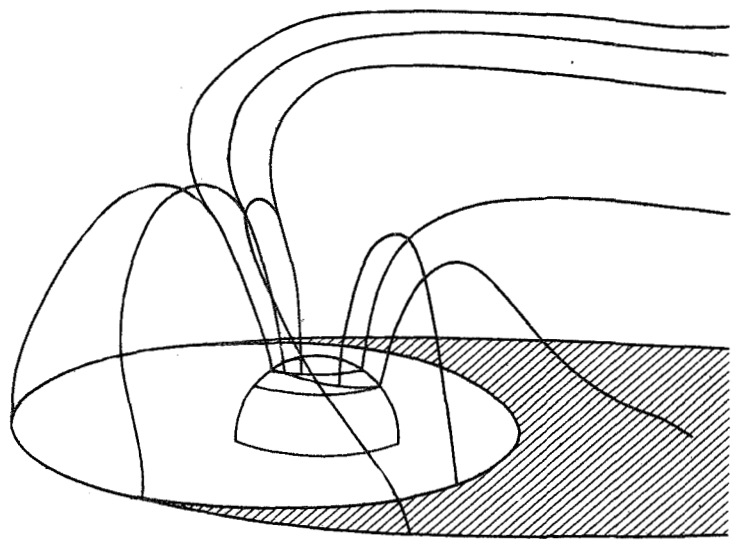

FIGURE 1. The geometry of magnetic lines from the high-latitude region. The lines from the inner zone are associated with the boundary of the magnetosphere, and the lines of the oval with the boundary of the plasma layer.

Studies of the distribution of low-energy plasma in the space around the Earth led to the conclusion that the Earth is surrounded by a relatively dense plasma — a plasmosphere, with a sharp boundary at a distance of 3—5 Earth radii; the plasma density drops markedly on crossing this boundary /17/. At large distances (about 10 Earth radii), Gringauz et al. /18/ discovered a region where the number of electrons with energies above 200 eV again increases. Vasyliunas /19/ in a recent report published a detailed review of the results pertaining to this part of the interplanetary space. The measurements were carried out in the evening sector of the magnetosphere; the lines of force emerging from the oval (in the form indicated by Feldstein and Starkov /20/) constitute the boundary of a plasma layer beyond which (farther from the Earth) high-intensity particle fluxes with energies above 1 keV are observed, and the mean energy density reaches 1 keV/cm^3. In the part of space inside this boundary, instruments with threshold sensitivity of 40 eV detected no measurable particle fluxes. The boundary of the plasma layer is sharp and distinct, its thickness not exceeding 0.4 Earth radii; the position of this boundary depends on the level of magnetic activity, varying in this sector from 11—12 radii in quiet times to 6 radii in stormy periods. The thickness of the layer at right angles to the equatorial plane is about 5 Earth radii. Figure 1 shows (greatly out of scale) a section through the magnetosphere obtained with the equatorial plane. The lines of force emerging from the oval, in accordance with Vasyliunas' results /19/, cross the equatorial plane at the boundary of the plasma layer; the lines of force corresponding to lower latitudes close through the parts of the magnetosphere near the Earth; the high-latitude lines trail off into the tail gradually closing through the neutral layer. The entire system

maintains a constant attitude relative to the Sun, and therefore rotates relative to the Earth. The Earth with its magnetic field rotates in the system of axes with fixed attitude to the Sun. This rotation must be taken into consideration if, in addition to the geomagnetic field, the Earth is also assigned an electric field

$$E = -\left[\frac{V}{c}, H\right]. \tag{2}$$

It is readily seen that, assuming a dipole geomagnetic field, the associated electric field can be represented as a gradient of the potential

$$\varphi = -\frac{\Omega M}{r}\sin^2\theta, \tag{3}$$

where M is the magnetic moment of the Earth, Ω is the angular velocity of the Earth.

Since the potential is determined apart from an additive constant, we can choose this constant so that the potential of the inner zone linked by lines of force with the magnetospheric boundary and the interplanetary space is zero. In this scheme, the pole is assigned a potential of +6 kV, the Fritz zone (ϕ = 65°) −10 kV, and the equator (in accordance with (3)) − 84 kV. If we assume that the lines of force are ideal conductors and are thus also lines of constant potential, the potential distribution and the electric field in the cross section through the magnetosphere tail should correspond to the pattern shown in Figure 2 (viewed from the Earth). The field vectors are directed from the centers of each segment of the magnetospheric "theta" through which passes the line of force of the geomagnetic pole, converging toward the middle of the neutral layer, through which pass the lines of force from the points of the oval closest to the equator in both hemispheres (these lines carry the most negative potential). The magnetic field in the upper (north) part of the tail is directed to the Earth; in crossed field in the northernmost part of the tail, the lines of force drift clockwise, synchronously with the diurnal rotation of the polar cap; in the inner part of the section, adjoining the neutral layer, the drift is directed from the evening to the morning side of the tail. The velocities invariably correspond to the diurnal rotation. Adjoining the neutral layer, the electric field is parallel to the layer and points to its middle. In the magnetic field of the layer, directed to the north part of the tail, the drift is away from the Earth on the evening side of the tail and to the Earth on the morning side (Figure 3). The

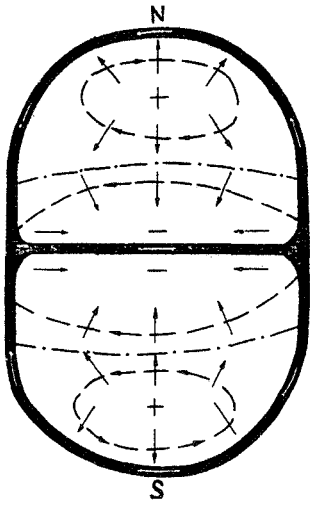

FIGURE 2. A section through the magnetosphere tail (viewed from the Earth). The directions of currents along the boundary, the electric field, and the drift of lines of force are shown. The dash-dotted line traces the boundary of the fluxes from the cap and from the auroral region. This boundary is also the zero-potential surface.

diurnal motion of a line of force thus consists of daytime rotation with the Earth, rapid trailing off into the tail in the evening, switch-over to the morning side of the tail during the night, and finally rapid return to the parts of the magnetosphere near the Earth in the morning hours. Let us consider this motion in more detail.

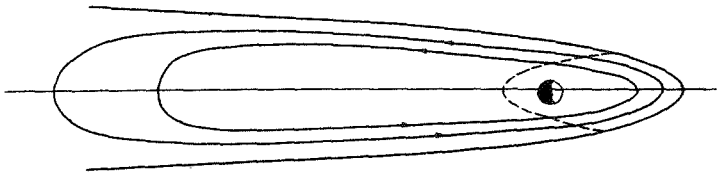

FIGURE 3. Plasma drift in the equatorial plane associated with the diurnal rotation of the Earth.

The daytime drift is produced by field (2) or (3). The transition to the evening drift mode, i.e., the lines trailing off into the tail, occurs at the time when the particular point on the Earth's surface approaches the oval and enters the part of space with a low magnetic field. The electric field associated with the Earth's rotation can be distorted by the boundary of the plasma layer; this distortion, apparently, compensates the field component normal to the boundary, while the tangential component crosses the boundary unaffected. The isopotential lines near the boundary are perpendicular to the boundary and the plasma therefore drifts at right angles to the boundary. Since the tangential component of the electric field remains constant, the marked drop of the magnetic field should produce a similarly pronounced increase in drift velocity. This may be attributed to the decrease in field strength, i.e., to the increase in the spacing between lines of force. The drift velocity is expected to continue increasing as the line of force moves through the plasma layer, provided this layer is exposed to solar wind pressure. Indeed, if we consider an isolated jet, its surface is isopotential and the electric field inside the jet should increase as it becomes thinner. The increase of the electric field, on the other hand, should increase the drift velocity, which in its turn should pinch the jet and increase the field. The motion inside the plasma layer can be classified as an instability — the transition from one stable state, with the lines of force closing through the near magnetosphere, to another stable state, with the lines of force closing through the tail.

When a drifting particle crosses the boundary where the magnetic field drops abruptly, its energy increases to

$$w = w_0 + m \cdot v_{dr}^2, \tag{4}$$

where w_0 is the energy of the particle when it reaches the boundary, v_{dr} is the drift velocity.

The physical reason for the increase in energy is that the particle is displaced along the electric field due to a change in the radius of curvature

(in general, this change in curvature is substantial in a small field). From equation (3), the electric field at the level of the boundary of the plasma layer should reach about 1 kV/Earth radius. If the magnetic field inside the plasma layer is taken equal to 1 gamma, the energy increment associated with the crossing over into a region of weaker magnetic field should be about 200 eV for a proton. The radius of curvature under these conditions is about $\frac{1}{4}$ of the Earth's radius, and the gyroperiod of a proton is about 1 min.

The very existence of the boundary of the plasma layer is apparently associated with this plasma drift phenomenon: in the space between the plasmosphere and the plasma layer, the density of the low-energy plasma is apparently higher than in the plasma layer, but its energy is below the sensitivity threshold of the instruments. Drifting in the field of the Earth's diurnal rotation, the low-energy plasma particles cross the boundary of the plasma layer. Due to the sudden increase of the gyroradius, the particle is displaced along the field. This displacement, accompanied by a certain acceleration of the particle, constitutes the current element which determines the magnetic field discontinuity across the boundary. The thinner the boundary, the easier is the transition from one radius to another and the easier is the generation of current along the boundary. Since current enhancement narrows the boundary, the entire process should produce a sharp boundary, as is actually observed. In the above analysis, we operated with protons only, whereas the measurements give the electron energy. There is probably an additional mechanism, in the form of local electric fields, equalizing the energies of electrons and protons.

Upon crossing the boundary, the drift approximation probably breaks down. Indeed, the thickness of the boundary layer is comparable to the radius of curvature, and the conditions of motion therefore change radically over a distance of the order of the radius. Fluctuations may cause a substantial change in the magnetic field during one revolution of the proton. Drifting inside the plasma layer, the particles enter a region where the thickness of the neutral plasma layer is comparable with the proton gyroradius. The drift approximation breaks down because both the gyroradius and the gyroperiod of a proton in a weak magnetic field are very large. The breakdown for the proton occurs earlier than that for the electron; the electrons drift with the line of force, whereas the protons may be lost by the line. The plasma moving with the line of force is therefore enriched in negative charges. The diurnal motion of the lines of force therefore leads to a buildup of negative charge on the evening side of the magnetosphere tail and positive charge on the morning side. The slow drift of the lines of force overnight does not require any further charge separation.

The above processes are associated with charge transfer from the boundary of the plasma layer into the tail interior and back. The charges induced near the outer surface of the layer apparently leak to the Earth, without causing any noticeable geophysical effects. Charge buildup inside the magnetosphere tail creates an additional electric field there, and the drift trajectories are altered. This effect can be allowed for by plotting the isopotential lines, which govern the particle drift. Initially, as in Figure 2, the potential inside the neutral layer had a minimum of -10 kV

in the middle part of the layer. The appearance of additional charges will alter the potential distribution: it will be lower on the morning side and higher on the evening side, as marked by the solid line in Figure 4b. The drift paths join the Earth only with those parts of the tail which are at the same potential as the Earth, i.e., between 0 and -10 kV. In Figure 4, these regions are marked by thick lines. The potential of the regions in between is either too low or too high, and they are therefore not joined with the Earth. Closed eddies form around these regions (Figure 4a) which essentially fit the Axford and Hines scheme /3/.

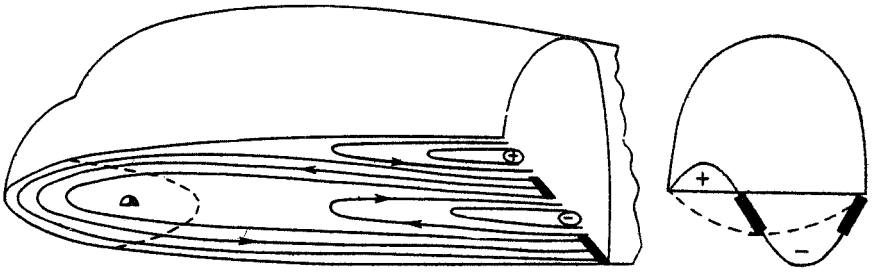

FIGURE 4. Formation of eddies in the neutral layer of the tail (a) and potential distribution in the neutral tail (b). The dashed line marks the situation produced by the diurnal rotation alone, and the solid line presents the distribution corresponding to charge transport. Thick segments identify the regions which are maintained at the same potential as the Earth.

The energy balance of this process can now be estimated. If we take tentatively 1 cm^{-3} for the density of protons in the neutral layer, 1 gamma as before for the magnetic field, and insert the electric field at the end of the process from equation (1), we obtain for the energy density

$$w = 2.5 \cdot 10^{-9} \left(1 + \frac{K_p}{5}\right) \text{ erg/cm}^3.$$

If the process is assumed to encompass a volume of 100 X 40 X 1 radii, i.e., approximately 10^{30} cm^3, the above expression gives a figure of the order of $2.5 \cdot 10^{21}$ erg for the total eddy motion energy in the tail plasma layer for a perfectly quiet field and 10^{22} for $K_p = 5$. The strength of the charge separation process can also be estimated. The tail and its plasma layer move relative to the Earth, trailing the Sun; the plasma layer exerts a certain pressure on the confining lines of force, i.e., on the lines of force of the oval. We tentatively assume the layer to be highly asymmetric, so that it exerts pressure only on the evening side of the Earth. This assumption is partly justified by the pronounced asymmetry of the plasmosphere, which is stretched above the evening meridian. If we take for the pressure $H^2/8\pi$, inserting for the field double the dipole field value (this doubling of the field is associated with the effect of the nearby boundary), the retarding effect produced by a strip of unit thickness stretched along the equator is then found to be $H_0^2 R_E^2/8\pi L^4$, where

$H_0 = 0.3$ is the field at the equator, L is the parameter of the line of force in the plasma layer which is closest to the equator, *i.e.*, the parameter of the Fritz zone (L = 6 according to the above). If the half thickness of the plasma layer near the Earth is 3—5 radii, we obtain for the layer power $5 \cdot 10^{16} - 10^{17}$ erg/sec. If the eddies and the associated electric field break up completely during a storm, some 24 hours will be required to restore the conditions corresponding to $K_p = 5$.

Charge separation is feasible only if charge leakage is substantially slower than charge buildup. Therefore, in a quiet magnetosphere, there is no potential transfer from the neutral layer to the Earth possibly because the neutral layer particles, with their large pitch angles, cannot escape from the deep magnetic field minimum in which they are trapped. If this isolation is broken at any time and the potential difference set up in the plasma layer is transmitted to the adjoining regions of the magnetosphere and onward along the lines of force to the Earth, a DP-2 disturbance is observed, as described by Obayashi and Nishida /21—23/: Hall current eddies are induced around high and low potential pockets in the ionosphere (Figure 5). The estimates in /22/ suggest that a potential difference of some 50 kV is needed to produce the variation; this figure is close to the result obtained from (1).

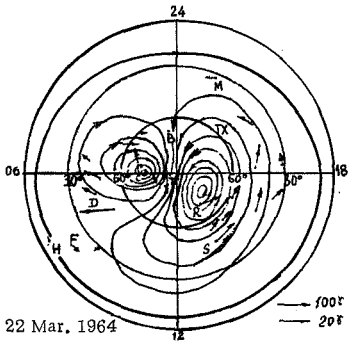

FIGURE 5. The current system of a DP-2 disturbance /23/.

A polar substorm is accompanied by a DP-1 magnetic field disturbance which is characterized by a current system in the shape of two jets flowing along the principal auroral zone in opposite directions (Figures 6a and 6b) or a closed current eddy embracing the oval (Figure 6c). The first two models were discussed in most of the earlier studies, and the last variant was first published in /24, 25/. As we have noted above, the assumption that the motivating force of the current system is localized in the current jet is inconsistent with our concepts of the electrical field in the magnetosphere. The current systems in Figure 6 are apparently produced by the general magnetospheric field interacting with the injected particle fluxes.

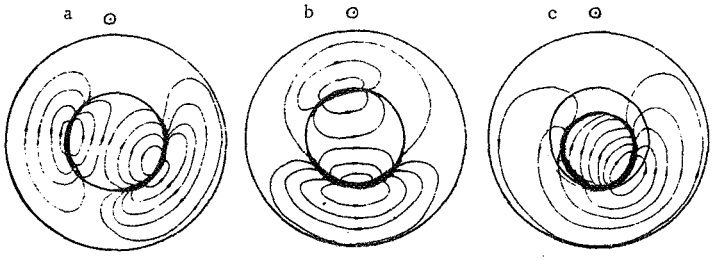

FIGURE 6. The current systems of a DP-1 disturbance /22/.

The particle fluxes injected in the ionosphere create a narrow conducting channel. Because of the existence of the boundary, the direct and the Hall conductivity in this channel change to Cowling conductivity, and the medium inside the channel is transformed into an excellent, relatively isotropic conductor. If a potential difference is applied between the evening and the morning side of the Earth (this potential difference may be transmitted from the magnetosphere along the lines of force) and the injecting particles have created a conducting channel short-circuiting this potential difference, electric current will flow in the closed circuit comprising the conducting regions in the ionosphere and the volume conductors — the lines of force. The magnetic field of this current is the same as that of the current system shown in Figure 6a and 6b: the field below the current jet is determined by the jet alone, and the field far from the jet is determined by the feeding conductors, whose field is indistinguishable from the field of the currents closing the jet. Thus, quiet conditions correspond to lack of any direct electric contact between the neutral layer of the tail and the Earth. When this contact is established and the potential is transmitted to the Earth, a DP-2 disturbance is observed. If the electric contact is further reinforced by particle injection, creating a conducting channel in the ionosphere, a DP-1 current system is formed. The high conductivity of the channel lowers the potential difference in the ionosphere and suppresses the DP-2 disturbance. The above model explains the principal features of the high-latitude geomagnetic disturbances. Certain discrepancies, however, nevertheless remain. Thus, the region of the largest potentials of the DP-2 variation (Figure 5) does not coincide with the ends of the current jets of the DP-1 system (Figures 6a and 6b). The existence of the current loop (Figure 6c) has not been explained either.

The transition from a DP-2 disturbance to a DP-1 disturbance is associated with particle injection. According to present-day concepts /26/, particle injection is linked with a sudden contraction of the lines of force previously stretched into the tail. The contraction is a rapid process, not unlike the breakdown of an instability, and it apparently involves partial loss of ions, like the diurnal motion of the lines of force. This, in its turn, will increase the electron content of the plasma transported Earthward by the contracting lines, whereas the distant parts of the tail are enriched with ions. As a result, the previously discussed field with a positive potential on the morning side of the magnetosphere and the ionosphere is supplemented by an additional field on the night side of the Earth, with a higher potential at higher latitudes. The centers of the charged regions are thus shifted in the required direction: the negatively charged region moves to lower latitudes, closer to the midnight meridian, and the positively charged region settles on the opposite meridian at higher latitudes (Figure 7).

There is one other factor to be considered: when the electric isolation of the neutral layer is broken, the weak electric field will be distorted (Figure 2) if the potential of the neutral layer is transmitted to that part of the magnetosphere where the field is directed to the Earth. Drift paths may form, linking the positive potential pockets in the neutral layer with the central part of the cross sections, where the lines from the near-polar region pass (Figure 8). The positively charged region

in this case extends from the neutral layer to the central part of the tail section, and when projected onto the Earth along the lines of force, the positive potential will spread over the entire near-polar region.

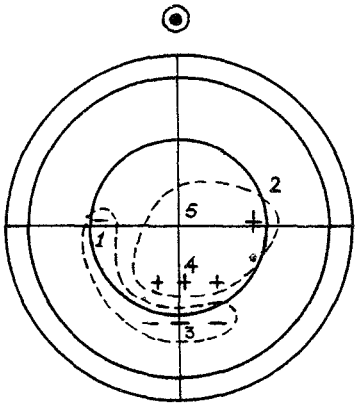

FIGURE 7. Potential distribution in the ionosphere during a DP-1 disturbance. The potential in regions 1,2 is created by the principal magnetospheric field, that in regions 3,4 by the field of injected particles, in region 5 by charge transfer to the central part of the tail.

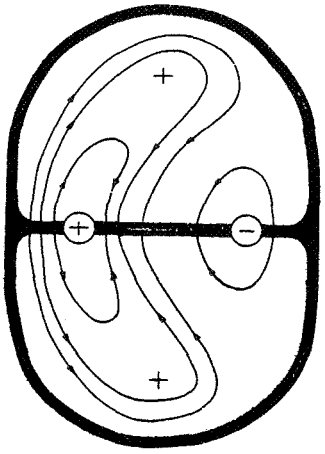

FIGURE 8. Possible drift paths in the tail when the isolation of the neutral layer has been broken.

The current system in Figure 6c differs from the other two current systems in that here a current jet extends in a direction almost opposite to the first two jets; the formation of this jet cannot be explained as the closing of an electric circuit between regions maintained at different potentials. Burdo /27/, in his search for general regularities governing the distribution of magnetic activity at high latitudes, proposed a chart of distribution of activity maxima which coincided with the chart of the maximum ionospheric current. At high latitudes, the activity maxima fell along three spirals, two of which extended from the day side of the inner zone, bypassing the pole on both sides, toward the night side of the principal zone; the third spiral stretched toward the evening side of the principal zone and along it. If these spirals are charted as on Figure 6, the first two will approximately coincide with the oval (Figure 6c), and the third with the daytime current (Figures 6a and 6b). It thus seems that the current systems (Figure 6) are made up of three basic jets: the morning jet, the night jet, and the evening jet. A combination of two jets — morning and evening — is responsible for the system shown in Figures 6a and 6b, whereas the current system in Figure 6c is produced by a combination of a morning and a night jet. The morning and the night jets have been previously associated with the shortcircuiting of different potentials. The night jet apparently can be identified with a Hall current flowing along the region of maximum electric field (maximum potential gradient) adjoining the boundary of the positive potential region. The difference in the origin

of these jets is also reflected in their shape: the night jet shows a much poorer focusing than the other two jets, and it has no sharp boundaries (which are produced by the injection region); the variation of the electric field and the Hall currents is furthermore more gradual. The blurred shape of this jet /24, 25/ is apparently one of the reasons why scientists concentrated on it at a much later date than on the other two.

It thus seems that the Earth's rotation produces a general magnetospheric electric field and a general circulation of the type described by Axford and Hines /3/. The generation of this field and the convection motion consume about 10^{22} erg, and the power of the charge separation mechanism is 10^{17} erg/sec. In quiet periods, the electric field arising in the neutral layer of the tail is not linked to the Earth and does not affect the geophysical processes. The penetration of this field in the magnetosphere and its propagation along the lines of force to the Earth produces a DP-2 disturbance. If this effect is further reinforced by particle injection, the field geometry is somewhat altered and the DP-2 variation changes to DP-1 disturbance, i.e., a polar substorm. The ionospheric current system of this disturbance in general is made up of three branches of different origin: two of the three branches are discharge currents flowing along the high-conductivity channel, and the third branch is a Hall current in the region of maximum electric field. The currents along the lines of force feeding the ends of the current jets also play an important role in the generation of the DP-1 magnetic field.

Bibliography

1. Bryunelli, B. E. — In: "Fizika magnitosfery i polyarnye buri," Trudy Letnei shkoly po kosmofizike, p. 3. Irkutsk, Izd. SO AN SSSR. 1968.
2. Bryunelli, B. E. — Trudy V Vsesoyuznoi ezhegodnoi zimnei skoly po kosmofizike, p. 212. Apatity, Izd. Kol'skogo filiala AN SSSR. 1968.
3. Axford, W. I. and C. O. Hines. — Canad. J. Phys., 39(10):1433. 1961.
4. Freeman, J. W. — J. Geophys. Res., 73(13):4151. 1968.
5. Montgomery, M. D. — J. Geophys. Res., 73(3):871. 1968.
6. Vasyliunas, V. M. — J. Geophys. Res., 73(7):2529. 1968.
7. Piddington, J. H. — Planet. Space Sci., 16(6):703. 1968.
8. Yanovskii, B. M. Zemnoi magnetizm (Geomagnetism). — Leningrad, Izd. LGU. 1963.
9. Nikol'skii, A. P. — In: "Fizika solnechnykh korpuskulyarnykh potokov i ikh vozdeistvie na verkhnyuyu atmosferu Zemli," p. 144. Moskva, Izdatel'stvo AN SSSR. 1957.
10. Khorosheva, O. V. — Geomagnetizm i Aeronomiya, 2(5):839. 1962.
11. Feldstein, Ya. I. — Geomagnetizm i Aeronomiya, 3(2):227. 1963.
12. Frank, L. A., J. A. van Allen, and J. D. Graven. — J. Geophys. Res., 69(15):3155. 1964.
13. Bobrov, M. S. — Astronomicheskii Zhurnal, 36(6):1028. 1959.

14. Mead, G. D. — J. Geophys. Res., 69(7):1181. 1964.
15. Taylor, H. E. and E. W. Hones. — J. Geophys. Res., No. 15:3605, 1965.
16. Mihalov, J. H., D. S. Colburn, R. G. Currie, and C. P. Sonett. — J. Geophys. Res., 73(3):943. 1968.
17. Carpenter, D. L. — Radio Science, 3(7):719. 1968.
18. Gringauz, K. I., V. G. Kurt, V. I. Moroz, and I. S. Shklovskii. — DAN SSSR, 132(5):1062. 1960.
19. Vasyliuvas, V. M. — J. Geophys. Res., 73(9):2339. 1968.
20. Feldstein, Y. I. and G. V. Starkov. — Planet. Space Sci., 15(2): 209. 1967.
21. Obayashi, T. — In: "Solnechno-zemnaya fizika," p. 172. Moskva, Izdatel'stvo "Mir." 1968.
22. Obayashi, T. and A. Nishida. — Space Sci. Rev., 8(1):3. 1968.
23. Nishida, A. — J. Geophys. Res., 73:1795, 5549. 1968.
24. Feldshtein, Ya. I. and A. N. Zaitsev. — Geomagnetizm i Aeronomiya, 5(6):1123. 1965.
25. Akasofu, S. I., S. Chapman, and C. I. Meng. — J. Atmos. Terr. Phys., 27(11/12):1275. 1965.
26. Piddington, J. H. — J. Atmos. Terr. Phys., 29(1):87. 1967.
27. Burdo, O. A. — In: "Fizika solnechnykh korpuskulyarnykh potokov i ikh vozdeistvie na verkhnyuyu atmosferu Zemli," p. 159. Moskva, Idatel'stvo AN SSSR. 1957.

MAGNETIC STORM DEVELOPMENT IN THE EARTH'S MAGNETOSPHERE

M. I. Pudovkin, S. I. Isaev, and S. A. Zaitseva

A magnetic storm is a highly complex agglomeration of various phenomena occurring in the Earth's ionosphere or magnetosphere. The sequence and the interrelation of the phenomena taking place in the ionosphere (polar aurorae, formation of enhanced ionization regions, electrical currents) have been studied in fair detail /1—3/. Our knowledge of the processes which develop during the magnetic storm in the magnetosphere is much less comprehensive, however.

It has been shown /4, 5/ that the study of polar storms reveals the dynamics of magnetospheric processes and thus provides us with a key to the understanding of the mechanism of storm generation as a whole. Moreover, the magnetospheric substorm (whose terrestrial counterpart is the polar storm) can be regarded as an elementary form of a general worldwide magnetic storm. We will therefore first concentrate on the development of an elementary polar storm. The exact choice of the commencement of the polar storm is a factor of great importance in these considerations. According to Akasofu /6/, the commencement of a polar substorm is generally identified with the commencement of the negative bay in the midnight region of the auroral zone. Khorosheva /7/ has shown, however, that at latitudes above the Fritz zone, the disturbance may commence long before the commencement of the bay in the zone proper. This conclusion is also confirmed by the findings of /8/.

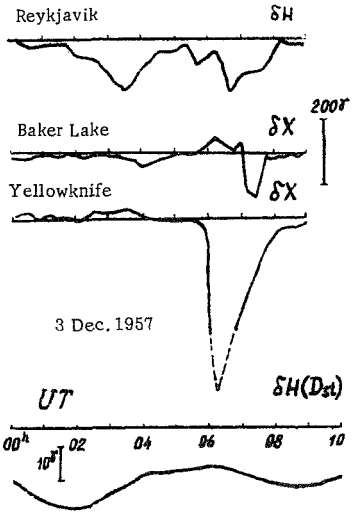

FIGURE 1. The development of a polar magnetic storm on 3 December 1957 at high latitudes and the $\delta H(D_{st})$ curve.

Figure 1 plots according to /9/ the variations δH in the bay of 06^h-08^hUT, 3 December 1957, as recorded at Yellowknife ($\phi = 69°.8$ N, $\Lambda = 295°$), Baker Lake ($\phi = 75°.1$ N, $\Lambda = 320°$), and Reykjavik ($\phi = 66°.6$ N, $\Lambda = 71°$). We see that at Yellowknife a sharp bay was observed against the background of an exceptionally quiet field, commencing distinctly at 05^h50^mUT. The δX curve at Baker Lake shows, however, that in accordance with the results of /7, 8/

the bay commencement at higher latitudes substantially preceded that at Yellowknife. A similar picture was observed at the Reykjavik observatory, which in the relevant period lay on the morning side (LT = $6^h - 8^h$) of the auroral zone. Here a substantial disturbance began about 4 hrs prior to the commencement of the Yellowknife bay.

Analysis of 30 geomagnetic bays carried out by Ivliev et al. /9/ shows that this is a typical situation, i.e., every magnetic bay is preceded by a peculiar disturbance. This preliminary disturbance differs from a typical geomagnetic storm in that its intensity is maximum not on the night side of the Earth, in the auroral zone, but rather on the morning side (Figure 2), at latitudes of 70 — 80°. It thus seems that the development of this disturbance is associated with the injection of plasma along the geomagnetic field lines passing through neutral points. This conclusion is confirmed by the results of /10/, according to which the auroral intensity on the day side of the auroral oval also increases considerably about 1 or 2 hrs prior to bay commencement on the night side of the auroral zone.

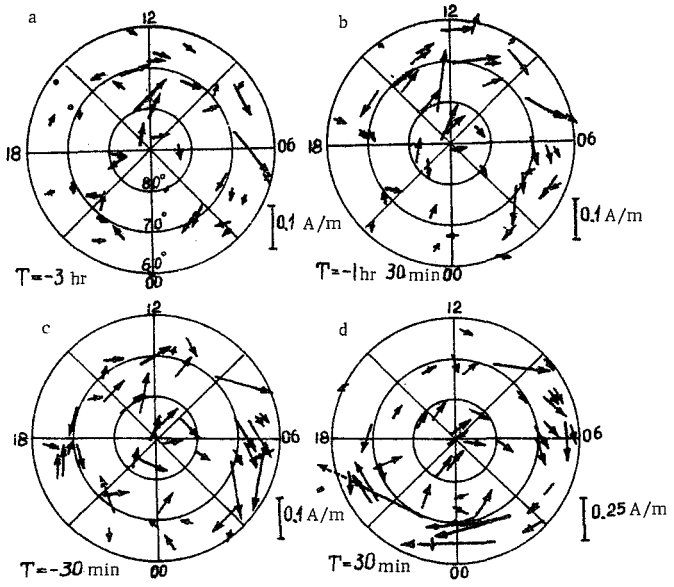

FIGURE 2. Space and time distribution of the disturbance currents in the polar cap (average for 30 storms) at various times after the commencement of the polar substorm.

What is the origin of this preliminary disturbance? According to /11, 12, 13/, every elementary magnetic storm on the night side is preceded by a small and yet sufficiently pronounced geomagnetic field disturbance on the equator (which occurs 1 — 3 hrs before the storm). This disturbance is apparently linked with an increase in solar wind pressure. The curves in Figure 1 show that an enhancement of the field H at low latitudes was observed in this case on 3 December 1957. The enhancement began simultaneously with the commencement of the preliminary disturbance in Reykjavik.

It thus seems that the preliminary disturbance in the polar cap, preceding the development of a polar bay, is directly associated with the increase in the solar wind pressure on the Earth's magnetosphere. The development of a geomagnetic bay is connected with the injection of auroral plasma from the magnetosphere tail /5, 11/. Since the plasma moves in a magnetic field, it apparently sets up an electric field in the Earth's magnetosphere during the storm; this field is directed from the morning to the evening side of the Earth.

In addition to the general drift toward the Earth, the particles also experience a gradient drift around the Earth, the protons drifting westward and the electrons eastward. This gradient drift can be observed in the westward displacement of positive bays of a certain kind along the auroral zone (proton drift) and in the eastward displacement of the absorption bays (electron drift) /5/. The following basic factors should be noted in this relation:

1. The region of corpuscular injection drifts along the Fritz zone, and not along the auroral oval. This implies that the drift envelope, touching the oval on the Earth's night side, does not coincide at any other point with the oval. As a result, the auroral oval can be identified with the outermost boundary of stably trapped radiation.

2. The particle energy increases in the course of the drift around the Earth.

The last conclusion is illustrated by Figure 3, which gives the diurnal variation of the energy of the electrons /14/ and protons /15/ injected into the upper atmosphere. The curves in Figure 3 show that the energy of auroral electrons is maximum at 07 hrs and minimum at 19 hrs local time, whereas the proton energy is conversely maximum at 18 hrs LT. This longitudinal distribution of particle energies points to the existence of an electric field in the magnetosphere. To judge from the figure, this field is equal to 10^{-5} V/cm and is directed from east to west on the Earth's night side. These results fit the conclusions derived from the analysis of the motion of polar arcs.

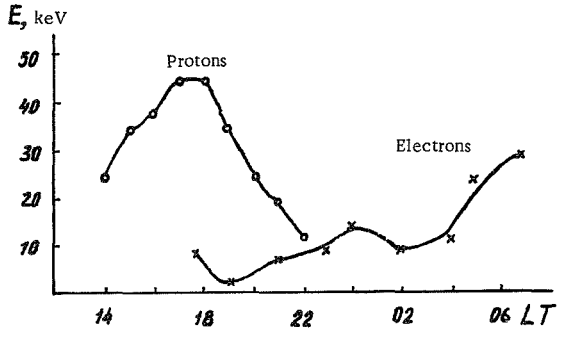

FIGURE 3. The diurnal variation of the energy of injected protons and electrons in the auroral zone.

How and when does the electric field form in the magnetosphere? Since the motion of the auroral arcs toward the equator begins almost simultaneously

with the enhancement of the field H on the equator /9/, it seems that the electric field is also generated at that time. This assumption is borne out by the fact that for $E=10^{-5}$ V/cm, a plasmoid will take about 1.5—2 hrs to move from the magnetosphere tail to the L corresponding to the auroral zone, and these are exactly the time intervals representing the delay of the magnetic storm commencement relative to the enhancement of the field H on the equator /11/. There is thus serious reason to believe that the development of the field E in the magnetosphere is associated with changes in some of the solar wind parameters. The electric field generation mechanism has been treated in detail in /16, 17/, where it is shown that the strength and the direction of the magnetospheric electric field are determined by the frozen magnetic field of the solar wind. Direct observations from satellites /18—20/ apparently confirm the theory of /14/.

The existence of an electric field in the Earth's magnetosphere explains the acceleration of the auroral plasma and also a number of other finer features in the development of polar storms, e.g., the shape of the electron and proton injection zones and their mutual position, the diurnal variation of the azimuths of the auroral arcs, the velocities of auroral glow inhomogeneities, etc. /16, 17/. The satisfactory fit between theory and experiment seems to suggest that the problem of development of an elementary polar storm in the magnetosphere has been solved in general lines.

Let us now consider the development of a universal magnetic storm. As is known, the main phase of the storm involves the formation (or enhancement) of a belt of DR currents, which in its turn is linked with an increase in the overall kinetic energy of the particles trapped by the geomagnetic field. The intensity of the DR field observed on the ground is related by the energy of the trapped particles by the equality $W=\frac{1}{2}M_E\cdot\delta H$ /21—23/, which for medium-strength storms ($\delta H=50\gamma$) gives $W=2\cdot10^{22}$ erg. The major part of the kinetic energy concentrated in the radiation belts is carried by low-energy particles with energies below 50 keV /24, 25/. This result is vividly illustrated by the table below /25/.

Total energy of protons and electrons (200 eV ≤ E ≤ 50 keV) in radiation belts

1966	Particles with 200 eV ≤ E ≤ 50 keV	Total particle energy for 1 ≤ L ≤ 8, erg	ΔB(0) calculated, gammas	D_{st}(H) observed, gammas
23 June	Protons	$4.8\cdot10^{21}$	−12	*Quiet field*
25 June	"	$1.4\cdot10^{22}$	−36	−30 (± 10)
9 July	"	$2.1\cdot10^{22}$	−55	−50 (± 10)
	Electrons	$5.3\cdot10^{21}$	−14	

Thus, the nature of the DR currents has been elucidated. And yet the mechanism of formation of the DR belt is not quite clear. We have shown above that certain information on processes in the disturbed magnetosphere can be obtained from the analysis of polar storms. Therefore, before attempting to elucidate the formation mechanism of DR currents, we will consider the relation between DR and DP disturbances.

Already Chapman and Sugiura /26/ and Akasofu and Chapman /27/ showed that the development of the main phase of a magnetic storm is intimately

linked with polar disturbances. However, the causal relation between these factors remained unclear. This problem was considered in greater detail in /4/, where the authors came to the conclusion that the belt of DR currents forms simultaneously with the injection of the auroral plasma into the auroral zone. It is significant that the total energy of particles injected into the auroral zone is proportional to the energy injected into the DR current belt /4/. These data seem to indicate that the formation of the DR belt is not only simultaneous with but is also directly associated with the development of a polar storm in the Earth's magnetosphere.

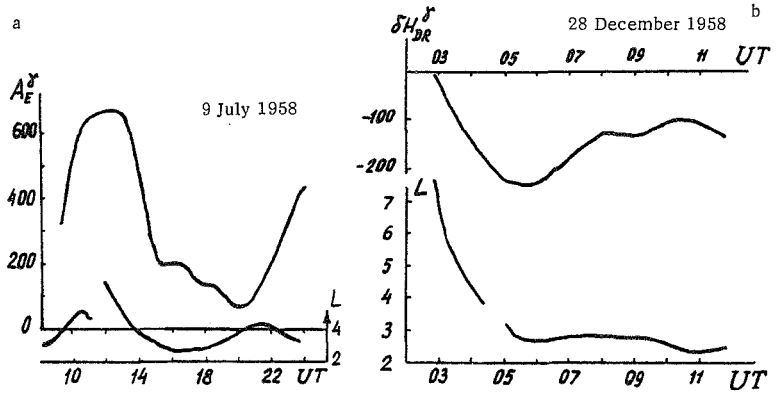

FIGURE 4. Variation in the position of the DR current belt during a polar storm: a — 9 July 1958 (magnetic data); b — 28 December 1958 (observation of a red stable arc).

Let us now try to establish how the DR belt exactly forms. To this end, we will consider some peculiar features observed for particular storms. Figure 4a plots, according to the data of /28/, the variation of the mean radius of DR currents (assuming that they are shaped as an equatorial current ring) during the recovery phase of the storm of 9 July 1958. Figure 4a also gives the intensity of the polar disturbances (the AE indices according to /29/). We see from the curves that around 10—11 hrs UT, the intensity of the polar disturbances markedly increases, reaching a maximum at 12 hrs UT. At the same time the radius of the DR currents increases (up to $7R_E$), and this may be interpreted as due to the formation of a new DR belt at a greater distance from the Earth. As the polar storm develops, the radius of the DR belt decreases, reaching the minimum value of $\rho = 2.2R_E$ toward the end of the polar storm. In the period free from strong polar disturbances (16—20 hrs UT), the radius of the DR currents slowly increases, and a renewed decrease begins simultaneously with the commencement of a new burst of polar disturbances. Analysis of several storms carried out in /28/ shows that this is a typical pattern, i.e., during strong polar storms, the radius of the DR belt generally decreases, only to increase in the quiet periods.

However, the determination of the radius of the DR belt from ground magnetic data involves a number of serious errors /28/, so that more reliable (though scantier) results are obtained from observations of middle-latitude red arcs, whose relation to the DR belt has been convincingly

demonstrated in /39—33, 28/. Figure 4b plots the position of the red arc from observations at Barrow ($\phi = 68°.6$ N), College ($\phi = 64°.7$ N), Fritz Peak ($\phi = 48°.7$ N) and the variation of $\delta H(D_{st})$ from the data of /34/. Again, as in the case of the storm of 9 July 1958, the arc, which is in fact a projection of the DR belt along the geomagnetic field lines onto the ionosphere, appeared near the auroral zone (L=7) and moved toward lower latitudes to $L \approx 2.5$ as the storm developed. The data of ground observations of the DR current field and of middle-latitude red arcs thus show that the DR currents originate in the magnetosphere at distances corresponding to the auroral zone, and only later move deeper into the magnetosphere. This result is also borne out by satellite observations. Indeed, Figure 5b, borrowed from /24/, shows the equatorial distribution of the proton flux intensity with $E < 50$ keV during the storm of 7—13 July 1966 (Figure 5a). We see that both before and after the storm, a low-intensity low-energy radiation belt was observed at a distance of $6-7 R_E$ from the Earth. During the main phase of the storm, the particle flux intensity in the belt increased almost by one order of magnitude and the belt intensity maximum shifted to L=3.5.

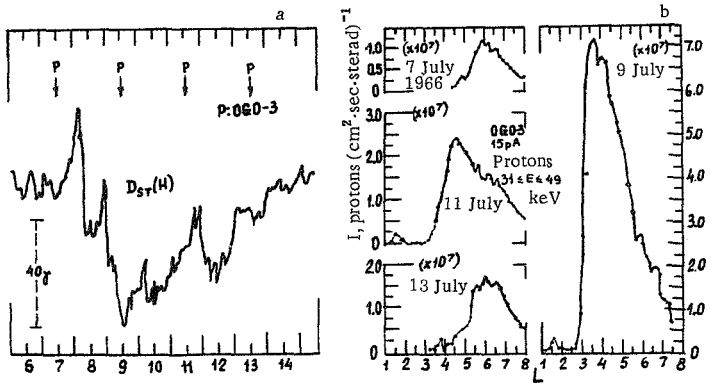

FIGURE 5. The variation of $\delta H(D_{st})$ during the storm of 7—13 July 1966 (a) and the equatorial distribution of the proton flux intensity for 31 keV $\leq E \leq$ 49 keV during this storm (b).

The plasma filling the DR belt during the storm thus penetrates into the inner magnetosphere from the peripheral regions. This penetration occurs simultaneously with the injection of the auroral plasma, also mainly on the night side /34/. It therefore seems that the auroral plasma moving during the storm from the magnetosphere tail acts as a source of both the polar storms and the DR currents /4/. The authors of /35—37/ reach the same conclusion.

The acceleration of charged particles in the Earth's magnetosphere during a polar storm was considered in detail on the basis of Alfven's theory in /38/. The results show that as the particles move from the magnetosphere tail to the L corresponding to the auroral zone, the particle energy increases by

1 ∓ 2 orders of magnitude. A highly significant factor is that the existence of the electric field in the magnetosphere is apparently intermittent, and not continuous: it is turned on for about 1.5—2 hrs at a time /11, 38/, with a mean periodicity of about 4 hrs /2/. As a result, only part of the particle trajectory around the Earth lies in an electric field (otherwise, no significant change in energy would be registered), and the mean particle energy increases. If the time to complete one circuit around the Earth coincides with the recurrence period of the polar bays, the particle acceleration mechanism becomes highly effective. It can be shown that for a bay recurrence period of some 4 hrs at L=4—5, the acceleration is most effective for particles with energies of a few tens of keV. This result is apparently not inconsistent with the experimental findings /24, 25/.

We thus see that the polar substorm is an elementary form of the universal magnetic storm as a whole, and not only of the polar storm. However, the relation between the DP and DR disturbances is not limited to the above considerations, and the development of the DR currents in its turn affects the development of the polar storm.

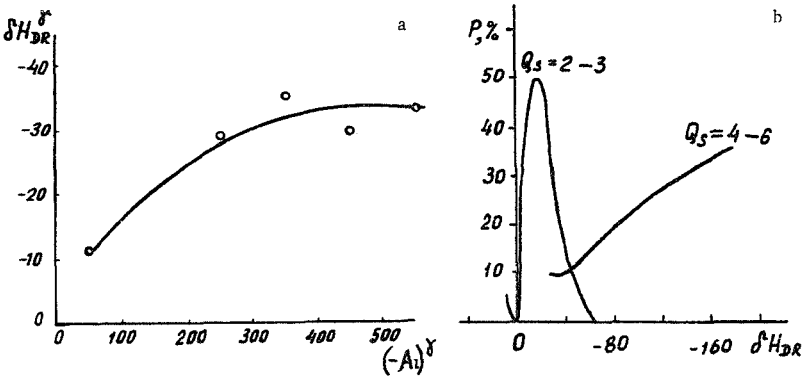

FIGURE 6. The field of DR currents and the intensity of polar disturbances (A_L index) at the time of splitting of the auroral zone ($\Delta l \geqslant 200$ km) (a) and the probability of auroral zone splitting vs. the intensity of the DR field for various magnetic activity levels (b).

Direct inspection of photographs reveals a distinct splitting of the auroral belt in certain cases: two widely spaced auroral zones are actually observed. This splitting at first may seem quite accidental, since it is observed both at high magnetic activity levels and under relatively quiet conditions. However, a more detailed examination of the splitting conditions reveals certain regular features in this phenomenon. Figure 6a plots (average data for 30 storms) the DR current field (δH_{DR}) and the intensity of the polar disturbances (A_L indices from /29/) corresponding to the time of splitting of the auroral zone. (Splitting is assumed to occur when the two auroral glow regions are spaced by more than 200 km). We see from Figure 6a that the points do not fall at random: they are distinctly clustered around a certain curve. Hence the conclusion that the splitting of the auroral zone is largely determined by these two factors, viz., the intensity of the DR currents and the intensity of the polar disturbances. It is moreover fairly clear that for small δH_{DR} the

zone splitting is observed only for small A_L, but as δH_{DR} increases, the polar storm intensity needed to initiate this splitting also becomes higher. This result is shown in a slightly different form in Figure 6b, which plots from the data of /39/ the probability of splitting of the auroral zone as a function of the DR field intensity for various magnetic activity levels. We see that for a fixed polar disturbance intensity, the probability of zone splitting first increases with the increase in the intensity of DR currents, reaching a maximum at $Q=2-3$ for $\delta H_{DR}\approx -30\gamma$, and then steeply decreases. For $\delta H_{DR}=0$, the splitting probability is very low. Hence it follows that the existence of a belt of DR currents is a necessary condition for the splitting of the auroral zone. Let us try to establish how the existence of DR currents may affect the configuration of the auroral zone.

It has been shown /38/ that the shape of the auroral zone can be derived by considering the adiabatic drift of particles in the magnetosphere in crossed electric and magnetic fields. However, the calculations of particle motion were carried out assuming a dipole magnetic field in the magnetosphere. In accordance with the above data, it is better to explain the auroral zone splitting by the peculiar features of electron motion in the geomagnetic field distorted by the field of DR currents. The electron trajectories in this field were computed in /40/ by numerical integration of the equation of motion of the particles:

$$\frac{d\vec{v}}{dt}=\frac{[\vec{E}\times\vec{B}]}{B^2}-\frac{\mu}{eB^2}[\nabla B\times\vec{B}].$$

The following parameters were used: $\mu=0.7\cdot10^{-5}$ CGSM, $E=(0.3-3)\cdot10^3$ CGSM.

The field of the DR currents was calculated using the Akasofu-Chapman model /41/. The center of the DR belt was taken at $\rho=5R_E$ and the ground value of δH_{DR} was taken to be $(-70)\gamma$ (Figure 7). Figure 8 shows the electron paths for $E=3.3\cdot10^2$ CGSM. It is clear from the figure that the presence of DR currents significantly modifies the motion of particles in the magnetosphere. Indeed, outside the DR belt, the electron trajectories are equivalent to the Alfven trajectories, and the electrons drift eastward around the Earth. As a result, the particle energy and the plasma density increase. On crossing the outer boundary of the DR belt, the particles enter a region where the magnetic field gradient is reversed, and they are thus driven in the westward direction around the Earth. As a result, the electron energy and the plasma density decrease. Having traversed the region of maximum field depression, the electrons again enter a region where the magnetic field increases toward the Earth, and they again start drifting eastward, their energy increasing. The sections of the trajectories over which the electron energy $E \geq 5$ keV are shown by bold lines in Figure 8. The auroral zone, which was found to be continuous for a dipole field B, falls into two parallel zones in the presence of DR currents, with a significant depression of auroral intensity in the gap between the two zones. This conclusion is of the highest importance in the interpretation of the observed splitting of the auroral zone, which is responsible for the development of the middle-latitude auroral zone during strong magnetic storms /39, 42/.

A similar analysis of electron motion in a magnetic field has been carried out for various values of E. Some of the results are presented in Figure 9,

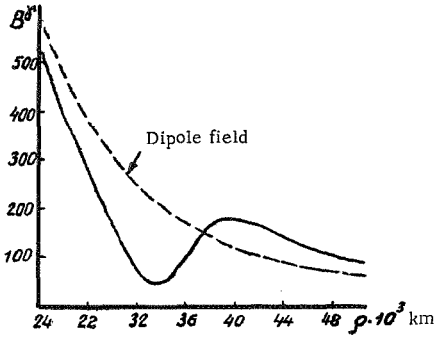

FIGURE 7. The geomagnetic field in the equatorial plane with allowance for the field of DR currents.

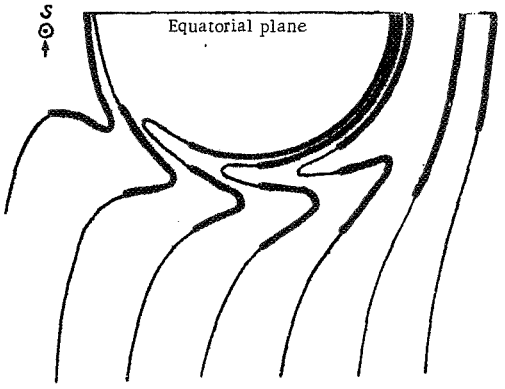

FIGURE 8. Electron trajectories ($\mu = 0.7 \cdot 10^{-5}$ CGSM) in the equatorial plane for $E = 3.3 \cdot 10^{2}$ CGSM.

which gives the position of the south boundary of the auroral zone as a function of the field strength E. The dashed line marks the latitude corresponding to the region of maximum B values, where following the change in the sign of VB the electrons reverse the direction of their motion and the auroral inhomogeneities start drifting in the opposite sense along the arc. The latitudes of zero or low-intensity auroral glow correspond to minimum fields B.

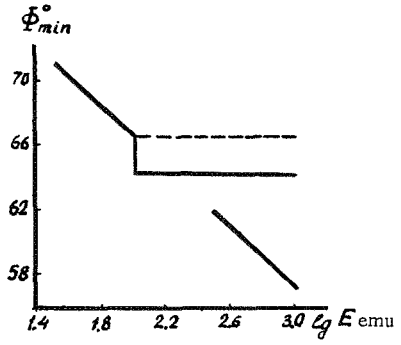

FIGURE 9. The position of the southern boundary of aurorae (calculated) vs. the electric field E.

The above analysis of the motion of charged particles in the Earth's magnetosphere thus explains the observed splitting of the auroral zone and also yields the mean values of the relevant characteristics by tying up the phenomenon with certain points of the DR field. Indeed, it has been shown in /39/ that the probability of observing polar aurorae at various magnetic activity levels differs in years of minimum and maximum solar activity. For low magnetic activity in years of active Sun, the latitudinal distribution of the aurorae has a single maximum at the Fritz zone latitudes. The main maximum of the frequency of auroral occurrence splits into two in days of high disturbance, and an additional maximum is observed at $\phi \approx 52°$. In the light of the above interpretation of the observed zone splitting, it would seem that these features of the latitudinal variation of the auroral frequency indicate that the DR belt in magnetically disturbed days in years of maximum solar activity is located at a distance of from 3 to 5.5 Earth's radii. This is clearly a very plausible conclusion.

The experimental and theoretical results accumulated during the last 2—3 years are on the whole sufficient for elucidating the physical nature of the processes which take place in the Earth's magnetosphere during a

magnetic storm. They enable us to reconstruct the general sequence of development of these processes, which mainly include the generation of the electric field in the magnetosphere, the drift of the auroral plasma in crossed electric and magnetic fields and adiabatic acceleration of the drifting particles, the partial trapping of the auroral plasma by the geomagnetic field, and the formation of the DR current belt. These processes, however, do not cover the entire range of effects accompanying a magnetic storm. In particular, we have so far disregarded such important processes as the onset of instabilities in the auroral plasma, which lead to a redistribution of the particles over the pitch angles and thus cause their penetration into the upper atmosphere /43/. The study of these effects constitutes a highly important independent problem, and we therefore chose to confine the present discussion to macroscopic processes in the magnetosphere.

Bibliography

1. Cole, K.D.— Space Sci. Rev., 5(6):99. 1966.
2. Akasofu, S-I.— Space Sci. Rev., 6(1):21. 1966.
3. Pudovkin, M.I.— In: "Fizika magnitosfery i polyarnye buri," p.100. Irkutsk. 1968.
4. Zaitseva, S.A., M.I. Pudovkin, and O.I. Shumilov.— Geomagnetizm i Aeronomiya, 8(5):905. 1968.
5. Pudovkin, M.I., O.I. Shumikov, and S.A. Zaitzeva.— Planet. Space Sci., 16:881. 1968.
6. Akasofu, S-I. and D.S. Kimball.— Annals of IGY, 38. 1965.
7. Khorosheva, O.V.— Synopses of Reports at the International Symposium on Solar-Terrestrial Physics, p.18. Izd. KrAO.
8. Lijima, T. and T. Nagata.— Rept. Ion. Space Res. in Japan, 22(1/2):1. 1968.
9. Ivliev, D.Ya., M.I. Pudovkin, and S.A. Zaitseva.— Geomagnetizm i Aeronomiya. 1969. (In press.)
10. Starkov, G.V. and Ya.I. Fel'dshtein.— Geomagnetizm i Aeronomiya, 10(2):367. 1967.
11. Belyakova, S.I., S.A. Zaitseva, and M.I. Pudovkin.— Geomagnetizm i Aeronomiya, 8(4):712. 1968.
12. Sano, Yu. and T. Ondon.— Memoirs of the Kakioka Magnetic Observatory, 12(2):1. 1966.
13. Lijima, T. and T. Nagata.— Rep. Ion. Space Res. in Japan, 22(3):16. 1966.
14. Zaitseva, S.A., D.Ya. Ivliev, and M.I. Pudovkin.— Geomagnetizm i Aeronomiya, 9(1):108. 1969.
15. Loginov, G.A., V.A. Mitinev, and M.I. Pudovkin.— Geomagnetizm i Aeronomiya. 1969. (In press.)
16. Pudovkin, M.I. and O.I. Shumilov.— Ann. Geophys., 25(1):555. 1969.
17. Pudovkin, M.I. Polyarnye magnitnye buri (Polar Magnetic Storms).— Leningrad, "Nauka." (In press.)
18. Fairefield, D.H. and L.J. Cahill.— J. Geophys. Res., 71(1):195. 1966.

19. Wilcox, J.W., K.H. Shatten, and N.F. Ness.— J. Geophys. Res., 72(1):19. 1967.
20. Rostoker, G. and C-G. Fälthammar.— J. Geophys. Res., 72(23):5853. 1967.
21. Dessler, A.J. and E.N. Parker.— J. Geophys. Res., 64(12):2239. 1959.
22. Bryunelli, B.E.— Geomagnetizm i Aeronomiya, 6(6):1083. 1966.
23. Scopke, N.— J. Geophys. Res., 71(13):3125. 1966.
24. Frank, L.A.— J. Geophys. Res., 72(5):1905. 1967.
25. Frank, L.A.— J. Geophys. Res., 72(15):3753. 1967.
26. Sugiura, M. and S. Chapman.— Abhandl. Akad. Wiss., Göttingen Math. Phys. Klasse, Sonderheft, 4. 1960.
27. Akasofu, S-I. and S. Chapman.— J. Geophys. Res., 68(10):3155. 1963.
28. Zaitseva, S.A., M.I. Pudovkin, V.V. Dryakhlov, and V.N. D'yachenko.— Geomagnetizm i Aeronomiya. 1969. (In press.)
29. Echols, C., Yu.S. Wong, and T.N. Davis. Hourly Values of the Auroral Electrojet Activity Index for 1958.— Alaska, Geophys. Inst. Univ., UAG R-192. 1967.
30. Cole, K.D.— J. Geophys. Res., 70:1689. 1965.
31. Roach, F.E. and J.R. Roach.— Planet Space Sci., 11:523. 1963.
32. Rees, M.H. and S-I. Akasofu.— Planet Space Sci., 11:105. 1963.
33. Truttse, Yu.L.— Planet Space Sci., 16(8):981. 1968.
34. S-I Akasofu and C-I Meng.— J. Geophys. Res. 72(19):4905. 1967.
35. Davis, T.N. and R. Parthasarathy.— J. Geophys. Res., 72(23):5825. 1967.
36. Piddington, J.H.— J. Atm. Terr. Phys., 29(1):87. 1967.
37. Piddington, J.H.— Planet Space Sci., 16(6):703. 1968.
38. Pudovkin, M.I. and O.I. Shumilov.— Geomagnetizm i Aeronomiya, 8(6):1072. 1968.
39. Isaev, S.I.— Geomagnetizm i Aeronomiya, 2(5):861. 1962.
40. Isaev, S.I., M.I. Pudovkin, D.I. Shumilov, and S.A. Zaitzeva.— International Symposium on the Physics of the Magnetosphere. Washington, 9. 1968.
41. S-I Akasofu and S. Chapman. A Study of Magnetic Storms and Auroras.— Sci. Rept., No.7, NSF Grant No.4/22. 1961.
42. Isaev, S.I.— Geomagnetizm i Aeronomiya, 2(4):663. 1962.
43. Tverskoi, B.A. Dinamika radiatsionnykh poyasov Zemli (Dynamics of Van Allen Radiation Belts).— Moskva, "Nauka." 1968.

APPLICATION OF THE METHODS OF MEASUREMENT OF SMALL AND ULTRASMALL QUANTITIES OF VARIOUS ISOTOPES TO ASTROPHYSICAL RESEARCH

V. O. Naidenov

Let us consider the principal astrophysical problems that are being solved and can be solved with the aid of the methods of measurement of small and ultrasmall amounts of various isotopes.

First we would like to stress the relative meaning of the term "small and ultrasmall" quantities of isotopes. The exact meaning of this term is determined by three factors: a) the present-day level of technical development, b) the particular experimental conditions, c) the individual properties of the isotope to be measured. Let us consider this problem in some detail.

The main way for increasing the detection sensitivity of radioactive isotopes is through the development of low-noise detectors. Analysis of the maximum attainable sensitivity with the existing methods has shown /1/ that a certain experimental setup will measure 10—50 A^{37} atoms and only 10^4 tritium atoms. The great variety of decay modes, decay energies, states of aggregation, etc., results in an enormous diversity in the technical performances of low-noise detectors /2, 3/. The measurement sensitivity of stable isotopes is increased by appropriate development of mass spectrometry and activation analysis. The application of these relatively new methods will determine 10^{11}—10^{12} atoms of the isotope in a sample /4—7/. In some cases (He^3, Li^6, A^{36}), the sensitivity can be increased to 10^7 atoms /1, 8/. In this context, we would like to stress two points.

a) The quantity of the isotope depends on its concentration in the sample and the mass of the sample. Often, the experimental conditions limit the sample to a very small mass. Therefore, even measurements of fairly high concentrations must rely on the techniques developed for the determination of small and ultrasmall quantities of the isotopes. For example, the content of Na, Sc, Cr, Mn, Co, Cu in meteorite chonders is between 10^{-3} and 10^{-1}%. However, the measurements of these elements in individual chonders required the application of activation analysis /9/.

b) The isotopic composition of a given element (e.g., the Pb isotopes in a meteorite) is determined by mass spectrometry and activation analysis. Therefore, in general, these measurements should also be classified as measurements of small and ultrasmall quantities of isotopes (especially as we are actually measuring small isotopic shifts in these cases).

Experience shows that to attain maximum sensitivity, we must take into consideration the specific properties of the isotope. As a result, narrow-purpose equipment is generally used, capable of determining at most 1 to 3 isotopes.

Dynamic methods and methods employing photographic emulsion are not classified among the conventional detector techniques. In astrophysical research, we are naturally interested in comparing the performance of different experimental techniques. The entire range of astrophysical problems can be divided into two parts: astrophysical processes which occur in the present or whose effects are observable in the present, and astrophysical processes which took place in the past. The processes of the first group can be dealt with by examining synthetic, artificial specimens. The development of satellite techniques will probably open new vistas in this direction. The second group must rely on natural specimens only. These include various terrestrial minerals, marine and glacial sediments, some biological objects, etc. Specimens of extraterrestrial origin occupy a position of special significance. These include meteorites and cosmic dust. In the near future, scientists will actually be able to examine rocks of lunar origin and specimens from other planets.

PAST PROCESSES

1. The origin of the solar system

Numerous studies have been published on the origin of the solar system and the early stages of its development /10—13/. However, the theory is still far from being complete. Any theory should explain the entire range of currently observable effects and phenomena. This primarily includes the various topics of nucleosynthesis and the related aspects of the abundance of the chemical elements in the Sun and the planets, as compared to the cosmic abundance of the elements in the Universe. This also includes various mineralogical and laboratory studies aimed at elucidating the conditions necessary for the formation of the isotopic, cosmic, mineralogical, and other compositions. Measurements of small and ultrasmall quantities of isotopes inevitably occupies a position of leading importance in this work. They are mainly applied to dating and determination of the isotope composition of various formations in meteorites, abyssal terrestrial rocks, and other natural specimens. Dating is done by measuring the mother to daughter isotope ratio (K—Ar, Rb—Sr, U—Pb methods) or by measuring the isotope ratio of the same element (Pb—Pb method). These dating techniques are naturally based on certain starting assumptions which are not immune to occasional criticism /14/. The isotope ratio of a given element, e.g., Pb or Xe, in principle may shed light on nucleosynthesis processes. Indeed, the quantity of the element being determined, Pb^{204} say, is assumed to have remained constant since the time of nucleogenesis, whereas the other isotopes may have built up gradually owing to the decay of the heavier radioactive elements ($U^{235} \rightarrow Pb^{207}$). The uncertainty in the interpretation of these measurements is fairly high, since the details of the r-process have been poorly developed, and various differentiation and diffusion processes have to be allowed for in the last stages. Some topics should be revised in connection with the probable existence of "stability islands" among the transuranides. Therefore, large-scale measurements are required of the isotopic composition of various meteorites, meteoritic inclusions (the individual chonders),

and various terrestrial rocks. The establishment of a time scale and the isotopic composition will apparently be the main problem when the first lunar specimens are obtained.

2. The history of cosmic rays

The celestial bodies in the solar system are subjected to the continuous impact of cosmic rays. The interaction of cosmic rays with the surface of meteorites, interplanetary dust, and the Earth's atmosphere has been considered in great detail /15—20/, and we will therefore only list the main astrophysical aspects with brief comments. At the earliest stages of evolution of the solar system the flux of cosmic rays was probably higher than it is today. This is uncertain, however, since the only sufficiently long-lived isotope produced by exposure to cosmic rays is K^{40} ($T_{1/2}=1.3\cdot 10^9$ years). Comparison of the K^{40} and K^{41} abundance in various iron meteorites did not provide a conclusive solution to this problem /21/. The last 10^7 years, on the other hand, were studied in much greater detail. Several overlapping and mutually reinforcing methods are available for this period. We can analyze the quantity of stable and radioactive isotopes, or short-lived and long-lived isotopes produced in nuclear reactions with cosmic rays. So far, however, results confirm the constancy of the cosmic ray intensity during the relevant period apart from a factor of 2. This uncertainty is largely associated with various impurities in natural targets and with inaccuracies in the excitation function.

The problem of the cosmic ray intensity has been adequately covered only for the last $5\cdot 10^4$ years. This is entirely due to the great advance in radiocarbon dating. The cosmic ray intensity was found to have remained constant within a few per cent. These topics are closely linked with the detection of short intensity bursts and modulation of cosmic rays in the past. Simultaneous measurement of the concentrations of radioactive isotopes with various halflives in principle should provide information regarding both these aspects /17/. The corresponding experiments, however, involve considerable difficulties and no adequate measurements have been carried out so far. One point should be stressed: the Earth's atmosphere provides a much more suitable target for these studies than the meteorites do. The radioactive isotopes forming in the Earth's atmosphere in reactions with cosmic rays naturally separate to settle in different sedimentary strata. Be^{10}, for example, makes it possible to identify a major burst even if it occurred a few million years ago. These studies require measurements in strata of known age. The situation in this respect is analogous to the currently developed idea of studying supernova bursts during the last millennium from the increased C^{14} content in the tree rings /22/.

3. The history of meteorites

The meteorite dating obtained by K—Ar and U—Pb methods does not agree with the results which take into consideration the yield of nuclear products in reactions triggered by cosmic rays (the so-called "cosmic age" of the meteorites). This discrepancy can be resolved by assuming that the meteorites, being minor objects in the solar planet, originated from a substantially larger body in whose interior the effect of cosmic rays was greatly suppressed.

Analysis of the stable to radioactive isotope ratios provided some insight into the preatmospheric shape of the meteorites and made it possible to estimate the collision frequencies and the erosion of meteorites in the interplanetary space. Typical quantities of some isotopes in stony meteorites produced by cosmic ray reactions are the following /23/: in 10^8 years, He^3, Ne^{21}, and A^{38} form in quantities of $2 \cdot 10^{14}$, $4 \cdot 10^{13}$, and $5 \cdot 10^{12}$ atoms per cm^3, respectively. Higher instrumental sensitivity is required for the analysis of individual inclusions in meteorites (chonders, magnetic or nonmagnetic fractions) or individual layers. The cosmic age of meteorites of various classes constitutes a highly important problem. A low cosmic age indicates that meteorites of the given type apparently formed near the Earth, possibly from the outer layers of the Moon. A high cosmic age (10^7 years) implies asteroidal origin.

4. Interplanetary dust

Zodiacal light and meteorite trails reveal the existence of macroscopic dust particles in the interplanetary space. The mass spectrum of these particles has been studied by various methods, but there is still no clear picture /24—26/. Interplanetary dust settles in layers in glacial and other sediments. The peculiar features of the dust particles as minute members of the solar system are reflected in the rate of formation of the various isotopes, which is mainly determined by the low-energy soft solar cosmic rays, and not the harder galactic cosmic rays affecting the meteorites. The dust therefore is expected to show a high level of activity for isotopes with low-threshold nuclear reactions and can be used to study the variation of solar cosmic rays /18, 20, 27/. Problems relating to the origin of interplanetary dust, its lifetime in the interplanetary space, and interaction with other objects of the solar system are solved by a combination of methods applicable to the determination of isotopic composition and dust mass spectrum.

* * *

In the nearest future we will be able to analyze directly the surface rocks of the Moon and Mars. This will provide a tool for studying various rare and little-probable events which can be detected only over large time intervals. For example, a slight excess of the induced radioactivity over the general background in individual patches of the lunar surface will supply an indication of antibodies having impacted against the Moon /28/. The presence of isotopes produced by cosmic ray reactions may be used as proof of the extraterrestrial origin of the specimen.

PRESENT PROCESSES

1. Spatial distribution of cosmic rays and modulation effects

Several methods are available for solving this problem. One of the methods is based on measuring the ratio of a short-lived (days, weeks) to a long-lived (years) isotope, forming in similar nuclear reactions (e.g.,

the A^{37}/A^{39} ratio). Another method involves dynamic measurements from spaceships. So far, however, detailed measurements have been carried out inside the Mars orbit, while the meteorites probe more distant parts of the solar system. The distribution of the light isotopes (H^3, He^3, He^4) in the interior of a meteorite /29/ sheds light on modulation effects.

2. The solar wind

The solar wind is studied by a great variety of methods. The combination of the results is adequately described by the theory /30/. However, further insight is required into the nature and the effects of the solar wind. Detailed studies of the isotopic composition of the solar wind may greatly help in this direction. Both natural and artificial specimens can be used. The solar wind particles penetrate into the outer skin layer (a few microns thick for a density of about $3\,g/cm^3$) of the meteorite or the lunar surface. The meteorites lose this skin-deep information on entering the Earth's atmosphere because of partial ablation. The lunar surface, on the other hand, reliably stores the information. In general, numerous ambiguities and uncertainties encountered in meteorite measurements are eliminated when we deal with the surface of the Moon. Moreover, lunar surface measurements will certainly provide a new angle for analyzing the extensive results of meteorite measurements. Artificial specimens avoid the uncertainties associated with the complex chemical composition of natural targets. A thin foil of high-purity material exposed on board a spaceship or by the astronauts on the Moon will readily separate the solar wind particles from high-energy particles and their secondary products. Estimates /31/ show that in 24 hours a $300\,cm^2$ target may acquire $2 \cdot 10^{14}$ He atoms, $5 \cdot 10^{12}$ Ne atoms, and $8 \cdot 10^{10}$ A atoms. A 40 kV potential applied to the target will increase the collection efficiency by a factor of 50. As a result, the fluxes of H^2, H^3, He^3, He^4, and other solar wind isotopes can be measured. Although this is not a dynamic method and the exposure takes a few days, this is a fairly short time for various purposes. Measurements carried out under various conditions, at various distances and in different phases of the solar activity, will reveal the dynamics of numerous phenomena associated with the solar wind. Comparison of the abundance of isotopes in the solar wind with the content of these isotopes in various meteorites (there are meteorites with anomalous content of the rare gases) and their abundance on the Sun will provide certain information relating to the origin of the solar system. These measurements will possibly supply an indication of whether or not the solar wind "blew stronger" in the past.

3. The composition of the galactic cosmic rays

Considerable attention is currently focused on the isotopic composition of the galactic cosmic rays in connection with problems of their origin, the probing of the interstellar medium, etc. The photographic emulsion and the dynamic methods are widely supplemented by techniques which call for the development of the traces of heavy metals in meteorites and special artificial specimens. The last method makes it possible to determine the preatmospheric shape of the meteorite and the mass lost in the atmosphere /32/. The high content of He^3, Li, Be, B in the galactic cosmic rays has been established long ago. A substantial percentage of deuterium nuclei has also been detected /33/. Assuming that these are secondary products, we can

estimate the mass traversed by the cosmic rays and their lifetime /34/. In principle, large high-purity targets will measure the tritium fluxes also. We can thus find the mass traversed by the cosmic rays in the neighborhood of the solar system (a few tens of light years). Estimates show that a 1 m^2 target exposed for 100 days will detect the tritium nuclei if their number exceeds 0.1—0.15 of the total number of He^3 nuclei.

4. Solar cosmic rays

Large solar flares may eject streams of relatively energetic particles. This explains the considerable attention focused on the mechanism of this phenomenon. Measurements of the isotopic composition of the solar cosmic rays and its comparison with the abundance of the elements on the Sun makes it possible to decide whether these isotopes are products of nuclear reactions in the solar flare or the entire solar composition is accelerated. By measuring the content, in the solar cosmic rays, of those isotopes whose abundance in the Sun is negligible, we can find the interplanetary mass traversed by the particles (as for the galactic cosmic rays) /35, 36/. The acceleration mechanism can be inferred from the ratio of isotopes with different charge to atomic weight ratio (H^1, H^2, H^3, He^3, He^4, C, A). Measurements of H^3 and He^3 were carried out during a large solar flare /37, 38/ and a relatively high content of these isotopes was discovered: the content of tritium was 0.4% of the number of protons, and the content of He^3 reached 10%. These experiments, however, suffered from uncertainties which interfered with unambiguous interpretation: no measurement data were available on the integral flux of H^1 and He^4; the measurements were made with random samples without preliminary isotopic purity control. It is highly desirable to proceed with further measurements of this kind. Interesting results will probably be obtained by exposing a stack of special purity plates. The sensitivity of the equipment for tritium (10^5—10^6 atoms) and He^3 (10^7—10^8 atoms) is sufficient for additional measurements of the energy spectrum of each isotope.

5. Accretion of matter by the Earth

The origin of He, A, Xe and similar gases in the Earth's atmosphere is often explained by reference to accretion of gases from the interplanetary space. Quantitative estimates of this effect, however, involve considerable difficulties. In particular, the magnetic field near the Earth and in the plasma apparently lowers the rate of accretion. Detailed calculations should therefore proceed from measurements of the isotopic composition of the solar wind and the low-energy component of the solar cosmic rays outside the Earth's magnetosphere.

6. The radiation belts of the Earth

The problems of stability, origin, and lifetime of particles in the radiation belts and the relation of these parameters to solar activity — this is only a partial list of topics of current interest. Protons and electrons are so far the only particles detected in any measurable quantities /39/. However, during large solar flares, the nuclei of solar cosmic rays may be trapped. Measurements of tritium in the metal of rockets and satellites made after a solar flare /37/ suggest that particles other than protons may be trapped;

these measurements even went further and provided the lifetime of H^3 in the radiation belt (a few months). However, as we have already noted, there are numerous uncertainties in the interpretation of these results /37/. Measurements in radiation belts should therefore be continued, using methods similar to those described for solar cosmic rays above.

7. Measurements of the neutrino flux from the Sun

The high penetrating power of the neutrino, although ideal for probing deep into the solar interior, constitutes a great disadvantage from the viewpoint of detection. The problems of neutrino astrophysics are widely discussed in this volume, and we will therefore mention only one point which has bearing on the methodology of A^{37} measurements. By using a low-noise proportional counter, we can raise the sensitivity to 10 A^{37} atoms. This record sensitivity is in no way inferior to the sensitivities of photoemulsions and dynamic methods.

CONCLUSION

Our survey is by no means complete and exhaustive. And yet, it gives some idea of the enormous scope of astrophysical problems that can be studied and solved by measuring small and ultrasmall quantities of various isotopes. Our discussion takes into consideration the availability of lunar rock samples and exposure of large artificial targets in outer space. This, however, by no means detracts from the importance of natural samples, such as meteorites, marine and glacial sediments, etc. The increased sensitivity of the measuring equipment will enable us to measure individual inclusions, formations, or strata.

It is only natural to strive to determine the maximum number of different isotopes in a single sample. This is a difficult task, however, since the high-sensitivity techniques, as we have noted above, are generally suitable for simultaneous measurements of from 1 to 3 isotopes. Cooperation between different laboratories or installation of different kinds of equipment for the determination of small and ultrasmall quantities of various isotopes in one institute is therefore inevitable.

I would like to acknowledge the help of G. E. Kocharov and Yu. N. Starbunov and their valuable critical comments.

Bibliography

1. Kocharov, G.E. and V.O. Naidenov.— Trudy V Vsesoyuznoi ezhegodnoi zimnei shkoly po kosmofizike, p. 100. Izdatel'stvo Kol'skogo Filiala AN SSSR, Apatity. 1968.
2. Watt, D.E. and D. Ramsden. High Sensitivity Counting Techniques.— Pergamon Press. 1964.
3. Kocharov, G.E. and V.O. Naidenov.— PTE, No. 3:5. 1966.
4. Metody analiza veshchestv vysokoi chistoty (Methods of Analysis of High-Purity Materials). Edited by I.P. Alimarin.— Moskva, "Nauka." 1965.

5. Yoe, J.H. and H.J.Koch [Editors]. Trace analysis. New York, Wiley. 1957.
6. Taylor, D. Neutron Irradiation and Activation Analysis.— Princeton, Van Nostrand. 1964.
7. Kuznetsov, R.A. Aktivatsionnyi analiz (Activation Analysis).— Moskva, Atomizdat. 1967.
8. Alimova, I.A., B.S. Boltenkov, V.N. Gartmanov, B.A. Mamyrin, and B.N. Shustrov.— Geokhimiya, No.9:1044. 1966.
9. Schmitt, R.A., R.H. Schmitt, and G.G. Goles.— J. Geophys. Res., 70:2419. 1965.
10. Fowler, W.A., J.L. Greenstein, and F. Hoyle.— Geophys. J., 6:148. 1962.
11. Cameron, A.G.W.— Icarus, 1:314, 339. 1962.
12. Marshall, R.R.— Icarus, 1:95. 1962.
13. Kohman, T.R.— J. Chem. Educ., 38, 73. 1961.
14. Rancitelly, L.A. and D.E. Fisher.— J. Geophys. Res., 73:5429. 1968.
15. Anders, E.— Rev. Mod. Phys., 34:287. 1962.
16. Arnold, J.R.— Ann. Rev. Nucl. Sci., 11:349. 1961.
17. Geiss, H., H. Oeschger, and U. Schwarz.— Space Sci. Rev. 1:197. 1962.
18. Lal, D. and B. Peters.— Prog. Element. Particle and Cosmic Ray Phys., 6:3. 1962.
19. Arnold, J.R., M. Honda, and D. Lal.— J. Geophys. Res., 66: 3519. 1961.
20. Wasson, J.T.— Icarus, 2:54. 1963.
21. Voshage, H. and H. Hintenberger.— Z. Naturforsch., 14a: 828. 1959.
22. Konstantinov, B.P. and G.E. Kocharov.— Doklady AN SSSR, 165:63. 1965.
23. Eberhardt, P., O. Eugster, J. Geiss, and K. Marti.— Z. Naturforsch., 21a:414. 1966.
24. Öpik.— Proc. Roy. Irish Acad., 54a:165. 1951.
25. Nazarova, T.N.— KI, 4:900. 1966.
26. Konstantinov, B.P., M.M. Bredov, and E.P. Mazets.— Doklady AN SSSR, 174:580. 1967.
27. Alder, V., H. Oeschger, and J.T. Wasson.— In: "Radioactive Dating and Methods of Low-Level Counting," p.189. Vienna. 1967.
28. Vlasov, N.A. Antiveshchestvo (Antimatter).— Moscow, Atomizdat. 1968.
29. Shen, C.S. and R.K. White.— J. Geophys. Res., 73:4273. 1968.
30. Parker, E.N.— Planet Space Sci., 13:9. 1965.
31. Singer, P., P. Eberhardt, and J. Geiss.— J. Geophys. Res., 70:2243. 1965.
32. Fleisher, R.L., P.B. Price, R.M. Walker, and M. Maurette.— J. Geophys. Res., 72:331. 1967.
33. Fan, C.J., G. Gloeckler, and J.A. Simpson.— Phys. Rev. Lett., 17:329. 1966.
34. Ramaty, R. and R.E. Lingenfelter.— Can. J. Phys., 46:5627. 1966.
35. Biswas, S. and C.E. Fichtel.— NASA X-611-65-219. 1965.

36. Lingenfelter, R.E. and R. Ramaty.— Publ.593. Univ. of California, Los Angeles. 1967.
37. Tilles, D., J. Defelice, and E.L. Fireman.— Icarus, 2:258. 1963.
38. Schaeffer, O.A. and J. Zähringer.— Phys. Rev. Lett., 8:389. 1962.
39. Fenten, K.B.— J. Geophys. Res., 72:3889. 1967.

PLASMA CONTAINMENT IN ADIABATIC TRAPS

B. B. Kadomtsev

Research into plasma containment in adiabatic traps was begun in connection with the purely applied problem of controlled thermonuclear fusion. In quite a short time, a wide range of interesting physical phenomena were discovered in a plasma contained in an adiabatic trap, and the discovery of the radiation belts of the Earth demonstrated that similar effects may occur under natural conditions also. Considerable progress has been achieved by now toward understanding the physical effects in traps and we are in a position to summarize the various results in this field. The various problems of containment of isolated particles, equilibrium and hydrodynamic stability of plasma have been clarified in general outline, and our understanding of the kinetic plasma instability has markedly improved.

Experimental studies of the containment of isolated particles have shown that the adiabatic invariant is conserved with exponential accuracy, and in very strong magnetic fields longer containment is observed. This is probably a hint at the permanent conservation of the adiabatic invariant in axisymmetric traps, theoretically predicted by Arnold.

An important stage in the investigation of plasma containment in adiabatic traps was marked by the experiments of M.S. Ioffe and co-workers, who showed that plasma in ordinary traps develops the theoretically predicted fluting hydrodynamic instability. The same experiments established the possibility of stabilizing the flute instability by means of additional current-carrying rods.

The main emphasis at present is on the kinetic instabilities, which are a manifestation of the maser effect of electromagnetic wave amplification by means of population inversion. In hot-ion plasma, this group of instabilities includes cyclotron pumping of Alfven waves ("pearls") and Langmuir waves (Harris instability), conical and drift-conical instability of dense plasma, modified negative-mass instability, and a number of more restricted and less significant instabilities. Conical and drift-conical instabilities are the only ones which have not been observed so far experimentally.

In hot-electron plasma, the principal instability is the cyclotron pumping of whistlers. This instability is observed in most laboratory experiments, and it is also highly effective in the radiation belts of the Earth.

Experiments show that the instabilities are in fact responsible for the collective processes in a plasma contained in adiabatic traps;

instabilities also play a decisive role in the formation of the radiation belts around the Earth.

A paper on plasma containment in adiabatic traps will be published in Uspekhi Fizicheskikh Nauk by B. B. Kadomtsev, and M. S. Ioffe. It will deal in detail with the various aspects of this problem.

DISTRIBUTION OF THE OUTER BELT PROTONS IN THE μ, L SPACE

Yu. I. Gubar' and V. P. Shabanskii

Comparison of the theory of charged particle transport across the drift envelopes with experimental findings is more meaningful in the space of adiabatic invariants.

The particle distribution in this space was derived from experimental data on low-energy proton fluxes. The results of intensity measurements provided by EXPLORER XII, EXPLORER XXVI, and ELEKTRON-series satellites were used to this end. The equatorial particles were first considered. Proton fluxes with energies above a given value are converted into fluxes with fixed minimum magnetic moment. The transformation is performed assuming an exponential energy spectrum and also directly, without any assumption concerning the spectrum.

With the exponential spectrum, magnetic moment conservation leads to a radial intensity profile which is independent of μ_{min} in a certain range. The fluxes $j(>\mu)$ rapidly increase as L rises from 2 to 3—3.5. For L values beyond the belt maximum, $j(>\mu)$ is a relatively weak function of L. This is particularly obvious for the section of the outer proton belt according to the EXPLORER XII 1961 data. A somewhat stronger (decreasing) dependence of the fluxes $j(>\mu)$ on L emerges from the measurements of EXPLORER XXVI early in 1965, at low magnetic disturbance levels. The transformation from energy to the magnetic moment thus revealed a definite time variation of intensity, which was apparently associated with significant changes in solar activity.

The radial variation of the equatorial fluxes for small μ fits the analogous computations of L. S. Chesalin for particles near the equator (EXPLORER XII). For large μ, a certain divergence is observed due to the latitudinal dependence of the fluxes. The proton distribution function in the μ, L space is obtained from the Nakada-Mead relation. The connection of this relation with Janosi's more general relation and with Dungee's expression for the phase space element in the variables μ, L is established. A dipole magnetic field is assumed.

The distribution function based on experimental data differs from the steady-state distribution without losses and sources beyond the belt maximum. The difference is particularly significant for 1961, when the solar activity was still fairly high. Instead of decreasing as L^{-2}, the distribution function increases with L. For some values of μ, the distribution function even increases as L^5. The results are in qualitative agreement with Hess' calculations for nonequatorial particles (from the data of EXPLORER XII).

The separability of the distribution function, established by Hess for nonequatorial particles, follows for equatorial particles from the exponential energy spectrum and the conservation of μ. Certain processes which may be responsible for the observed proton distribution are considered.

The pressure of protons with a given minimum magnetic moment is not particularly sensitive to L beyond the belt maximum. The protons are thus in a nearly equilibrium state, which may be the result of sufficiently rapid diffusion. Direct measurements of the fluxes $j(>\mu)$ are highly desirable.

SELF-SIMILAR FLOW IN RAREFIED PLASMA

M. A. Gintsburg

The problems of the self-similar evolution of a spherical plasmoid, a cylindrical plasma pinch, and a plane plasma sheath are considered. The corresponding differential equation is

$$\delta \cdot v + (\eta v)' = (1-\eta v)\left\{ \ln\left[e^{\int \frac{dv}{v}} e^{-\frac{v^2}{2}} \cdot \frac{1}{\eta^2} \right] - (1-\eta v)\eta v'' + v'(\eta^2 v' - \delta) + \eta v' v (1+\delta) \right\}', \qquad (1)$$

where v is the ion velocity,

$$\delta = \begin{cases} 0 \text{ for the cylinder,} \\ 1 \text{ for the plane sheath,} \\ -1 \text{ for the sphere.} \end{cases}$$

Prime denotes differentiation with respect to $\eta = t/r$.

Numerical solution of equation (1) on a computer leads to the following conclusions.

1. When the variation of the density n as a function of the time t is observed at a fixed point, n(t) is not a monotonic function (as for a flowing neutral fluid) but has a maximum for some $\eta < 1$ (a solution in the form of a unit density and velocity pulse). The plasma spreads out in sheaths.

2. A characteristic velocity inversion effect is observed: once the density and velocity pulse has passed through a given point, the ion velocities at that point are directed inward, to the center, i.e., besides the general outward flow of the plasmoid, there is also inward, centerward flow of ions.

3. The ions are accelerated in the course of their centerward motion. After the pulse has passed, the ion velocities do not go to the unperturbed value v = 0. In other words, ion acceleration is irreversible, a highly significant point for its efficiency.

4. The spherical (cylindrical, plane) pulse gradually spreads and becomes diffuse, and its amplitude decreases.

If the magnetic field is introduced, the self-similar equations of magnetic hydrodynamics take the following form in the plane case:

$$\vec{v}' = \frac{(1-v^2)^{\frac{1}{2}}}{1-\eta v_x}\left(\vec{E} - \vec{v}(\vec{E}\vec{v}) + [\vec{v}\vec{H}]\right),$$

$$H_y' = \frac{\eta}{1-\eta^2}\left(H_y + n_i v_{iz} - n_e v_{ez}\right) - \frac{E_z}{1-\eta^2}; \quad E_y' = \frac{1}{1-\eta^2}\left(\eta E_y + H_z + n_e v_{ey} - n_i v_{iy}\right), \text{ etc.}$$

In the cylindrical case,

$$v_z' = \frac{v_\varphi^2}{1-\eta v_z} + \frac{(1-v^2)^{1/2}}{1-\eta v_z}\left(E_z - v_r(\vec{E}\vec{v}) + v_\varphi H_r - v_r H_\varphi\right), \text{ etc.}$$

We also derived a numerical solution of the two-dimensional steady-state problem of the transverse flow of a plasma beam as a result of the formation of runaway electrons along the or axis (the beam moves along the oz axis). Computations show that there are no electrons inside a certain cone directed along the oz axis with an opening angle $\pi - 2\theta_{max}$. Let K_1, K_2, K_4, K_5 be the density, the transverse velocity, the field, and the longitudinal velocity of the beam ions in the plane z = 0. Then to first approximation ($\tan\theta < 1$)

$$\tan\theta_{max} = 2K_5 \frac{\left[\left(\frac{K_4}{K_5} + K_2\right)^2 + 8 + A\right]^{1/2} - \left(K_2 + \frac{K_4}{K_5}\right)}{8 + A}, \qquad (2)$$

where $A = e^{K_3} - K_1 - 2\delta + (K_4/K_5)^2 + K_2 \cdot (K_4/K_5)$.

Equation (2) is the solution of the problem of flow around a cone ($\delta = 0$) or a wedge ($\delta = +1$) with an opening angle $\pi - 2\theta_{max}$. If the conical angle θ is larger than $\pi - 2\theta_{max}$, the drag is high, and for $\frac{\theta}{2} < \frac{\pi}{2} - \theta_{max}$ the drag is low.

PARTICLE ACCELERATION IN A PLASMA IN OUTER SPACE

M. A. Gintsburg

A mechanism of particle acceleration by the eddy electric fields of nonlinear waves was described in the author's publications (see below). For example, the energy increment of an ion in a hydromagnetic wave is given by

$$\Delta W = 4H_0^2/8\pi n_0,$$

where H_0 and n_0 are the average parameters of the unperturbed plasma, i.e., the particles absorb four times the energy of the initial magnetic field. Under the conditions of a strong chromospheric flare ($H_0 = 500$ gauss, $n_0 = 10^8$ cm^{-3}), we have $\Delta W = 250$ MeV, which is in fact the typical energy of solar cosmic rays. Electrons are also accelerated by the nonlinear wave, so that ion acceleration is invariably accompanied by X-ray bursts. The role of particles trapped in the potential well of relativistic electron waves is also analyzed.

Bibliography

Ginzburg, M.A. — J. Geophys. Res., 72:2749. 1967. Gintsburg, M.A. — Astronom. Zh., 45:610. 1968.

COMPARISON OF THE VARIATIONS OF HIGH-ENERGY ELECTRONS AND ULTRA-LOW-FREQUENCY RADIATION

A. B. Malyshev, P. M. Svidskii, V. A. Burov, I. G. Kleimenova, and V. A. Troitskaya

The results of simultaneous observations of the injected high-energy electron fluxes and ULF radiation ("hissing") are compared.

1. The electron fluxes were observed in the region of drift envelopes with L from 3 to 5.5 at altitudes between 220 and 1150 km. Electrons with energy above 0.2 MeV (scintillation counters) and above 1.5 MeV (Geiger counters) were recorded. The ULF radiation between 0.5 and 10 kHz was picked up by ground stations. The electron and the radiation fluxes were measured in the area of Kerguelen Isl.

2. During these observations (2 — 11 July 1965), significant variations in the high-energy electron fluxes were noted. Analysis of observation findings points to three types of electron injection: a) catastrophic, b) normal, c) slight. Each type of injection is associated with a certain spectrum of ULF radiation.

3. Assuming that the ULF wave propagates along a line of force, we can compute the upper cutoff frequency for each L envelope. The upper cutoff frequency in the spectrum of ULF radiation in the magnetosphere is determined by the electron cyclotron resonance absorption at the apex of the force line.

4. Comparison of the computations with the observed spectrum of ULF radiation during the high-energy electron injection indicates that the injection type is correlated with the ULF radiation spectrum. The interaction of the trapped electrons with the electromagnetic waves modifies the pitch-angle distribution and eventually leads to their injection into the atmosphere.

5. Interaction with ULF radiation is the only effective mechanism allowing electrons to escape from the outer radiation belt.

THE EFFECT OF SOLAR WIND VELOCITY INHOMOGENEITIES ON THE STRUCTURE OF THE INTERPLANETARY FIELD

I. I. Alekseev, A. P. Kropotkin, and A. R. Shister

Experimental data reveal a significant dependence of the solar wind velocity on the heliolatitude θ and the heliolongitude φ. We considered the structure of the interplanetary field in relation to this anisotropy of solar plasma ejection.

The streaming velocity V of the solar wind is known to be high compared to the velocity of sound cs and the Alfven velocity c_A in the interplanetary space. Therefore, to first approximation, we may ignore the effect of the thermal and magnetic pressure gradients on the velocity field. The velocity field is therefore assumed given and independent of time; we take $v_r = \text{const}$, $v_\theta = v_\varphi = 0$. The magnetic field is frozen into this given, and in generally spherically asymmetric, plasma stream. The problem of the kinematic transport of the magnetic field from the space around the Sun into the interplanetary space was solved under these assumptions. The solution gives the following field components:

$$B_r = B_{r_0}\left(\frac{r_0}{r}\right)^2 + \frac{r_0}{rV}\left(1-\frac{r_0}{r}\right)\left[\frac{B_{\varphi_0}}{\sin\theta}\frac{\partial V}{\partial \varphi} + B_{\theta_0}\frac{\partial V}{\partial \theta}\right];$$

$$B_\theta = \frac{r_0}{r}B_{\theta_0}; \qquad B_\varphi = \frac{r_0}{r}B_{\varphi_0},$$

where $B_{r_0} = B_r(r_0, \theta, \varphi)$, $B_{\theta_0} = B_\theta(r_0, \theta, \varphi)$, $B_{\varphi_0} = B_\varphi(r_0, \theta, \varphi)$, the scale r_0 is conveniently taken of the order of a few Sun's radii. We thus see that B_r is essentially determined by the inhomogeneities of the solar wind velocity, and the corresponding effect increases with increasing distance r. Estimates show that velocity inhomogeneities of scale $\Delta\varphi \sim 1$ may produce significant changes in B_r at the Earth's orbit, and even reverse its sign, for $\Delta V/V \sim 10\%$. For smaller-scale $\Delta\varphi$, a similar effect is observed even for smaller velocity inhomogeneities.

We derived the shape of a force line which significantly differed from the ordinary Archimedes spiral, forming, in particular, characteristic loops of different sizes, not unlike those observed experimentally.

INTERACTION OF HIGH-ENERGY PARTICLES WITH THE NEUTRAL LAYER OF THE MAGNETOSPHERE TAIL

I. I. Alekseev and A. P. Kropotkin

Since the neutral layer in the magnetosphere tail, where the tangential magnetic field component reverses its sign, is relatively thin, $d \sim 0.1 R_E$ (where R_E is the Earth's radius), the motion of particles of sufficiently high energies with Larmor radii $r_L \geqslant d$ in the field of the tail is no longer adiabatic in this layer. On the other hand, when $r_L \gg d$, the motion of particles near the neutral layer may be analyzed by treating this layer as an infinitesimally thin boundary between two regions with a homogeneous field. The tangential component of the magnetic field has opposite signs on the two sides of this plane boundary. Analysis of particle motion in this simple model leads to the following results.

1. For a given ratio of normal to horizontal field components $\frac{B_n}{B_t} = \tan\alpha$, the particle will either be transmitted through the boundary or reflected from the boundary, depending on the pitch angle β_0 and the phase of the Larmor rotation φ_0 which the particle has when it first crosses the boundary.

2. Before being transmitted or reflected, the particle will in general cross the boundary several times. The crossing multiplicity n also depends on β_0 and φ_0.

3. If the angle α is not too small, $\alpha \geqslant 1$ (this case is observed during magnetic disturbances, when the Earth-ward edge of the current layer approaches to the Earth and $\frac{B_n}{B_t} \sim 1$). In this case, $n \sim 1$ almost for all values of β_0 and φ_0. The simple relations expressing the variation of β and φ when the particle moves near the boundary make it possible to compute for $\alpha \geqslant 1$, the values of the parameters β_n, φ_n which the particle acquires when it moves away from the boundary (assuming that the "initial" parameters β_0, φ_0 are known). The evolution of the pitch angle distribution of the particles crossing the boundary and being reflected from the boundary was estimated, with allowance for the actually observed strong dispersion in pitch angles.

4. For small $\alpha \ll 1$, which is the case observed in the magnetosphere tail proper ($\alpha \sim 1/20$), the first adiabatic invariant is approximately satisfied, $\beta_n \simeq \beta_0$, although the motion is nonadiabatic, as before.

5. For $\alpha \ll 1$ the number of particles reflected from the boundary is equal to the number of transmitted particles.

6. For $\alpha \ll 1$ the total number of boundary crossings n was computed as a function of β_0 and the resultant displacement of a particle in the plane of the neutral layer across the magnetosphere was determined. Effects of particle leakage from the magnetosphere through the neutral layer and particle injection effects can be assessed on the basis of these findings.

LOCALIZATION OF ACTIVE SOLAR REGIONS RESPONSIBLE FOR THE GENERATION OF THE GEOEFFECTIVE AGENT

V. P. Nefed'ev

To determine the probable onset and duration of the generation of the agent responsible for the decrease of the cosmic ray intensity, we considered certain processes in active regions on the Sun at the level of the photosphere (variation of sunspot area); at the level of the chromosphere (chromospheric flares of strength 2B and higher); at the level of the corona (number and spectrum of events at meter wavelengths). We thus analyzed the solar activity during ten months in 1967 and for the months of August–September 1966. The solar activity varied quite markedly during this period.

Periods of solar activity sufficiently clearly localized in time were selected for analysis. The beginning of each active period was identified either with a marked increase in sunspot area or with a marked increase in flare activity (or both, if the increase in sunspot area and in flare activity were observed simultaneously). The end of the active period was identified with the decrease in flare activity or in sunspot area. A total of 13 active periods were identified.

Twelve active periods on the Sun corresponded to decreases of cosmic ray intensity of various amplitude and character. The tracings of cosmic ray intensity decrease showed three characteristic points: T_1 – the decrease begins, T_2 – the cosmic ray intensity starts increasing back to the initial level, T_3 – the cosmic ray intensity has fully recovered.

The time between T_1 and T_2 was found to be equal (to within one day) to the overall duration of the active period on the Sun. Short active periods on the Sun (of about 1 day) corresponded to intervals $T_1 - T_2 \simeq 1$ day. The longest of the observed active periods (7–8 days) corresponded to a cosmic ray intensity decrease with $T_1 - T_2$ also equal to 7–8 days.

The active regions on the Sun were observed between E50 and W40 (at the beginning of each active period), except for a single region at E90, which did not have a substantial effect on the cosmic ray intensity.

APPLICATION OF ELECTRICAL FIELDS IN INTERPLANETARY SPACE AS RADIATION SHIELDING AGAINST PROTONS AND ELECTRONS

T. Ya. Ryabova and K. A. Trukhanov

One of the basic problems encountered in connection with the feasibility of a prolonged stay in interplanetary space involves the radiation shielding of the scientific equipment, materials (photographic film, say), and naturally also spacecraft crew and other living organisms on board.

Since the weight of the conventional radiation shielding which attenuates the penetrating radiation in a suitable absorbing mass accounts for a substantial fraction of the total spacecraft weight (especially in long trips), it is highly desirable to ensure maximum shielding efficiency with minimum weight and maximum reliability in relation to the particular conditions of interplanetary travel.

One of the most attractive solutions of this problem is by deflection of charged particles from the spacecraft hull by strong electrical fields. Analysis shows than an electrostatic radiation shielding system is highly effective and its weight is one order of magnitude less than the weight of the equivalent absorbing shielding (the power requirements are quite low also). The main results pertaining to the electrostatic shielding against the protons of the inner radiation belts and the principal engineering difficulties making the electrostatic shielding unfeasible in the nearest future were analyzed. Effective electrostatic shielding can be provided at this stage under the conditions of natural and artificial electron radiation belts, ensuring adequate shielding of a small volume from solar flare protons.

Since the electron flux intensity in the radiation belts is fairly high ($\sim 10^7 - 10^8$ el/cm^2 sec), the deflecting electric field of the electrostatic shielding may be set up by utilizing the charge induced by the electrons from the radiation belts, i.e., without resorting to any high-tension sources on board spacecraft.*

Another highly important problem is the shielding against electrons (it is relevant for long-lived orbital stations in 24-hour orbit, for spacecraft accelerated by low-thrust engines, for objects exposed to high electron fluxes from the beta decay of nuclear reaction products). In view of the high intensity of the electrons and the production of highly penetrating bremsstrahlung, the conventional shielding is generally very bulky.

The efficiency of the electrostatic shielding was assessed in terms of certain parameters which express the principal characteristics of

* Leakage currents from the surface of a high-voltage electrode are virtually suppressed by means of a thin (about 0.01 g/cm^2) system screening off the ultraviolet radiation of the Sun and interplanetary plasma ions.

shielding in general form for any given electron spectrum ($dN/d\varepsilon \sim \varepsilon^{-\gamma}$, $dN/d\varepsilon \sim \exp(-\frac{\varepsilon}{\varepsilon_0})$, $dN/d\varepsilon \sim \exp(-0.5758 - 0.0558^2)$. Using these characteristics, the weight of the electrostatic shielding was estimated: it was found to be $^1/_{20} - ^1/_{30}$ of the corresponding weight of conventional absorbing shielding. The "self-charging" of the shielding makes it no less reliable than any conventional shielding.

The electrostatic shielding thus provides one of the most promising ways of ensuring radiation safety of spacecraft in the radiation belts of the Earth.